



Andrea Pucci

**Sol-Gel Não Aquoso para Nanopartículas Dopadas
de Óxido do Metal**

**Nonaqueous Sol-Gel Routes to Doped Metal Oxide
Nanoparticles**



Andrea Pucci

Sol-Gel Não Aquoso para Nanopartículas Dopadas de Óxido de Metal: Síntese, Caracterização, Organização e Propriedades

Nonaqueous Sol-Gel Routes to Doped Metal Oxide Nanoparticles: Synthesis, Characterization, Assembly and Properties

Dissertação apresentada à Universidade de Aveiro para cumprimento dos requisitos necessários à obtenção do grau de Doutor em Química, realizada sob a orientação científica do Doutor Nicola Pinna, Investigador Coordenador do Departamento de Química da Universidade de Aveiro

Dedico este trabalho à Nonno

o júri

presidente

Prof. José Manuel Lopes da Silva Moreira
Professor catedrático da Universidade de Aveiro

Prof. Georg Garnweitner
Juniorprofessor da Technischen Universität Braunschweig, Germany

Prof. Antonio Jorge Duarte de Castro Silvestre
Professor coordenador do Instituto Superior de Engenharia de Lisboa

Prof. Mauro Comes-Franchini
Professor associado da Università di Bologna, Italy

Prof. Fernando Manuel Bico Marques
Professor catedrático da Universidade de Aveiro

Prof. Tito da Silva Tridade
Professor associado com agragação da Universidade de Aveiro

Prof. Nicola Alessandro Pinna (Orientador)
Investigador coordenador da Universidade de Aveiro e WCU professor assistente da Seoul National University

agradecimentos

I am most grateful to my supervisor, Prof. Nicola Pinna for giving me the opportunity to begin this PhD adventure and for driving me through it. You taught me a lot and not only from the scientific point of view.

I thank all jury and especially Prof. G. Garnweitner and Prof. A. Silvestre for agreeing to be external examiner and for carefully checking this manuscript. All the people that contributed to this work, with a special mention for Prof. David Zitoun and Dr. Felipe Figueiredo, with whom I am indebted. All the people working at the University of Aveiro, Montpellier II and Seoul.

S.-H. Yu and Prof. Y.-E. Sung are kindly acknowledged for their help on the electrochemical characterization on LTO materials. Prof. G. Ungar and his group in Sheffield are acknowledged for SAXS measurements and relative electron density calculations.

The more important thing in order to enjoy the lab life is to have nice fellows around. I thank Catherine, Gianvito and all the group members for helping me when needed and cheering me up continuously. Marc & Guylaine in particular for being my guides in material science and in life.

Kris, Gareth, Tiago, Seba, The "Gambosinhos" Aveiro Frisbee Team, all the foreigner students I met in this 4 years Erasmus. Ricardo, Carlos, Rui M. Rui, Gil and Mohamed and both white and black teams. Duncan, Dany, Kieran and all people I use to hang around with. The citizen, past and present, of the Republic of Rua do Mercado; in particular, a special thank to Donna Rosete, for being like a mum to all of us. Everyone added a little piece to the puzzle of this fantastic lifechanging experience.

This work received the financial support from FCT and EMMI-FAME network of Excellence.

palavras-chave

Síntese Solvotermica, Via de Síntese com o Alcool Benzílico, Nanopartículas de Oxido Metálico, Dopagem

resumo

Os resultados apresentados nesta tese foram obtidos sob o projeto de doutoramento intitulado " Vias de Síntese não aquosas para nanopartículas de óxido metálicos dopados: Síntese, caracterização, organização e propriedades". O objetivo deste estudo é a investigação de nanoestruturas de óxidos metálicos dopados com metais de diversa natureza, conduzindo a diferentes tipos de aplicações.

O controlo mais fácil da a cinética reaccional nas vias de síntese solvotermicas, em comparação com métodos aquosos, permite combinar a reatividade dos precursores dos óxidos metálicos, abrindo o caminho a uma forma de produção de óxidos dopados fácil e a baixa temperatura. Neste manuscrito são discutidos diversos exemplos da aplicação da " via de síntese com o alcool benzílico". Esta poderosa via sintética foi utilizada para preparar zircônia, háfnia e varias perovskites dopadas com metais de transição, na procura de propriedades magnéticas interessantes, e igualmente na preparação de óxido de zirconio dopado com metais raros. Uma utilização adicional deste metodo de síntese, que prova a sua solidez, constitui na preparação de nanocristais de $\text{Li}_4\text{Ti}_5\text{O}_{12}$ com excelentes propriedades eletroquímicas para aplicações em baterias de lítio. Finalmente, o efeito do dopagem e dos outros parâmetros de reação no empacotamento dos nanocristais é racionalizado.

O estudo desses materiais foi realizado na Universidade de Aveiro e também na University of Montpellier II e na Seoul National University, onde existem equipamentos e competências complementares.

keywords

Solvothermal synthesis, Benzyl Alcohol Route, Metal Oxide Nanoparticles, Doping

abstract

The results presented in this thesis have been achieved under the Ph.D. project entitled "Nonaqueous Sol-Gel routes to doped metal oxide nanoparticles: Synthesis, characterization, assembly and properties". The purpose of this study is the investigation of metal oxide nanostructures doped with metals of a diverse nature, leading to different type of applications.

The easier control over the reaction kinetics in solvothermal routes, compared to aqueous methods, allows to better match the reactivity between metal oxide precursors, paving the way to a facile and low temperature production of doped oxides. In this manuscript diverse examples of the exploitation of the "Benzyl Alcohol Route" are discussed. Such a powerful pathway was utilized for the synthesis of transition metal doped zirconia, hafnia and various perovskites, and the study of their magnetic properties, as well as the synthesis of rare earth doped zirconium oxide. A further extension, proving the solidity of the synthetic method, is shown for the preparation of $\text{Li}_4\text{Ti}_5\text{O}_{12}$ nanocrystals carrying excellent electrochemical properties for lithium-ion battery applications. Finally, the effect of doping and other reaction parameters on the assembly of the nanocrystals is discussed.

These studies were carried out principally at the University of Aveiro, as well as at the University of Montpellier II and at the Seoul National University due to complementary available expertises and equipments.

Table of Content

Dedication.....	V
Jury.....	VII
Acknowledgement.....	IX
Portuguese Abstract.....	XI
English Abstract.....	XIII
Table of Content.....	XV
List fo Figures.....	XVI
Acronyms & Symbols.....	XVIII
Acronyms.....	XX
Symbols.....	XXI
Chapter 1: Non-Aqueous Sol-Gel Routes to Metal Oxides.....	1
1 Introduction.....	3
2 Solvothermal Synthesis.....	3
2.1 Thermolysis.....	4
2.2 Non-aqueous sol-gel chemistry.....	5
2.3 The “Benzyl Alcohol Route”.....	6
2.3.1 Ether elimination.....	6
2.3.2 Ester elimination.....	7
2.3.3 C-C bond formation.....	9
2.3.4 Hybrid and composite materials.....	10
3 Doping in NHSG.....	13
4 Conclusion and Layout of the Manuscript.....	13
5 Bibliography.....	16
Chapter 2: Techniques and Methods.....	21
1 The solvothermal synthesis.....	23
1.1 Zirconia.....	23

Table of Content

1.2	Hafnia	25
1.3	Perovskite.....	25
1.4	Lithium titanate	27
2	Characterization techniques	27
2.1	X-ray powder diffraction (XRD)	27
2.2	Electron microscopy (EM)	27
2.3	Electron paramagnetic resonance (EPR).....	28
2.4	Superconducting quantum interference design magnetometry	28
2.5	X-ray absorption spectroscopy (XAS)	28
2.6	Small-angle X-ray scattering (SAXS).....	29
2.7	Electrochemical characterizations.....	29
2.8	Dilatometry	30
2.9	Impedance spectroscopy	30
2.10	Other techniques	30
3	Bibliography	32
Chapter 3: Transition Metal Doped Oxide.....		33
1	Introduction	35
2	Result and Discussion	37
2.1	Synthesis	37
2.2	Structural and Morphological Characterization	39
2.2.1	ZrO ₂	39
2.2.2	HfO ₂	41
2.2.3	Perovskites.....	41
2.2.4	TEM	44
2.2.5	Diffuse reflectance.....	47
2.2.6	XAS.....	49
2.3	Annealing	50
2.4	Magnetic properties.....	53
2.4.1	EPR.....	53
	Susceptibility Studies	58
3	Conclusions	63
4	Bibliography	65
Chapter 4: Rare Earth Doped Zirconia.....		69
1	Introduction	71

2	Results and Discussion	72
2.1	Structural and Morphological Characterization	72
2.2	Electrochemical properties of 14.8% Y-doped ZrO ₂	78
2.2.1	Sintering of the ceramics	78
2.2.2	Electrical conductivity	80
3	Conclusions.....	86
4	Bibliography	87
Chapter 5: Lithium Titanium Oxide.....		89
1	Introduction	91
2	Results and Discussion	93
2.1	Structural and Morphological Characterization	93
2.2	Electrochemical properties	97
3	Conclusions	101
4	Bibliography	103
Chapter 6: Assembly.....		105
1	Introduction	107
2	Results and discussion	109
3	Conclusions.....	122
4	Bibliography	124
Conclusions.....		128

List of Figures

Figure 1.1: Schematic representation of a standard condensation mechanism involving ether elimination.....	7
Figure 1.2: Schematic representation of a standard condensation mechanism involving ester elimination.....	8
Figure 1.3: Schematic representation of the proposed condensation mechanism of BaTiO ₃	10
Figure 3.1: XRD patterns of Mn-doped zirconia.....	39
Figure 3.2: XRD patterns of Mn-doped hafnia.....	40
Figure 3.3: XRD pattern of Cr-doped ZrO ₂ and Cr-doped HfO ₂	40
Figure 3.4: XRD pattern of Mn-doped and Cr-doped BaTiO ₃	42
Figure 3.5: XRD pattern of Mn- doped and Cr-doped BaZrO ₃	43
Figure 3.6: TEM images of ZrO ₂ and HfO ₂	44
Figure 3.7: SEM and TEM images of Mn-doped BaTiO ₃ and BaZrO ₃	46
Figure 3.8: UV-Vis spectra of doped ZrO ₂ and HfO ₂	48
Figure 3.9: XANES spectra of Mn-doped ZrO ₂ Cr-doped ZrO ₂	50
Figure 3.10: XRD patterns of Zr _{0.970} Mn _{0.030} O _{2-δ} after annealing under air	52
Figure 3.11: XRD patterns of Zr _{0.920} Mn _{0.080} O _{2-δ} after annealed under oxygen.	52
Figure 3.12: EPR spectra of Mn-doped zirconia	53
Figure 3.13: EPR spectra of Hf _{0.85} Mn _{0.15} O _{2-δ}	54
Figure 3.14: Second derivative of EPR spectra of Zr _{0.920} Mn _{0.080} O _{2-δ} as synthesized and after annealing	55
Figure 3.15: Temperature dependence of the resonance intensity of the EPR spectra in Zr _{0.920} Mn _{0.080} O _{2-δ} annealed under oxygen at 800 °C.....	56
Figure 3.16: EPR spectra of Cr-doped zirconia and Cr-doped hafnia.....	57
Figure 3.17: ZFC/FC and hysteresis loop for Zr _{0.920} Mn _{0.080} O _{2-δ} after annealing under oxygen.	58
Figure 3.18: ZFC/FC curves and hysteresis loop Mn-doped hafnia	60
Figure 3.19: Magnetic measurements Zr _{0.980} Cr _{0.020} O _{2-δ} , pristine and annealed at 650°C.	61
Figure 4.1: XRD of zirconia doped with europium or terbium.	72
Figure 4.2: XRD of 5.8% Y-doped ZrO ₂ synthesized at different temperature.....	75
Figure 4.3: XRD of 14.8% Y-doped ZrO ₂ synthesized with yttrium alkoxide and the one synthesized using YCl ₃	75
Figure 4.4: TEM and HRTEM images of functionalized Eu-doped ZrO ₂ and of Y-doped ZrO ₂ prepared with YCl ₃ precursor.....	77
Figure 4.5: Dilatometry plot of Y-doped ZrO ₂	79
Figure 4.6: SEM of YSZ sintered at (a) 1300, (b) 1400 and (c) 1500 °C.	80

Figure 4.7: Representative impedance spectra obtained at 350 °C for the YSZ.	81
Figure 4.8: Equivalent electrical circuit chosen at low temperatures.	82
Figure 4.9: Temperature dependence of the apparent grain boundary and specific grain boundary conductivity	83
Figure 4.10: Temperature dependence of the space charge potential.	85
Figure 5.1: The Li^+ intercalation/deintercalation equilibrium between the two LTO phases.	91
Figure 5.2: XRD pattern of the as prepared LTO nanostructures	93
Figure 5.3: XRD pattern of the as-prepared and calcined LTO nanostructures with a Li:Ti concentration ratio of 8.5:8 mmol	95
Figure 5.4: SEM and TEM of LTO structure.	96
Figure 5.5: HRSEM images of the LTO micrometric sized particles.	97
Figure 5.6: Capacity-voltage profiles for as-synthesized and calcined nanocrystalline $\text{Li}_4\text{Ti}_5\text{O}_{12}$.	98
Figure 5.7: Capacity versus cycle number for nanocrystalline $\text{Li}_4\text{Ti}_5\text{O}_{12}$.	99
Figure 5.8: Reversible capacity versus cycle number.	101
Figure 6.1: XRD patterns of the ZrO_2 samples.	109
Figure 6.2: TEM and of the assembly	110
Figure 6.3: SEM and TEM images of supercrystals).	113
Figure 6.4: SAXS diffractogram of pure Zirconia synthesized at 230 °C and relative reconstructed electron density map	114
Figure 6.5: SAXS diffractogram of pure Zirconia synthesized at 325 °C and relative reconstructed electron density map.	115
Figure 6.6: SAXS diffractogram of 10% Tb-doped Zirconia synthesized at 325 °C and relative reconstructed electron density map.	116
Figure 6.7: HRTEM image of the Voronoi polyhedra.	118
Figure 6.8: ^{13}C Solid State NMR and FT-IR spectra of pure zirconia.	119
Figure 6.9: SAXS diffractograms of Zirconia samples as a function of the annealing temperature.	121

Acronyms & Symbols

Acronyms

BnOH	Benzyl Alcohol
BET	Brunauer–Emmett–Teller
CHN	Carbon, Hydrogen, and Nitrogen Elemental Analysis
DMS	Diluted Magnetic Semiconductors
DSC	Differential Scanning Calorimetry
EC	Electrochemistry
EDX	Energy Dispersive X-ray Spectroscopy
EELS	Electron Energy Loss Spectroscopy
EPR	Electron Paramagnetic Resonance
EXAFS	Extended X-ray Absorption Fine Structure
GC-MS	Gas Chromatography – Mass Spectroscopy
HRTEM	High Resolution Transmission Electron Microscope
ICP-AES	Inductively Coupled Plasma – Atomic Emission Spectroscopy
IR	Infrared
Ln	Lanthanides
MRI	Magnetic Resonance Imaging
NHSG	Non Hydrolytic Sol-Gel
NMR	Nuclear Magnetic Resonance
NPs	Nanoparticles
PL	Photoluminescence

RE	Rare Earth
RT	Room Temperature
SAED	Selected Area Electron Diffraction
SAXS	Small Angle X-ray Spectroscopy
SEM	Scanning Electron Microscope
SQUID	Super Quantum Interference Design
TEM	Transmission Electron Microscope
TGA	Thermogravimetric Analyses
TM	Transition Metal
UV-Vis	Ultraviolet - Visible
XANES	X-ray Absorption Near Edge Structure
XRD	X-ray Diffraction
ZFC-FC	Zero Field Cooled – Field Cooled

Symbols

χ	Susceptibility
μ_B	Bohr Magneton, $\mu_B = 9.27400915 \times 10^{-24} \text{ JT}^{-1}$
A	Hyperfine Coupling Constant, $A (\text{cm}^{-1}) = g \mu_B a/hc$
HS	Hyperfine Splitting (T)
g	g-factor (dimensionless), $h\nu = g\mu_B$
H _c	Coercive Field

Acronyms & Symbols

M_S	Magnetization at Saturation
T_B	Blocking Temperature
T_N	Neel Temperature
T_θ	Curie-Weiss temperature
T_C	Curie Temperature
C	Charge Rate
ϵ_0	Permittivity of Vacuum
ϵ_r	Relative Permittivity
δ_{gb}	Grain Boundary Thickness
$\sigma_{gb,sp}$	Grain Boundary Conductivity
R_{gb}	Grain Boundary Resistance
C_{gb}	Grain Boundary Capacitance
C_b	Bulk Capacitance
σ_b	Bulk Conductivity
$\sigma_{gb,sp}$	Grain Boundary Conductivity
$\Delta\Phi$	Difference Between Bulk and Grain Boundary Charge Potential

CHAPTER 1*
Non-aqueous Sol-Gel Routes to Metal Oxides

*This chapter is partially based on: A. Pucci, N. Pinna Z. *Naturforsch.* **2010**, 65, 1015

Table of contents

1	Introduction	3
2	Solvothermal Synthesis	3
2.1	Thermolysis.....	4
2.2	Non-aqueous sol-gel chemistry	5
2.3	The “Benzyl Alcohol Route”	6
2.3.1	Ether elimination.....	6
2.3.2	Ester elimination.....	7
2.3.3	C-C bond formation	9
2.3.4	Hybrid and composite materials	10
3	Doping in NHSG	13
4	Conclusion and Layout of the Manuscript.....	13
5	Bibliography	16

1 Introduction

The fundamental and applied scientific importance of nanomaterials has, without any doubt, been demonstrated in the last decade. The peculiar conductive, magnetic, optical, and chemical properties at the nanoscale led to several breakthroughs in various fields. Biomedical applications, long life batteries, spintronic devices, and solar cells are just a few examples of how these nanomaterials can be exploited¹⁻⁴. As the knowledge and development of nanoscience advances, a growing attention is given to the development of versatile, cheap and scalable synthesis methods allowing at the same time the precise control of the composition and of the size and shape at the nanometer scale. As a matter of fact, the above mentioned properties are strongly affected by the size and shape of the nanostructures. The traditional route to inorganic materials is the ceramic approach; high temperature is used to provide interdiffusion of metal ions between intimately mixed solid precursors. On the one hand, this method is universally applicable and leads to high density materials and a high degree of crystallinity. On the other hand, it does not permit the control of the shape, size and size distribution at the nanometer scale. Moreover, the major limitation is the thermodynamic control over the reaction, leading only to the more stable compounds. Many wet chemistry methods have been developed to achieve the preparation of other interesting materials (*i.e.* kinetically promoted and metastable phases). Among these protocols, the solvothermal method plays an outstanding role. Solvothermal synthesis generally refers to a reaction occurring in the presence of any kind of solvent in a sealed system (*e.g.* in an autoclave) with the temperature raised above the boiling point of the solvent.

2 Solvothermal Synthesis

The understanding of the formation mechanism and the growth of nanocrystals in solution in order to direct the synthesis towards the desired product is one of the major objectives of nanochemistry. This would make solution approaches more

suitable for applications, but also allowing cheaper and greener paths. Up to now, it is nearly impossible to foresee the morphology of nanoparticles and the tailoring of their composition, size and shape can be done only on an empirical basis.⁵ To attain this objective, the comprehension of the reaction mechanisms is clearly the starting point.⁶⁻⁷ The solvothermal method is particularly suitable from this point of view as the reaction systems are relatively simple, especially when no surfactant or capping agents are used. The study of organic byproducts allows the investigation of how the precursors interact, suggesting a way to set the different reaction parameters.⁶ The most common reactions occurring in nonhydrolytic solvothermal synthesis are thermolysis and metathesis reactions. Other routes have been exploited which go through a complex-formation process or a reduction/oxidation as in the case of γ - LiV_2O_5 nanorods.⁸

2.1 Thermolysis

The formation of nanomaterials by thermal decomposition of metal complexes has been extensively studied and was mainly applied to obtain metals. The decomposition of the ligands toward the production of metal oxide nanoparticles generally involves alkene elimination and the formation of a hydroxyl group. One of the first attempts for the synthesis of metal oxides was studied by Inoue and coworkers.⁹

Their synthesis approach involves the thermal decomposition of metal complexes, at temperatures ranging from 200 to 300 °C, in diverse glycols, ethylene glycol and 1,4-butanediol being the most investigated. Through this route several metal oxides¹⁰⁻¹² and phosphates¹³ were synthesized. Simple alcohols have also been exploited. For example, Inoue compared the products obtained reacting aluminum alkoxides in various solvents under solvothermal conditions.¹⁴ Simple primary alcohols led to hybrid materials in which solvent alcohol molecules are incorporated between boehmite layers through covalent bonding.¹⁵ Similar results were obtained in glycol media but, in these cases, the organic moieties in the derivative of boehmite,

presenting two functional groups, act as bridges between the inorganic layers.¹⁶ The length of the carbon chain affects the size of the final product. Thus, these approaches allow the synthesis of hybrid materials with tunable size and interlayer distance. Noteworthy, the alkoxide (glycooxide) derivative of boehmite can eventually be an intermediate step toward the synthesis of γ -alumina by increasing time, temperature or concentration of the precursor during the reaction.^{14,17} Other more complex solvents were used, such as 2-methoxyethanol, leading to the oxides of cerium,¹⁸ gallium¹⁹ or rare earth metals.²⁰ Metal hydroxides were also prepared reacting $\text{RE}(\text{NO}_3)_3$ in alcohols or glycols at 250 °C, obtaining different morphologies;²¹ only after calcination the pure oxides were obtained. Recently, Julian-Lopez *et al.* synthesized a mesoporous $\text{Er}_2\text{Ti}_2\text{O}_7$ pyrochlore structure in ethanol at 170 °C, however, very probably, the reaction mechanism is more complex than a simple thermal decomposition in this case.²²

2.2 Non-aqueous sol-gel chemistry

Some advantages such as the cheapness of the solvothermal approach towards other synthesis methods are even more pronounced in the case of metathesis reactions, where it is not necessary to reach the thermal decomposition of the precursor and lower temperatures are often allowed. Three polymorphs of titania, namely anatase, rutile and brookite, were obtained from TiCl_4 under solvothermal condition (110 °C) just varying the solvent (diethyl ether, ethanol and *tert*-butanol, respectively).²³ Other examples of materials which were prepared through a metathesis approach are hollow spheres of hematite²⁴ or tetragonal CoO ²⁵ in ethanol and in presence of a surfactant.

Alkylhalide, ether, ester or amide eliminations, C-C bond cleavage or formation processes are some of the mechanisms taking place during metal oxide formation. These reactions are grouped under the general name of non-aqueous or nonhydrolytic sol-gel (NHSG) chemistry.^{6-7,26-28} A brief description of this chemistry

will be made in the following section as most of these synthesis paths are involved in the formation of metal oxide nanostructures through the “benzyl alcohol route”.

2.3 The “Benzyl Alcohol Route”

From a general point of view, the non-aqueous and/or NHSG method allows the synthesis of nanoparticles even in sub-solvothermal conditions (typically between 40 and 180 °C) exploiting metal halides as precursor. Several oxides have been obtained through this approach.²⁹⁻³¹ Nevertheless, it is difficult to avoid the presence of halide impurities in the final product making this path not suitable when high purity is required. In such cases, by exploiting the advantages of solvothermal syntheses involving slightly higher temperatures it is possible to transform metal complexes in the respective oxide.

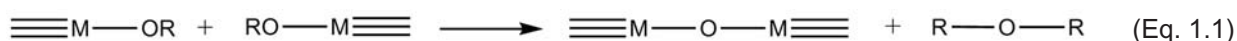
The non-aqueous sol-gel synthesis of oxide nanocrystals is based on organic condensation reactions leading to the formation of metal-oxygen-metal (M-O-M) bonds. It is important to notice that, using benzyl alcohol as solvent, the condensation can occur directly among the ligand of the metal precursor or upon a ligand exchange reaction. Indeed, in this system BnOH has a three-fold role, that is i) as reaction media, ii) as capping agent controlling and limiting the crystal growth and iii) providing the oxygen for the inorganic network.

2.3.1 Ether elimination

The reaction of a metal alkoxide in benzyl alcohol to form M-O-M bridges occurs often through ether elimination (Eq. 1.1), as in the cases of TiO₂, SnO₂ and, in particular, as two of the systems, ZrO₂ and HfO₂, which are discussed in this manuscript.³²⁻³⁶

The solvothermal reaction of hafnium ethoxide in benzyl alcohol has been extensively studied.³² The ether elimination between benzyl alkoxide resulted to be prominent compared to the same reaction among ethoxide species. As a matter of fact, the amount of benzyl ether was found to be 3 times higher than the diethyl counterpart in

the mother liquor. This indicated a strong tendency of the ethoxy groups to exchange (Eq. 1.2) prior the condensation reaction (Eq. 1.3), probably promoted by the mesomeric effect of the aromatic moiety and the excess of benzyl alcohol in the solution. The use of precursors with longer organic chain as ligand (the synthesis of ZrO_2 and HfO_2 will be carried out with zirconium(IV) isopropoxide isopropanol complex and hafnium(IV) *tert*-butoxide, respectively; *cf.* Chapter 2) should reduce the extent of the ligand exchange, as observed in the solvothermal treatment of $Ti(OiPr)_4$.³⁷



R = Bn or Et

Figure 1.1: Schematic representation of a standard condensation mechanism involving ether elimination (Eq.1.1) and the relative example of HfO_2 network formation (Eq. 1.3) preceded by a ligand exchange (Eq. 1.2).

2.3.2 Ester elimination

Other more stable and/or less expensive metal precursors such as carboxylates can also be used as metal source. Their solvothermal treatment in benzyl alcohol leads to the elimination of the corresponding ester (Eq. 1.4). As a typical example, benzyl acetate was found in the reaction mixture after the production of zinc oxide both in conventional heating³⁸ and under microwave irradiation³⁹⁻⁴⁰. The ester elimination pathway is well known in zinc carboxylate-alcohol systems⁶ and has been observed in different cases.⁴¹⁻⁴² Solvothermal treatment of $Zn(ac)_2$ in the excess of benzyl alcohol leads to the formation of benzyl acetate and zinc hydroxide derivative (Eq. 1.5). Thus, the condensation reaction occurs through two parallel mechanism between either two zinc hydroxides with formation of water or between zinc acetate and hydroxide.³⁸ This

Chapter 1 – Non-aqueous Sol-Gel Routes to Metal Oxides

latter reaction presents acetic acid as byproduct which promptly reacts with benzyl alcohol to form benzyl acetate and water. It must be point out that in inert solvent (e.g. ketons or aldehydes) the direct condensation between $Zn(ac)_2$ and BnOH can occur with no OH group involved.

Unfortunately, the processes involved in the reactions were not studied systematically for all the materials produced using this approach. No mechanisms have been proposed for the synthesis of Mn^{43} or Cr oxide, for example. In particular, chromium systems were never investigated in BnOH and even in other media the reaction path was never examined.⁴⁴ On the other hand, a mechanism can be proposed in the case of iron oxides. Several precursors were investigated for the synthesis of either magnetite or maghemite nanoparticles.^{39,45} An ester elimination mechanism was proposed by Gotic and Music⁴⁶ in the case of iron acetate reacting in ethanol or octanol. However, when iron acetylacetonate is reacted in benzyl alcohol or benzylamine the formation of Fe-O-Fe bridges passes through a mechanism involving the cleavage of a C-C bond in the acetylacetonate moiety.^{7,47} In the case of benzylamine, the C-C bond cleavage leads to iron-enolate species which further react with the solvent molecules promoting ketimine condensation. This last reaction leads to species presenting hydroxyl groups that can further condensate to iron oxide nanoparticles.⁴⁷

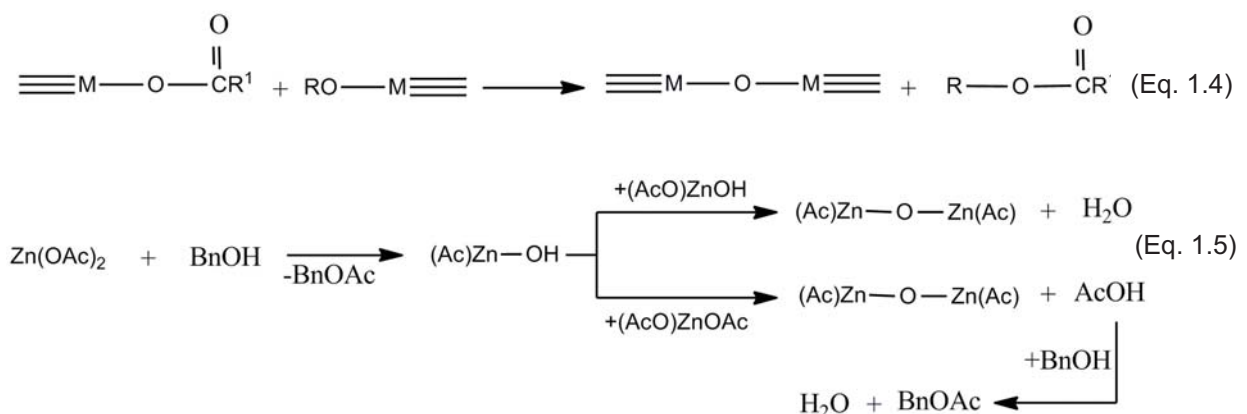


Figure 1.2: Schematic representation of a standard condensation mechanism involving ester elimination (Eq. 1.4) and the relative example of ZnO network formation (Eq. 1.5).

2.3.3 C-C bond formation

The aldol/ketimine condensation is not the only mechanism leading to C-C coupling in NHSG. Indeed, it is important to mention that the metal center often acts as a catalyst leading to the formation of new carbon-carbon bonds. During the synthesis of CeO₂ nanoparticles from Ce(O*i*Pr)₃ 4-phenyl-2-butanol and 1,5-diphenyl-3-pentanol were found in the reaction mixture.⁴⁸⁻⁴⁹ The side products are suggested to be due to a coupling activated by the formal deprotonation of a methyl group of the isopropoxide ligand. A similar coupling, following a Gubert-like reaction,⁵⁰⁻⁵¹ occurs during the formation of alkaline earth metal titanates.⁵²⁻⁵³ Benzyl alcohol can oxidize alkali and alkaline earth metals near room temperature forming a benzylate complex (Eq. 1.6) which catalyze the reaction by deprotonating a methyl group in β -position of the isopropyl ligand (2). The resulting carbanion (3) finalizes the condensation with a nucleophilic attack at an activated benzyl alcohol group that lead to the formation of 4-phenyl-2-butanol (5) and of the metal oxide bond (6).

Other interesting perovskites or ternary oxides have been synthesized through the benzyl alcohol route following the same reaction (e.g. NaNbO₃,⁵⁴ NaTaO₃⁵⁴). The formation of LTO nanostructures will be proved to follow a similar mechanism (*cf.* Chapter 5).⁵⁵ The possibility of matching the different reactivity of diverse kinds of metal complexes in benzyl alcohol makes this approach extremely versatile even for the preparation of complex materials.⁵⁶

Chapter 1 – Non-aqueous Sol-Gel Routes to Metal Oxides

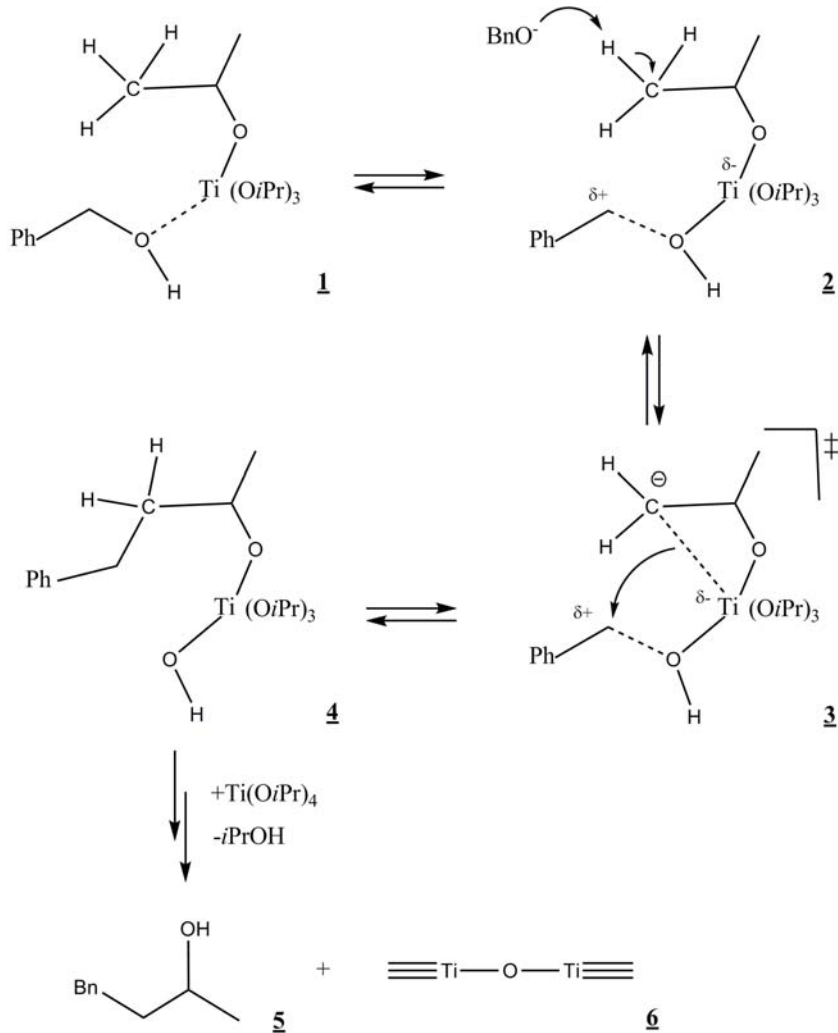


Figure 1.3: Schematic representation of the proposed condensation mechanism of BaTiO_3 . It involves the oxidation reaction of Ba in BnOH (Eq. 1.6) as first step followed by the catalyzed formation of 4-phenyl-2-butanol and inorganic bridges.

2.3.4 Hybrid and composite materials

Another possibility offered by this synthetic route is the formation of nanostructured hybrid materials. The benzyl alcohol (or in some cases a derivative resulting from the reaction process) acts as a capping ligand to specific crystallographic facets of the *in*

situ formed inorganic nanocrystals allowing to obtain highly anisotropic shapes. Simultaneously, it stabilizes and phase-separates the inorganic nanocrystals by creating a highly ordered superstructure with spatially well-defined domains.⁵⁷ The combination of organic and inorganic components leads to multifunctional materials with properties arising from the two constituents but also from the interface between them.⁵⁸ The first hybrid material synthesized in benzyl alcohol was Y_2O_3 .⁵⁹ The reaction of $Y(OiPr)_3$ in benzyl alcohol at 250 °C led to a lamellar structure in which benzoate molecules were arranged in between the inorganic layers. Following these results, the approach was extended to rare earth oxide nanohybrids such as gadolinium, neodymium, erbium and samarium oxides.⁶⁰⁻⁶¹

Another family of hybrid materials was recently synthesized by reacting alkaline earth metal oxide precursors (Ca, Ba or Sr) and aluminium isopropoxide at 275 °C. The synthesis led to flower-like particles consisting of uniform thin platelets or needles stabilized by benzoate ligands.⁶²

When tungsten chloride is reacted in anhydrous benzyl alcohol pure inorganic platelets of tungstite are obtained.^{29,63} A small quantity of a specific ligand, introduced during the synthesis, dramatically affects the morphology and the supramolecular arrangement of the final material. For example, with deferoxamine mesylate the final material is constituted of long wires of $W_{18}O_{49}$ which have a uniform diameter of about 1.3 nm, an aspect ratio of more than 500 and are organized in bundles. They are kept together by π - π interactions between benzaldehyde molecules adsorbed at their surface.⁶³ Similar nanowires were also obtained without additional ligands when tungsten isopropoxide was used instead of tungsten chloride.⁶⁴ When 4-*tert*-butylcatechol was used as ligand, long rods consisting of highly ordered lamellar organic-inorganic hybrid structures similar to the ones found for the rare earth hybrid materials were observed.⁶⁵

From these examples it is clear that different precursors lead to different nanostructures, but in these systems, the addition of an inert solvent plays also a crucial role in determining shape, size and polydispersity. As a typical example, the previously shown synthesis of ZnO in benzyl alcohol results in a heterogeneous

Chapter 1 – Non-aqueous Sol-Gel Routes to Metal Oxides

sample where nanoparticles and nanorods coexist, showing a quite large size distribution.³⁸ If under the same reaction conditions benzyl alcohol is partly replaced by anisole acting as an inert solvent, short rods are formed. Finally, well defined nanowires are obtained when the benzyl alcohol content was further decreased to just traces.

In addition to oxides, benzyl alcohol was also used as solvent for the synthesis of metal phosphate nanocrystals and hybrid materials. Willinger *et al.* synthesized nanocrystalline titanium, zirconium, vanadium, yttrium and lanthanide phosphates at a yield above 90% from metal chlorides and/or alkoxides in benzyl alcohol in the presence of anhydrous phosphoric acid.⁶⁶ The synthesized lanthanide phosphates show high emission efficiencies when doped with terbium, proving the good crystalline quality of the as-synthesized nanocrystals. Bilecka *et al.*⁶⁷ and Yang *et al.*⁶⁸ synthesized LiFePO_4 for application in Li ion batteries. Finally, Di *et al.* showed that the approach can also be used to produce highly luminescent rare earth phosphonate hybrid nanostructures.⁶⁹

Moreover, this reaction protocol allows the formation of composite materials. Very recently, the fast deposition of a thin layer of metal oxide nanoparticles on diverse substrates by MW-assisted process was exploited for the formation of Fe_3O_4 /graphene and SnO_2 /graphene composites, which proved to be excellent negative electrodes for Li-ion batteries,⁷⁰ as well as for the preparation of Fe_2O_3 catalyst for the growth of vertically aligned CNTs.⁷¹

The reducing power of the benzyl alcohol seems to be the main limitation of the versatility of the approach. Cations sensitive towards reduction to the respective metals cannot be used. A typical example is the attempted synthesis of lead oxide or lead titanate, where lead(II) is reduced to metallic lead. In these cases alternative non reductive solvents, such as ketones, can be used.⁷²

3 Doping in NHSG

The previous section illustrated the variety of possible structures and complex materials achievable through the benzyl alcohol route. The mentioned asset given from the reduced reactivity of metal precursors in such a media offers the opportunity to play around with different reaction parameters (*i.e.* time and temperature of the reaction as well as nature and concentration of the precursors) in order to obtain phase pure multi-component oxides and, in particular, doped metal oxide.

The intentional introduction of impurities in the oxide matrix has been widely explored as it permit to tailor the pristine material supplying stability toward particular phases or structures, tuning the electrical or ionic conductivity, improving the catalytic activity or more simply introducing properties not intrinsic to the pure material.

With this aim, the benzyl alcohol route as been exploited leading to the preparation of various systems mainly focusing on 3d-block elements as adulterant ions: TM-doped ZnO,^{38,73-74} Mn-doped ZrO₂,⁷⁵ Co- and Fe-doped TiO₂⁷⁶ and very recently of Co-doped HfO₂.⁷⁷ Other materials obtained are Eu-doped ZrO₂⁷⁸⁻⁷⁹ and Y₂O₃.⁵⁹ Ln-doped RE₂O₃ were synthesized in benzyl alcohol^{60,80} as well as in 4-biphenyl methanol,⁸¹ allowing the tuning of the distance between the inorganic layers of the as-prepared lamellar hybrid material. Several alkaline earths were also investigated as dopant in LaMnO₃ perovskite.⁸² Recently, Rauwel *et al.* claimed the synthesis of CaHfO₃ and SrHfO₃ nanoparticles which can be however considered a lime stabilized hafnia.⁸³⁻⁸⁴

4 Conclusion and Layout of the Manuscript

In this introduction the versatility of non-aqueous sol-gel chemistry, under solvothermal conditions, for the synthesis of metal oxide nanostructures was introduced.⁷ Particular emphasis was put on the case of doped metal oxides in order to highlight one of the most promising advantages of these chemical routes. That is, the possibility to easier match the reactivity of the metal complexes and of the

Chapter 1 – Non-aqueous Sol-Gel Routes to Metal Oxides

dopants compared to aqueous systems. As a matter of fact, some of the materials discussed, up to now were only accessible by high temperature solid state reactions. In spite of the recent progress in nanomaterials chemistry research, it is not yet possible to prepare a certain compound on the nanoscale with a desired composition, structure, size and morphology, intentionally and in a predicted way. One of the reasons is the fact that it is not yet possible to predict the reactivity of metal complexes in a particular solvent.

As a typical example, solid solution of indium tin oxide nanoparticles, in the full range of concentrations, could be synthesized in benzyl alcohol starting from Sn(IV) alkoxides and In(III) acetylacetonate.^{53,85-86} The same could not be achieved using In(III) alkoxides instead because in this case, the different reactivity of the two metal complexes does not permit the formation of a solid solution.⁸⁷⁻⁸⁸ Indeed, in a particular solvent the metal oxide formation is influenced by various additional effects such as intermediate products formed during the reaction, side reactions and catalytic effects of the metal centers, the metal oxide seeds and early formed nanoparticles.

The studies reported in this thesis can be seen as a step forward towards a rational approach to multi-metal and, in particular, on doped metal oxide nanocrystals. The previous section showed some advances done in the last few years on the field of doped metal oxides via NHSG methods. However, there are still plenty of possibilities to exploit the advantages offered by such a versatile synthetic approach. Biomedical applications, long life batteries, spintronic devices, and solar cell, for example are constantly in need for advanced material or new synthetic approaches.

During the Ph.D. work diverse compounds for a wide spectrum of applications were investigated, seeking for a simple and straightforward protocol to an engineered synthesis of complex metal oxides. In this thesis, after a brief discussion of the different analytical techniques used, the systems studied are presented. Chapter 3 focuses on the doping of zirconia, hafnia and various perovskites with transition metals and the study of their magnetic properties. Dopant precursors of different nature are used to investigate the effect of their ligand and oxidation states on the final compound. The know-how gained with the study of these systems was applied

for the synthesis of rare earth doped zirconium oxide. In Chapter 4 the preparation of such compounds and the investigation of Y-doped ZrO_2 as electrolyte for fuel cell applications is described. The material demonstrated enhanced sinterability and great potential upon a slight powder manipulation. A further extension, proving the solidity of the synthetic method, is shown in Chapter 5 in which the preparation of $\text{Li}_4\text{Ti}_5\text{O}_{12}$ nanocrystals carrying excellent electrochemical properties for lithium-ion battery applications is discussed. One of the main advantages of NHSG routes compared to hydrolytic methods, that is the production of crystalline particles without the need of post-synthesis thermal treatments, allowed to obtain hybrid materials and assembly of ligand functionalized nanoparticles into tridimensional ordered superstructures. Modifying the reaction parameters (*i.e.* varying temperature and doping concentration) permitted to fabricate ordered and densely packed supercrystals presenting hexagonal, cubic or rhombohedral lattices in which the nanoparticles are attached together by an *in situ* formed organic glue.

5 Bibliography

- (1) Alivisatos, A. P. *The Journal of Physical Chemistry* **1996**, *100*, 13226.
- (2) Burda, C.; Chen, X.; Narayanan, R.; El-Sayed, M. A. *Chemical Reviews* **2005**, *105*, 1025.
- (3) Schmid, G. *Nanoparticles. From Theory to Application*; Wiley-VCH: Weinheim, 2004.
- (4) Eychmüller, A. *The Journal of Physical Chemistry B* **2000**, *104*, 6514.
- (5) Pinna, N.; Niederberger, M. *Angewandte Chemie International Edition* **2008**, *47*, 5292.
- (6) Niederberger, M.; Garnweitner, G. *Chemistry - A European Journal* **2006**, *12*, 7282.
- (7) Niederberger, M.; Pinna, N. *Metal Oxide Nanoparticles in Organic Solvents*; Springer London, 2009.
- (8) Wang, Y. W.; Xu, H. Y.; Wang, H.; Zhang, Y. C.; Song, Z. Q.; Yan, H.; Wan, C. R. *Solid State Ionics* **2004**, *167*, 419.
- (9) Inoue, M.; Tanino, H.; Kondo, Y.; Inui, T. *Journal of the American Ceramic Society* **1989**, *72*, 352.
- (10) Inoue, M.; Kominami, H.; Inui, T. *Research on Chemical Intermediates* **1998**, *24*, 571.
- (11) Kubo, K.; Hosokawa, S.; Furukawa, S.; Iwamoto, S.; Inoue, M. *Journal of Materials Science* **2008**, *43*, 2198.
- (12) Iwamoto, S.; Saito, K.; Inoue, M.; Kagawa, K. *Nano Letters* **2001**, *1*, 417.
- (13) Nakamura, T.; Inui, T.; Inoue, M.; Miyake, T. *Journal of Materials Science* **2006**, *41*, 4335.
- (14) Inoue, M. *Journal of Physics: Condensed Matter* **2004**, *16*, S1291.
- (15) Inoue, M.; Kimura, M.; Inui, T. *Chemistry of Materials* **1999**, *12*, 55.
- (16) Inoue, M.; Kominami, H.; Inui, T. *J. Chem. Soc., Dalton Trans.* **1991**, 3331
- (17) Pansanga, K.; Mekasuwandumrong, O.; Panpranot, J.; Prasertdam, P. *Korean Journal of Chemical Engineering* **2007**, *24*, 397.
- (18) Inoue, M.; Kimura, M.; Inui, T. *chemical Communications* **1999**, 957.
- (19) Kim, S.-W.; Iwamoto, S.; Inoue, M. *Ceramics International* **2009**, *35*, 1603.
- (20) Kobayashi, T.; Hosokawa, S.; Iwamoto, S.; Inoue, M. *Journal of the American Ceramic Society* **2006**, *89*, 1205.
- (21) Yin, S.; Akita, S.; Shinozaki, M.; Li, R.; Sato, T. *Journal of Materials Science* **2008**, *43*, 2234.
- (22) Julián-López, B.; Martos, M.; Ulldemolins, N.; Odriozola, J., A. ; Cordoncillo, E.; Escribano, P. *Chemistry - A European Journal* **2009**, *15*, 12426.
- (23) Arnal, P.; Corriu, R. J. P.; Leclercq, D.; Mutin, P. H.; Vioux, A. *Journal of Materials Chemistry* **1996**, *6*, 1925
- (24) Lian, S.; Wang, E.; Gao, L.; Wu, D.; Song, Y.; Xu, L. *Materials Research Bulletin* **2006**, *41*, 1192.
- (25) Ye, Y.; Yuan, F.; Li, S. *Materials Letters* **2006**, *60*, 3175.

- (26) Garnweitner, G.; Niederberger, M. *Journal of Materials Chemistry* **2008**, *18*, 1171.
- (27) Vioux, A. *Chemistry of Materials* **1997**, *9*, 2292.
- (28) Mutin, P. H.; Vioux, A. *Chemistry of Materials* **2009**, *21*, 582.
- (29) Niederberger, M.; Bartl, M. H.; Stucky, G. D. *Journal of the American Chemical Society* **2002**, *124*, 13642.
- (30) Niederberger, M.; Antonietti, M.; Rao, C. N. R., Muller, A., Cheetham, A. K., Eds.; Wiley-VCH: Weinheim, 2007.
- (31) Ba, J.; Polleux, J.; Antonietti, M.; Niederberger, M. *Advanced Materials* **2005**, *17*, 2509.
- (32) Pinna, N.; Garnweitner, G.; Antonietti, M.; Niederberger, M. *Advanced Materials* **2004**, *16*, 2196.
- (33) Zhou, S.; Garnweitner, G.; Niederberger, M.; Antonietti, M. *Langmuir* **2007**, *23*, 9178.
- (34) Garnweitner, G.; Goldenberg, L.; Sakhno, O.; Antonietti, M.; Niederberger, M.; Stumpe, J. *Small* **2007**, *3*, 1626.
- (35) Pinna, N.; Antonietti, M.; Niederberger, M. *Colloids and Surfaces A: Physicochemical and Engineering Aspects* **2004**, *250*, 211.
- (36) Pinna, N.; Neri, G.; Antonietti, M.; Niederberger, M. *Angewandte Chemie International Edition* **2004**, *43*, 4345.
- (37) Garnweitner, G., University of Potsdam, 2005.
- (38) Clavel, G.; Willinger, M. G.; Zitoun, D.; Pinna, N. *Advanced Functional Materials* **2007**, *17*, 3159.
- (39) Bilecka, I.; Djerdj, I.; Niederberger, M. *Chemical Communications* **2008**, *3*.
- (40) Bilecka, I.; Elser, P.; Niederberger, M. *ACS Nano* **2009**, *3*, 467.
- (41) Joo, J.; Kwon, S. G.; Yu, J. H.; Hyeon, T. *Advanced Materials* **2005**, *17*, 1873.
- (42) Du, H.; Yuan, F.; Huang, S.; Li, J.; Zhu, Y. *Chemistry Letters* **2004**, *33*, 770.
- (43) Djerdj, I.; Arcon, D.; Jaglicic, Z.; Niederberger, M. *J. Phys. Chem. C* **2007**, *111*, 3614.
- (44) Willis, A. L.; Chen, Z.; He, J.; Zhu, Y.; Turro, N. J.; Brien, S. *Journal of Nanomaterials* **2007**, 2007.
- (45) Pinna, N.; Grancharov, S.; Beato, P.; Bonville, P.; Antonietti, M.; Niederberger, M. *Chem. Mater.* **2005**, *17*, 3044.
- (46) Gotic, M.; Music, S. *European Journal of Inorganic Chemistry* **2008**, 2008, 966.
- (47) Pinna, N.; Garnweitner, G.; Antonietti, M.; Niederberger, M. *Journal of the American Chemical Society* **2005**, *127*, 5608.
- (48) Niederberger, M.; Garnweitner, G.; Buha, J.; Polleux, J.; Ba, J.; Pinna, N. *Journal of Sol-Gel Science and Technology* **2006**, *40*, 259.
- (49) Niederberger, M.; Garnweitner, G.; Ba, J.; Polleux, J.; Pinna, N. *International Journal of Nanotechnology* **2007**, *4*, 19.
- (50) Gubert, M. *Compt. Rend.* **1902**, *135*, 172.
- (51) Gubert, M. *Compt. Rend.* **1908**, *146*, 298.
- (52) Niederberger, M.; Garnweitner, G.; Pinna, N.; Antonietti, M. *J. Am. Chem. Soc.* **2004**, *126*, 9120.

Chapter 1 – Non-aqueous Sol-Gel Routes to Metal Oxides

- (53) Niederberger, M.; Pinna, N.; Polleux, J.; Antonietti, M. *Angewandte Chemie International Edition* **2004**, *43*, 2270.
- (54) Garnweitner, G.; Niederberger, M. *Journal of the American Ceramic Society* **2006**, *89*, 1801.
- (55) Yu, S.-H.; Pucci, A.; Hertrich, T.; Willinger, M.-G.; Baek, S.-H.; Sung, Y.-E.; Pinna, N. *Journal of Materials Chemistry* **2011**, *21*, 806.
- (56) Pinna, N.; Karmaoui, M.; Willinger, M.-G. *Journal of Sol-Gel Science and Technology* **2011**, *57*, 323.
- (57) Pinna, N. *Journal of Materials Chemistry* **2007**, *17*, 2769.
- (58) Sanchez, C.; Soler-Illia, G. J. d. A. A.; Ribot, F.; Lalot, T.; Mayer, C. R.; Cabuil, V. *Chemistry of Materials* **2001**, *13*, 3061.
- (59) Pinna, N.; Garnweitner, G.; Beato, P.; Niederberger, M.; Antonietti, M. *Small* **2005**, *1*, 112.
- (60) Karmaoui, M.; Sa Ferreira, R. A.; Mane, A. T.; Carlos, L. D.; Pinna, N. *Chemistry of Materials* **2006**, *18*, 4493.
- (61) Karmaoui, M.; Sá Ferreira, R. A.; Carlos, L. D.; Pinna, N. *Materials Science and Engineering: C* **2007**, *27*, 1368.
- (62) Karmaoui, M.; Willinger, M. G.; Mafra, L.; Hertrich, T.; Pinna, N. *Nanoscale* **2009**, *1*, 360.
- (63) Polleux, J.; Pinna, N.; Antonietti, M.; Niederberger, M. *J. Am. Chem. Soc.* **2005**, *127*, 15595.
- (64) Polleux, J.; Gurlo, A.; Barsan, N.; Weimar, U.; Antonietti, M.; Niederberger, M. *Angew. Chem., Int. Ed.* **2006**, *45*, 261.
- (65) Polleux, J.; Antonietti, M.; Niederberger, M. *J. Mater. Chem.* **2006**, *16*, 3969.
- (66) Willinger, M.-G.; Clavel, G.; Di, W.; Pinna, N. *J. Ind. Eng. Chem.* **2009**, *15*, 883.
- (67) Bilecka, I.; Hintennach, A.; Djerdj, I.; Novak, P.; Niederberger, M. *Journal of Materials Chemistry* **2009**, *19*, 5125.
- (68) Yang, H.; Wu, X.-L.; Cao, M.-H.; Guo, Y.-G. *The Journal of Physical Chemistry C* **2009**, *113*, 3345.
- (69) Di, W.; Ferreira, R. A. S.; Willinger, M.-G.; Ren, X.; Pinna, N. *The Journal of Physical Chemistry C* **2010**, *114*, 6290.
- (70) Baek, S.; Yu, S.-H.; Park, S.-K.; Pucci, A.; Marichy, C.; Lee, D.-C.; Sung, Y.-E.; Piao, Y.; Pinna, N. *RSC Advances* **2011**.
- (71) Silva, R. M.; Pucci, A.; Marichy, C.; Mata, D.; Ferro, M. C.; Silva, R. F.; Pinna, N. *CrystEngComm* **2012**, *14*, 48.
- (72) Garnweitner, G.; Hentschel, J.; Antonietti, M.; Niederberger, M. *Chem. Mater.* **2005**, *17*, 4594.
- (73) Bilecka, I.; Luo, L.; Djerdj, I.; Rossell, M. D.; Jagodic, M.; Jaglic, Z.; Masubuchi, Y.; Kikkawa, S.; Niederberger, M. *The Journal of Physical Chemistry C* **2011**, *115*, 1484.
- (74) Djerdj, I.; Garnweitner, G.; Arcon, D.; Pregelj, M.; Jaglicic, Z.; Niederberger, M. *Journal of Materials Chemistry* **2008**, *18*, 5208.
- (75) Clavel, G.; Willinger, M.-G.; Zitoun, D.; Pinna, N. *European Journal of Inorganic Chemistry* **2008**, *2008*, 863.

- (76) Djerdj, I.; Arcon, D.; Jaglicic, Z.; Niederberger, M. *Journal of Solid State Chemistry* **2008**, *181*, 1571.
- (77) Buha, J.; Arcon, D.; Niederberger, M.; Djerdj, I. *Physical Chemistry Chemical Physics* **2010**, *12*, 15537.
- (78) Ninjbadgar, T.; Garnweitner, G.; Börger, A.; Goldenberg, L., M. ; Sakhno, O.; Stumpe, J. *Advanced Functional Materials* **2009**, *19*, 1819.
- (79) Pucci, A.; Pinna, N. *Z. Naturforsch.* **2010**, *65*, 1015.
- (80) Sá Ferreira, R. A.; Karmaoui, M.; Nobre, S. S.; Carlos, L. D.; Pinna, N. *ChemPhysChem* **2006**, *7*, 2215.
- (81) Karmaoui, M.; Mafra, L.; SaFerreira, R. A.; Rocha, J.; Carlos, L. D.; Pinna, N. *J. Phys. Chem. C* **2007**, *111*, 2539.
- (82) Vazquez-Vazquez, C.; Arturo Lopez-Quintela, M. *Journal of Solid State Chemistry* **2006**, *179*, 3229.
- (83) Rauwel, E.; Galeckas, A.; Rauwel, P.; Fjellvåg, H. *Advanced Functional Materials* **2011**, n/a.
- (84) Clavel, G.; Pinna, N. *Advanced Functional Materials* **2012**.
- (85) Ba, J.; Feldhoff, A.; Rohlfing, D. F.; Wark, M.; Antonietti, M.; Niederberger, M. *Small* **2007**, *3*, 310.
- (86) Neri, G.; Bonavita, A.; Micali, G.; Rizzo, G.; Pinna, N.; Niederberger, M.; Ba, J. *Sensors and Actuators B: Chemical* **2008**, *130*, 222.
- (87) Pinna, N.; Niederberger, M.
- (88) Neri, G.; Bonavita, A.; Rizzo, G.; Galvagno, S.; Pinna, N.; Niederberger, M.; Capone, S.; Siciliano, P. *Sensors and Actuators B: Chemical* **2007**, *122*, 564.

Chapter 1 – Non-aqueous Sol-Gel Routes to Metal Oxides

CHAPTER 2
Techniques and Methods

Table of contents

1	The solvothermal synthesis	23
1.1	Zirconia	23
1.2	Hafnia	25
1.3	Perovskite	25
1.4	Lithium titanate	27
2	Characterization techniques	27
2.1	X-ray powder diffraction (XRD)	27
2.2	Electron microscopy (EM)	27
2.3	Electron paramagnetic resonance (EPR)	28
2.4	Superconducting quantum interference design magnetometry	28
2.5	X-ray absorption spectroscopy (XAS)	28
2.6	Small-angle X-ray scattering (SAXS)	29
2.7	Electrochemical characterizations	29
2.8	Dilatometry	30
2.9	Impedance spectroscopy	30
2.10	Other techniques	30
3	Bibliography	32

1 The solvothermal synthesis

Hafnium(IV) *tert*-butoxide 99.9% was purchased from Strem Chemicals. Zirconium(IV) isopropoxide isopropanol complex 99.9%, manganese(II) acetate 98%, manganese(II) acetylacetonate, manganese(III) acetylacetonate, chromium(III) acetylacetonate 99.99%, metallic barium 99% trace metals bases (tmb), titanium(IV) isopropoxide 99.999% (tmb), europium(III) acetate hydrate 99.9% (tmb), terbium(III) acetate hydrate 99.9% (tmb), gadolinium(III) acetylacetonate hydrate 99.9% (tmb), metallic lithium 99% (tmb), yttrium(III) chloride 99.99% (tmb), yttrium *isopropoxide* oxide, and benzyl alcohol 99%, were purchased from Aldrich. All the precursors were stored in a glove box and used as received.

%1 Zirconia

In a typical reaction of zirconia nanoparticles, a Teflon cup of 45 ml inner volume (a glass cup with inner volume of 35 ml was used for reaction temperature higher than 250 °C) was filled with 1.29 mmol of zirconium precursor, 20 ml of benzyl alcohol and an adequate quantity of dopant under an argon atmosphere (glove box). In the case of Y-doped zirconia the reaction was up-scaled to 8 g of zirconium precursor (20 mmol in 200 ml of benzyl alcohol) in order to cope with the larger amount of powder needed for impedance and mechanical analyses. The cup was slid into a steel autoclave, sealed, removed from the glove box and then heated for 2 days in a furnace at the required temperature, ranging between 230 and 350 °C (*cf.* Table 2.1 and Chapters 3, 4 and 6). The resulting suspensions were centrifuged and the precipitates were meticulously washed with ethanol (twice) and acetone and afterwards dried in air at 60 °C. As a general trend for low temperature reactions, the yield of the reaction is higher for pure zirconia samples and it decreases with the increasing of the dopant concentration (from 90% to 50%). Upon increasing the reaction temperature the yield is very high in all the cases, though part of it can be due to a higher concentration of organics (*cf.* below). Indeed, in some cases a yield

Chapter 2 – Techniques and Methods

higher than 100% was estimated. The powders are white or off-white for pure and rare earth doped oxides, green in the case of chromium and brown when Mn(II) and Mn(III) doping were added.¹⁻³ This kind of procedure is valid for the preparation of all the materials reported in the manuscript with the minor differences described below.

Table 2.1. Overview of studied zirconia samples, their yield and morphology (from XRD and TEM). *sample functionalized immediately after the reaction.

Matrix	Dopant	Nominal doping (mol%)	Temp (°C)	Time (day)	Yield (%)	Crystallite shape	Crystallite size (nm)
ZrO ₂	-	0	230	2	91	spherical	3.7
	Mn(ac) ₂	1	230	2	89	spherical	3.4
	Mn(ac) ₂	5	230	2	85	spherical	3.4
	Mn(ac) ₂	10	230	2	70	spherical	3.5
	Mn(acac) ₂	10	230	2	82	spherical	3.3
	Mn(acac) ₃	10	230	2	55	spherical	2.8
	Mn(ac) ₂	15	230	2	60	spherical	3.5
	Cr(acac) ₃	1	230	2	81	spherical	2.9
	Cr(acac) ₃	10	230	2	66	spherical	3.0
	Cr(acac) ₃	15	230	2	51	spherical	3.0
	Eu(ac) ₃ .H ₂ O	11	275	3	65.9	spherical	3.0
	Eu(ac) ₃ .H ₂ O	13	275	3	-	spherical	3.1
	Eu(ac) ₃ .H ₂ O	15	275	3	57.6	spherical	3.0
	Eu(ac) ₃ .H ₂ O	17	275	3	-	spherical	3.1
	Eu(ac) ₃ .H ₂ O	20	275	3	53.2	spherical	3.1
	Eu(ac) ₃ .H ₂ O	23	275	3	82.7	spherical	3.2
	Tb(ac) ₃ .H ₂ O	3	275	3	36.5	spherical	3.0
	Tb(ac) ₃ .H ₂ O	5	275	3	50.4	spherical	3.0
	Tb(ac) ₃ .H ₂ O	10	275	3	90.2	spherical	3.1
	Tb(ac) ₃ .H ₂ O	10	300	3	*	spherical	3.0
	Tb(ac) ₃ .H ₂ O	10	325	3	*	spherical	3.1
	Tb(ac) ₃ .H ₂ O	10	350	3	*	spherical	2.9
	-	0	300	2	-	spherical	-
	-	0	325	2	-	spherical	4.4
	-	0	350	2	-	spherical	4.4
	Y ₅ (iPrO) ₁₃ O	5.8	250	2	100	spherical	4.1
	Y ₅ (iPrO) ₁₃ O	5.8	300	2	110	spherical	4.1
	Y ₅ (iPrO) ₁₃ O	5.8	350	2	118	spherical	4.3
	Y ₅ (iPrO) ₁₃ O	14.2	250	2	90	spherical	3.3
	Y ₅ (iPrO) ₁₃ O	14.2	300	2	104	spherical	3.5
Y(Cl) ₃	14.2	300	2	100	spherical	6.0	

%2 Hafnia

For hafnia samples, a Teflon cup of 23 ml inner volume was filled with 1.06 mmol of hafnium(IV) *tert*-butoxide, 12 ml of benzyl alcohol and an adequate quantity of dopant. The reaction solution was heated to 250 °C for 2 days and finally washed with the same method previously described. The same trends as in the case of zirconia were observed in colors and yield (from 65 to 20%, cf. Table 2.2).^{3,4}

Table 2.2. Overview of studied hafnia samples, their yield and morphology (from XRD).

Matrix	Dopant	Nominal doping (mol%)	Temperature (°C)	Time (day)	Yield (%)	Crystallite shape	Crystallite size (nm)
HfO ₂	-	0	250	2		ellipsoidal	-
	Mn(acac) ₃	1	250	2	46	ellipsoidal	-
	Mn(acac) ₃	3	250	2	42	ellipsoidal	-
	Mn(acac) ₃	4	250	2	43	ellipsoidal	-
	Mn(acac) ₃	10	250	2	49	faceted pseudo spherical	2.8
	Mn(ac) ₂	15	250	2	65	faceted pseudo spherical	2.9
	Mn(acac) ₂	15	250	2	31	faceted pseudo spherical	3.0
	Mn(acac) ₃	15	250	2	42	faceted pseudo spherical	2.7
	Cr(acac) ₃	1	250	2	55	ellipsoidal	-
	Cr(acac) ₃	10	250	2	36	ellipsoidal	-
	Cr(acac) ₃	15	250	2	26	ellipsoidal	-

%3 Perovskite

1.30 mmol of barium metal were stirred in 20 ml of benzyl alcohol for 6h at 80 °C till complete dissolution. During the oxidation process some hydrogen gas was released.

Chapter 2 – Techniques and Methods

Upon reached a clear solution $\text{Ti}(\text{O}/\text{Pr})_4$ (or zirconium isopropoxide isopropanol complex) and the dopant precursor ($\text{Mn}(\text{acac})_3$ or $\text{Cr}(\text{acac})_3$), in the case of non pure samples, were added in a quantity so that their total number of mol were equivalent to those of barium. Indeed, the doping was considered to substitute only the six-fold coordinated B site of the perovskite structure ($\text{A}_1\text{B}_{1-x}\text{D}_x\text{O}_3$). The solution was reacted at 200 °C for 6 days as similarly described from Niederberger *et al*^{5,6} (Table 2.3).

The color of BaTiO_3 and BaZrO_3 powders is white but turns yellowish when doped with manganese and pale-green when doped with chromium. The yield of the reaction is very diverse depending on the system: The yield of the titanate compounds is rather high when doped with Mn while the addition of Cr ion in the reaction pot leads to a drop of the yield in all the cases below 30%. The zirconates do not show such a divergence adding different dopants; on the contrary, they behave similarly to the binary systems described above with a yield of 60% for the low doped samples down to 25% when increasing the quantity of dopant.

Table 2.3. Overview of studied perovskite samples, their yield and morphology (from XRD).

Matrix	Dopant	Nominal doping (mol%)	Temperature (°C)	Time (day)	Yield (%)	Crystallite shape	Crystallite size (nm)
BaZrO_3	-	0	200	6	53	irregular	1.9
	$\text{Mn}(\text{acac})_3$	1	200	6	58	irregular	1.7
	$\text{Mn}(\text{acac})_3$	5	200	6	31	irregular	1.9
	$\text{Cr}(\text{acac})_3$	1	200	6	63	irregular	1.6
	$\text{Cr}(\text{acac})_3$	5	200	6	26	irregular	1.8
BaTiO_3	-	0	200	6	N/A	pseudospherical	5
	$\text{Mn}(\text{acac})_3$	1	200	6	82	pseudospherical	5
	$\text{Mn}(\text{acac})_3$	3	200	6	76	pseudospherical	4
	$\text{Mn}(\text{acac})_3$	5	200	6	87	pseudospherical	4
	$\text{Cr}(\text{acac})_3$	5	200	6	30	pseudospherical	4
	$\text{Cr}(\text{acac})_3$	10	200	6	10	pseudospherical	3.5
	$\text{Cr}(\text{acac})_3$	15	200	6	29.5	pseudospherical	N/A

%4 Lithium titanate

50 mg (7.2 mmol) of metallic lithium were stirred in 20 ml of benzyl alcohol at 50 °C. Even in this case hydrogen evolution was observed and within 4 h all metal was oxidized and a clear, slightly yellowish solution was obtained. This reaction mixture was transferred into a Teflon-lined steel autoclave under the addition of 2.16 g (7.6 mmol) of $\text{Ti}(\text{O}/\text{Pr})_4$. Alternatively, a sample with a lithium:titanium ratio of 8.5:8 mmol was also prepared. The sealed autoclave was heated in an electric furnace at 250 °C for 2 days. Finally, 0.70 g of a white powder were obtained, accounting for an overall reaction yield of above 85%.⁷

2 Characterization techniques

&1 X-ray powder diffraction (XRD)

The X-ray powder diffraction (XRD) data were collected on an X'Pert MPD Philips diffractometer (CuK_α X-radiation at 45 kV and 40 mA, no monochromator). The patterns were measured in the 2θ range from 3.00 to 75.00° with a scanning step of 0.20°. The average crystallite size was estimated by applying the Scherrer formula.⁸

&2 Electron microscopy (EM)

Transmission electron microscopy (TEM) was carried out on a Hitachi H-9000 microscope operating at 300 kV, high resolution TEM and electron energy loss spectroscopy (EELS) measurements were performed using either a CM200FEG (Philips) microscope with a field emission gun and a GATAN Tridiem GIF or a JEOL 2200FS with a field emission gun and an omega filter. The microscopes were operated at 200 kV. Samples were prepared by depositing a drop of an

Chapter 2 – Techniques and Methods

ultrasonification-assisted suspension of particles in ethanol on a copper grid coated with an amorphous carbon film.

Scanning electron microscopy (SEM) investigations were carried using a HR-SEM Hitachi SU-70 and a Hitachi S-4800 operated between 2 and 30 kV acceleration voltage. The images were collected in secondary electron mode. Related technique such as energy-dispersive X-ray spectroscopy (EDX), EELS and selected area electron diffraction (SAED) were also used.

&3 Electron paramagnetic resonance (EPR)

The EPR experiments were performed at X band ~ 9.5 GHz on a Bruker ESP300 spectrometer with microwave powers between 0.02 and 200 mW. Temperature studies from 6 to 300 K were carried out using an Oxford gas-flow cryostat.

&4 Superconducting quantum interference design magnetometry

Magnetic properties were measured using a Superconducting Quantum Interference Design (SQUID) magnetometer MPMS XL7, in the range of temperature 2-350 K and of field 0-5 T. The temperature-dependent susceptibility was measured using DC procedure. The sample was cooled to 2 K under zero magnetic field, low magnetic field (5 mT) was then applied and data collected from 2 K to 350 K (zero-field cooled, ZFC). Field Cooled (FC) measurements were performed from 2 K to 350 K with an applied field (generally 0.5 T) during the cooling.

&5 X-ray absorption spectroscopy (XAS)

The Extended X-ray Absorption Fine Structure (EXAFS) and X-ray Absorption Near Edge Structure (XANES) measurement were carried out at the beamline N° 29 of the European Synchrotron Radiation Facility (ESRF) of Grenoble, France.⁹ X-ray absorption spectra (XAS) were measured at the Mn and Cr K-edge in transmission and fluorescence yield modes. For edge energy calibration, a XAS spectrum of MnO, Mn₂O₃ and MnO₂ and of Cr₂O₃ and CrO₂ were measured as a reference. The tests

where carried out on pelletized mixture of a few mg of sample (around 10 mg, depending on the concentration of the dopant) and 100 mg of BN.

&6 Small-angle X-ray scattering (SAXS)

The Small Angle X-ray Scattering experiments were carried out at station I22, Diamond Light Source at Oxford, UK,¹⁰ and at European Synchrotron Radiation Facility (ESRF) of Grenoble, France.⁹ The wavelength used was 0.065 Å. 2-dimensional SAXS patterns were recorded using a Mar165 CCD detector, and converted to 1-d curves by radial averaging.

The measurement of the positions and intensities of the diffraction peaks was carried out using Galactic PeakSolveTM program, where experimental diffractograms are fitted using Gaussian shaped peaks. The diffraction peaks are indexed on the basis of their peak positions, and the lattice parameters and the space groups are subsequently determined.

&7 Electrochemical characterizations

The working electrode was prepared from the LTO powder, Super P (as a conducting agent) and polyvinylidene fluoride (PVdF, as a binder) (70:10:20 in weight ratio) in *n*-methyl-2-pyrrolidinone (NMP) solvents. The slurry was coated on an aluminum current collector using a blade and then pressed for use as the working electrode. Electrochemical test cells were assembled in an argon-filled glove box using coin-type half cells (2016 type) with lithium foil as a counter electrode. 1.0 M solution of LiPF₆ in a mixture of ethylene carbonate (EC) and dimethylene carbonate (DMC) (1:1 in volume ratio) as the organic electrolyte. The cells were galvanostatically charged and discharged in the voltage range from 2.5 to 1 V vs Li/Li⁺. For the rate performance measurement, the current was varied from 1 C (0.175 A/g) to 30 C (5.25 A/g). The cycle performance for 200 cycles was recorded at 1 C rate. All the electrochemical measurements were made with a TOSCA-3100 battery cycler (Toyo Co., Japan) at room temperature.

&8 Dilatometry

The absolute and differential dilatometry measurements were carried out with a Linseis GmbH adidi 4.0 dilatometer equipped with a type B thermocouple and alumina measurement system. The analyses were done under air heating at 5 °C/min up to 1500 °C.

&9 Impedance spectroscopy

Impedance studies were carried out to investigate the conductivity of the ceramic materials and in particular to assess the resistive contributions of the interior of the grains (bulk) and of the grain boundaries. Platinum electrodes were painted on both sides of the pellets and subsequently sintered at 1000 °C for 10 min to gain the necessary mechanical resistance. The measurements were performed in the frequency range between 20 and 10^6 Hz with a test signal amplitude of 1 V in air and for temperatures between 200 and 1000 °C using a HP 4284A precision LCR meter. Impedance spectra were fitted to equivalent circuits using ZView (version 2.6b, 1990–2002, Scribner Associates) in order to assess bulk and grain boundary contributions.

&10 Other techniques

Rapid thermal annealing was carried out on a JIPELEC JETFIRST 100 instrument. The powders pressed into pellets were heated for 30 seconds under pure oxygen using a ramp of 20 seconds.

Carbon, hydrogen, and nitrogen elemental analysis (CHN) were performed using a CHNS-932 elemental analyzer with standard combustion conditions and handling of the samples in air.

Inductively Coupled Plasma-Atomic Emission Spectrometry (ICP-AES) was realized in the analytical laboratory of University of Aveiro.

The diffuse reflectance spectroscopy was performed on Jason V-560 UV-Vis spectrophotometer.

The Brunauer–Emmett–Teller (BET) surface area was determined using a Micromeritics ASAP 2000 nitrogen adsorption apparatus. All the samples were degassed at 100 °C prior to BET measurements.

For evaluation of the formation mechanism, the reaction solution obtained by centrifugation of the solid material was subjected to NMR and GC-MS analysis. ¹H and ¹³C NMR spectra were recorded in a 600 MHz, AVANCE 600 on a 5 mm CPTXI ¹H probe at, respectively, 600.13 and 150.90 MHz.

The organics left attached to the surface of the particles upon drying were analyzed by means of solid state NMR on a BRUKER AVANCE 400 spectrometer equipped with a 2.5 mm CP/MAS probe.

GC-MS analysis was performed on a JEOL JMS600 gas chromatographer equipped with a 30 m x 0.3 mm i.d. fused silica column from HP Company. Helium was used as carrier gas (flow rate of 1 ml/min) and ca. 1 μL of the sample diluted with hexane was injected. The injector temperature was 270 °C. The oven temperature was maintained isothermal at 50 °C for 1 min, and then increased by 20 °C /min from 50 to 250 °C, which was held isothermal for 10 min. The interface temperature was 320 °C, the ion source temperature was 150 °C, the electron energy was 70 eV, the filament current was 200 μA, and the scan rate of the mass spectrometer was 1.0 s/scan over the m/z range of 50 - 700. Methane-chemical ionization mass spectra were recorded with a source temperature of 120 °C and a source pressure 1 x 10³ Pa.

Thermogravimetric analyses and differential scanning calorimetries (TGA/DSC) were carried out with a SATARAM Labsys TG-DSC 12 operated on air at 10 °C/min up to 1000 °C.

Fourier transform infrared spectroscopy (FT-IR, Spectrum BX, Perkin Elmer) was carried out in the range of 4000-350 cm⁻¹ in transmission mode. The pellets were prepared by adding 1-2 mg of the nanopowder to 200 mg of KBr. The mixture was then carefully mixed and compressed at a pressure of 10 KPa to form transparent pellets.

3 Bibliography

- (1) Garnweitner, G.; Niederberger, M. *Journal of the American Ceramic Society* **2006**, *89*, 1801.
- (2) Clavel, G.; Willinger, M.-G.; Zitoun, D.; Pinna, N. *European Journal of Inorganic Chemistry* **2008**, *2008*, 863.
- (3) Pucci, A.; Clavel, G.; Willinger, M.-G.; Zitoun, D.; Pinna, N. *The Journal of Physical Chemistry C* **2009**, *113*, 12048.
- (4) Pinna, N.; Garnweitner, G.; Antonietti, M.; Niederberger, M. *Advanced Materials* **2004**, *16*, 2196.
- (5) Niederberger, M.; Garnweitner, G.; Pinna, N.; Antonietti, M. *J. Am. Chem. Soc.* **2004**, *126*, 9120.
- (6) Niederberger, M.; Pinna, N.; Polleux, J.; Antonietti, M. *Angewandte Chemie International Edition* **2004**, *43*, 2270.
- (7) Yu, S.-H.; Pucci, A.; Hertrich, T.; Willinger, M.-G.; Baek, S.-H.; Sung, Y.-E.; Pinna, N. *Journal of Materials Chemistry* **2011**, *21*, 806.
- (8) Scherrer, P. *Göttinger Nachrichten Math. Phys.* **1918**, *2*, 98.
- (9) <http://www.esrf.eu/UsersAndScience/Experiments/ElectStructMagn/BM29>.
- (10) <http://www.diamond.ac.uk/>.

CHAPTER 3*

Transitional Metal Doped Oxides

*This chapter is partially based on: A. Pucci, G. Clavel, M.-G. Willinger, D. Zitoun, N. Pinna *J. Phys. Chem. C* **2009**, 113, 12048

Table of contents

1	Introduction	35
2	Result and Discussion	37
2.1	Synthesis.....	37
2.2	Structural and Morphological Characterization.....	39
2.2.1	ZrO₂	39
2.2.2	HfO₂	41
2.2.3	Perovskites	41
2.2.4	TEM	44
2.2.5	Diffuse reflectance	47
2.2.6	XAS	49
2.3	Annealing	50
2.4	Magnetic properties	53
2.4.1	EPR	53
2.4.2	Susceptibility Studies	58
3	Conclusions	63
4	Bibliography	65

1 Introduction

Various soft chemistry approaches have been introduced in the past decades for the synthesis of metal oxide nanoparticles.¹⁻⁵ They were reported extremely successful for the production of simple oxides (e.g. binary). Indeed, dozens of routes for the production of titanium and zinc oxide nanoparticles can be found in the recent literature. In contrast, approaches leading to the formation of multi-metal and doped metal oxides by soft chemistry approaches are more rarely reported. As discussed in the beginning of this thesis (*cf.* Chapter 1), one reason might be the fact that it is difficult to match the reactivity of the different metal precursors in solution, which can prevent the formation of multi-metal phases or the homogeneous doping of simple oxides.² This is especially true for aqueous routes (e.g. sol-gel) as the hydrolysis rates are generally fast and strongly depend on the metal center.⁶ To circumvent this problem, a large amount of work was reported on the modification of metal complexes, such as metal alkoxides, for the controlled decrease of their reactivity.⁷ Non-aqueous sol-gel routes were introduced for the same purpose, and in fact, the reactivity of the metal oxide precursors is greatly decreased under water exclusion, thus making it easier to control the metal oxide formation.^{8,9} This feature provide the best conditions for the investigation of ternary or more complex systems, such as doped metal oxides.

Doping is commonly used in materials science in order to tailor or introduce additional physical properties in a given material. For spintronic applications, devices combining magnetic storage capacity and the semiconducting properties, it is primordial to synthesize materials containing magnetic impurities, in the order of several mol%, homogeneously distributed and occupying well defined sites in the host matrix.¹⁰ Once again, non-aqueous routes and especially NHSG approaches have been successfully employed for the synthesis of various large band gap oxides doped with magnetic impurities such as Mn, Fe, and Co cations.¹¹⁻¹⁵

ZrO₂ and HfO₂ compounds were recently predicted ferromagnetic above room temperature when doped with transition metal ions.^{16,17} Although these materials

Chapter 3 – Transitional Metal Doped Oxides

have been synthesized and studied since decades, their magnetic properties have been rarely described.¹⁸⁻²²

On the same direction goes the attempt to introduce magnetic ions in perovskites. Many of the perovskite structures, *e.g.* those showing off-centered Ba^{2+} ions, are ferroelectric. The addition of TM impurity may induce ferromagnetic behavior in the perovskite matrix, obtaining a multiferroic coupling.^{23,24} The magneto-electric coupling can be achieved in composites but it's rather rare in single phase materials (*e.g.* rare-earth- and bismuth-based perovskites are among the few examples). In the last few years ferromagnetic properties were sought in doped ferroelectric perovskite, mainly focusing on the introduction of iron ions in the matrix.^{3,25-27}

Our group recently reported that zirconia can be homogeneously doped with Mn.¹³ In the present chapter, this preliminary work is extended and the synthesis and characterization of zirconia, hafnia and perovskite nanoparticles doped with Mn and Cr are presented. Above all, this work is focused on the detailed characterization of the doping behavior using various experimental methods ranging from diffraction techniques, analytical electron microscopy and ICP-AES to UV-Vis and X-ray absorption spectroscopy and also, by monitoring the magnetic properties of the obtained particles. We will show that an in-depth characterization is needed to understand the role of synthesis and annealing conditions (*i.e.* role of the oxide matrix, nature of metal ion and ligands) and the doping behavior (*e.g.* efficiency, homogeneity, oxidation state of the transition metal ions). The elucidation of these parameters is the basis for the development of rational synthesis approaches towards multi-metal and doped metal oxide nanoparticles.

2 Result and Discussion

2.1 Synthesis

The synthesis of the binary metal oxide nanoparticles involves the solvothermal reaction of zirconium isopropoxide or hafnium *tert*-butoxide with benzyl alcohol as it was previously reported for the formation of pure ZrO_2 ²⁸ and HfO_2 .²⁹ The condensation step leading to M-O-M bond formation follows the ether elimination mechanism. This particular non-hydrolytic condensation was discussed in the introduction of this manuscript (*cf.* Chapter 1, section 2.3.1). This approach leads to the formation of uniform spherical nanocrystals in the case of pure zirconia whereas the as-synthesized pure hafnia nanocrystals display an ellipsoidal morphology.

It has been demonstrated that benzyl alcohol can oxidize alkali and alkaline earth metals near room temperature forming a complex which is an optimum precursor for ternary metal oxide condensation reactions (*cf.* Chapter 1, section 2.3.3).³⁰⁻³² Indeed, the oxidation of barium metal in benzyl alcohol and the further addition of a metal precursor carrying an oxidation state of IV lead to the formation, after solvothermal synthesis, of nanocrystalline Ba-based perovskites. Very small crystalline titanate and zirconate particles were obtained by solvothermal reaction in benzyl alcohol.³³ In this chapter, we extend this synthetic protocol to the case of Mn or Cr doped ZrO_2 , HfO_2 , BaTiO_3 and BaZrO_3 .

The doping was performed by adding up to 15 mol% of manganese(II) acetate, manganese(II) acetylacetonate, manganese(III) acetylacetonate or chromium(III) acetylacetonate to the reaction mixture (*cf.* Chapter 2). The nanoparticles were synthesized at 200 °C for perovskites, at 230 °C for ZrO_2 and at 250 °C for HfO_2 . Depending on the nature of the dopant precursor used, the reaction leads to brown (manganese) or green (chromium) powders. The doping concentration after synthesis was monitored by ICP-AES measurements (Table 3.1a and b, and Table 3.2). The doping efficiency was calculated from the ratio between the dopant incorporated in

Chapter 3 – Transitional Metal Doped Oxides

the structure and the molecular precursor used during the synthesis. The effective values reported in the tables 3.1a and 3.1b show that Mn doping is more efficient than Cr doping. Further, higher values were obtained for HfO₂ as compared to ZrO₂, which is unexpected taking into account the similarities between the two oxides and it is probably due to the lower reaction yield obtained for hafnium oxide. Changing the dopant precursor resulted in a significant alteration of the doping efficiency. Replacing the acetate ligand by an acetylacetonate group enhanced the effectiveness despite a lower reaction yield.

Table 3.1a. Overview of studied Zirconia samples, their crystallographic phase (from XRD and TEM) and the obtained dopant concentration (from ICP).

Sample	Phase	Nominal doping [%]	Dopant precursor	Effective doping [%]
Zr _{0.992} Mn _{0.008} O _{2-δ}	Cubic	1	Mn(ac) ₂	80
Zr _{0.970} Mn _{0.030} O _{2-δ}	Cubic	5	Mn(ac) ₂	60
Zr _{0.955} Mn _{0.045} O _{2-δ}	Cubic	10	Mn(ac) ₂	45
Zr _{0.921} Mn _{0.079} O _{2-δ}	Cubic	10	Mn(acac) ₃	79
Zr _{0.920} Mn _{0.080} O _{2-δ}	Cubic	15	Mn(ac) ₂	53
Zr _{0.998} Cr _{0.002} O _{2-δ}	Cubic	1	Cr(acac) ₃	20
Zr _{0.980} Cr _{0.020} O _{2-δ}	Cubic	15	Cr(acac) ₃	13

Table 3.1b. Hafnia samples studied, crystallographic phase (from XRD and TEM) and dopant concentration obtained (from ICP).

Sample	Structure	Nominal doping [%]	Dopant precursor	Effective doping [%]
Hf _{0.890} Mn _{0.110} O _{2-δ}	Cubic	10	Mn(acac) ₃	110
Hf _{0.850} Mn _{0.150} O _{2-δ}	Cubic	15	Mn(ac) ₂	100
Hf _{0.840} Mn _{0.160} O _{2-δ}	Cubic	15	Mn(acac) ₂	107
Hf _{0.830} Mn _{0.170} O _{2-δ}	Cubic	15	Mn(acac) ₃	113
Hf _{0.996} Cr _{0.004} O _{2-δ}	Monoclinic	1	Cr(acac) ₃	40
Hf _{0.950} Cr _{0.050} O _{2-δ}	Monoclinic	10	Cr(acac) ₃	50
Hf _{0.930} Cr _{0.070} O _{2-δ}	Monoclinic	15	Cr(acac) ₃	47

2.2 Structural and Morphological Characterization

2.2.1 ZrO₂

The X-ray powder diffraction pattern of the as-synthesized ZrO₂ product corresponds to the cubic or the tetragonal phase. As already shown in a previous work, at the nanoscale, the surface free energy stabilizes the cubic phase of ZrO₂.¹³ However, they are impossible to discern just by mean of XRD. All the manganese-doped (Figure 3.1) and chromium-doped (Figure 3.3a) zirconia samples show broad diffraction peaks due to the nanometric size. Their position and relative intensity are in agreement with the proposed structures. All the samples studied (Table 3.1a) show no additional reflections that could be attributed to crystalline impurities. Using the Scherrer formula for the estimation of the crystallite size, we obtained particle diameters ranging from 3 to 4 nm (*cf.* Table 2.1 Chapter 2).

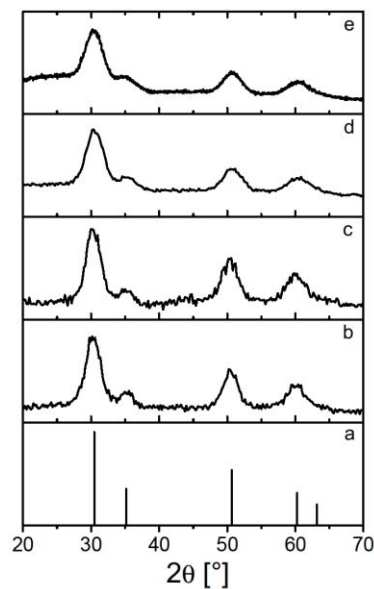


Figure 3.1: XRD patterns of a) expected reflection of cubic phase (vertical full line), b) Zr_{0.992}Mn_{0.008}O_{2-δ}, c) Zr_{0.970}Mn_{0.030}O_{2-δ}, d) Zr_{0.955}Mn_{0.045}O_{2-δ}, e) Zr_{0.920}Mn_{0.080}O_{2-δ}. NB: In all the XRD graphs presented in this thesis the ordinate axis shows the x-ray intensity in arbitrary units.

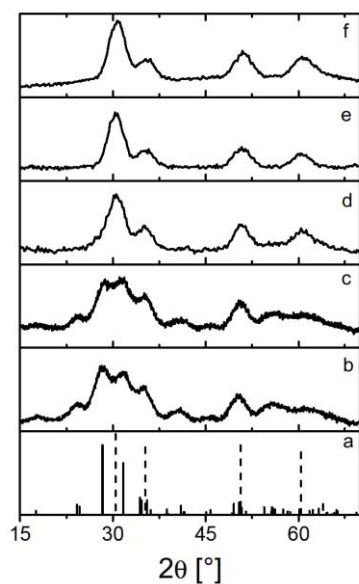


Figure 3.2: XRD patterns of a) expected reflection of cubic phase (vertical dashed line) and monoclinic phase (vertical full line); Mn-doped hafnia obtained adding 1 (b), 3 (c), 4 (d), 10 (e), and 15% (f) of manganese precursor.

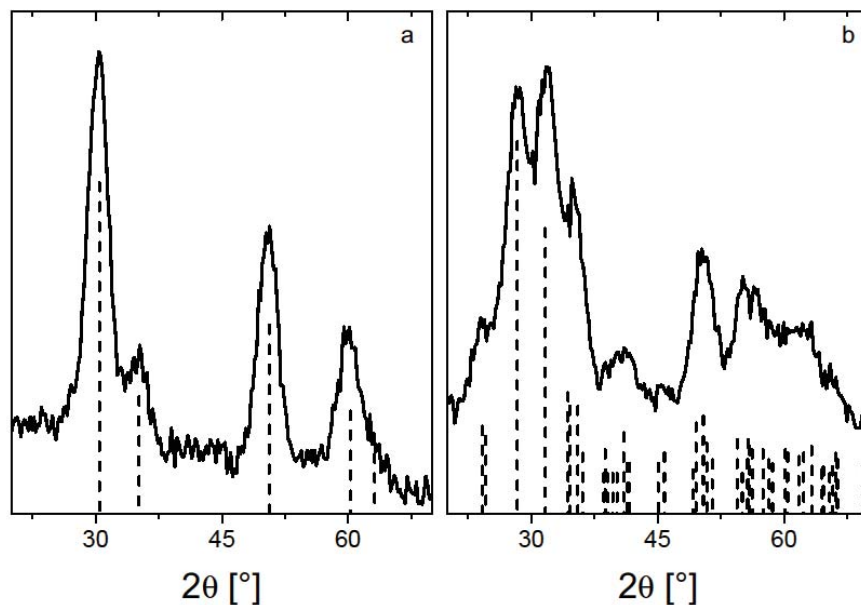


Figure 3.3: Typical XRD pattern of (a) Cr-doped ZrO_2 and the expected reflections of the cubic phase (vertical dashed line) and of (b) Cr-doped HfO_2 and the expected reflections of the monoclinic phase (vertical dashed line).

2.2.2 HfO₂

The solvothermal treatment of Hf alkoxide in benzyl alcohol leads to HfO₂ particles in monoclinic modification. The pattern of the pure hafnia nanoparticles, synthesized by this route, was analyzed using the Debye function.²⁹ It turned out that the reflections could be almost perfectly reproduced, in terms of intensity and peak positions, by single crystalline ellipsoidal nanoparticles (long diameter = 6 nm and short diameter = 3 nm) with the long axis parallel to the [100] crystallographic axis.

Upon doping hafnia, different phases could be stabilized depending on the dopant and its content. For loads of manganese precursor lower than 4%, the monoclinic phase is formed while for higher concentrations the cubic one is stabilized (Figure 3.2). As already observed for ZrO₂, manganese doping tends to stabilize the cubic phase. The introduction of chromium seems not to modify the crystal structure of pure HfO₂. Indeed, Cr-doped HfO₂ presents the monoclinic phase for all doping concentrations tested (Figure 3.3b). All the samples studied (Table 3.1b) show no additional reflections that could be attributed to the presence of secondary phases. The small dimension of the particles leads to broad and overlapping peaks for the monoclinic phase. For these samples, it was therefore not possible to use the Scherrer formula for an estimation of the crystalline size. However, as the aspect of the peaks corresponds to the one of the undoped samples²⁹ we can conclude that the size does not substantially vary upon doping.

2.2.3 Perovskites

The X-ray diffraction analysis on as-synthesized pure Ti-based perovskite sample (Fig. 3.4a and b solid line) shows a rather defined pattern which can be assigned to a BaTiO₃ phase.³⁰ This material can exist in five crystallographic modifications. The hexagonal modification can be ruled out due to the absence of some peculiar peaks (e.g. the reflection at 26.1° corresponding to the [103] direction, *cf.* JCPDS No. 8-372). The most likely structures are the cubic and the tetragonal (JCPDS No. 31-174

and 5-626, respectively) although it is not possible to discriminate between them due to the broadness of the peaks.³³ Considering the position of the reflections, orthorhombic and rhombohedral phases seem to be implausible although, again due to large peaks, they can be safely excluded only coupling these results with spectroscopy techniques (*e.g.* Raman and IR).

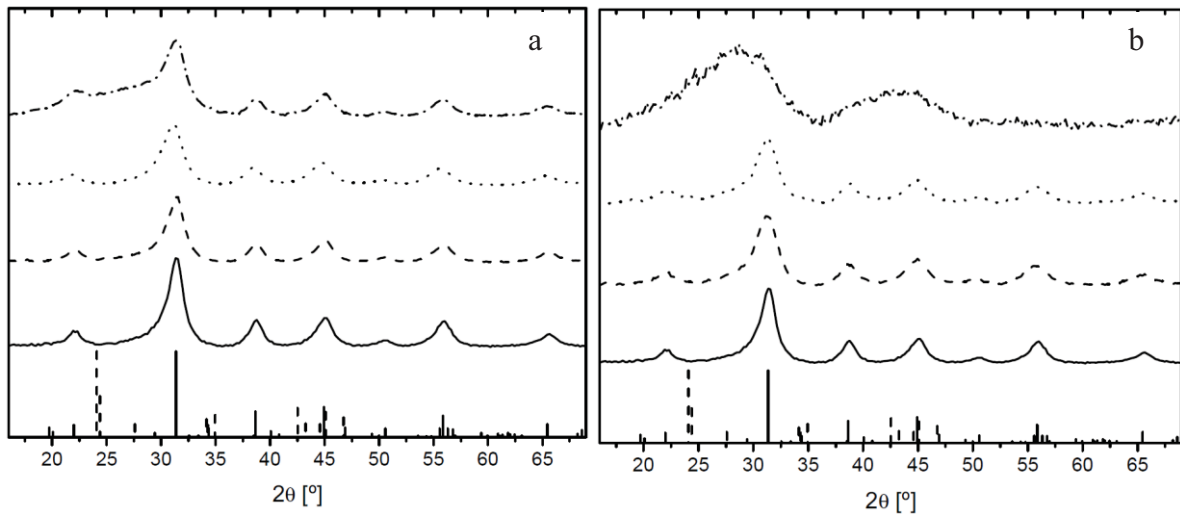


Figure 3.4: XRD pattern of pure (solid line) and 1% (dashed line), 3% (dotted line) and 5% (dashed-dotted line) Mn-doped BaTiO_3 (plot a) and pure (solid line) and 5% (dashed line), 10% (dotted line) and 15% (dashed-dotted line) Cr-doped BaTiO_3 (plot b). The vertical lines represent the expected reflection of BaTiO_3 and BaCO_3 (solid and dashed line, respectively).

The diffractograms of doped samples become less resolved with the increasing of the doping concentration due to a decreasing of the size or of the degree of crystallinity. Indeed, for the higher doped sample (15% Cr-doped BaTiO_3 , *cf.* figure 3.4b dashed-dotted line) no clear assignation is possible. The size of the particles calculated through the Scherrer formula is around 5 nm (*cf.* Table 2.3 in Chapter 2) for the pure sample and it decreases to a minimum size of 3.5 upon doping. In all the cases, the size calculated from the (111) reflection was slightly larger than the one calculated from the $(110)_C$ (or $(110)_T$ and $(101)_T$) peaks, suggesting a non spherical morphology.

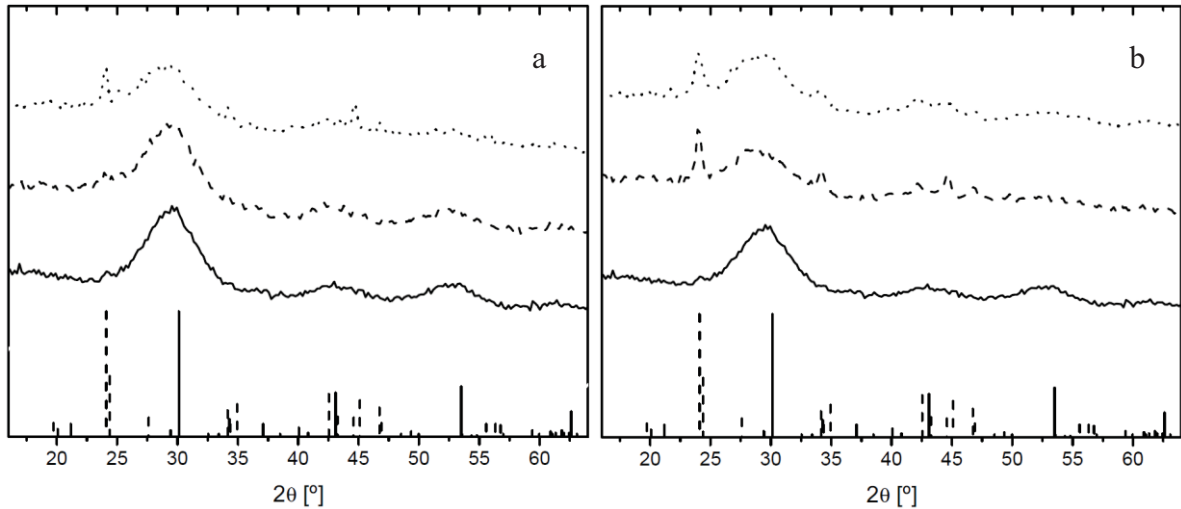


Figure 3.5: XRD pattern of pure (solid line) and 1% (dashed line) and 5% (dotted line) Mn- (a) and Cr- (b) doped BaZrO₃. The vertical lines represent the expected reflection of BaZrO₃ and BaCO₃ (solid and dashed line, respectively).

Table 3.2. Overview of studied perovskite samples, the obtained dopant concentration (from ICP) and the excess of B site atoms compared to the stoichiometry.

Sample	Nominal doping [%]	Dopant precursor	Effective doping [%]	Excess of B [%]
BaZrO ₃	0	-	-	-34
BaZrO ₃	1	Mn(acac) ₃	N/A	N/A
BaZrO ₃	5	Mn(acac) ₃	N/A	N/A
BaZr _{0.987} Cr _{0.013} O _{3-δ}	1	Cr(acac) ₃	130	-178
BaZr _{0.978} Cr _{0.022} O _{3-δ}	5	Cr(acac) ₃	44	-64
BaTiO ₃	0	-	-	-
BaTi _{0.985} Mn _{0.015} O _{3-δ}	1	Mn(acac) ₃	150	-1
BaTi _{0.972} Mn _{0.028} O _{3-δ}	3	Mn(acac) ₃	93	12
BaTi _{0.955} Mn _{0.045} O _{3-δ}	5	Mn(acac) ₃	90	18
BaTi _{0.971} Cr _{0.029} O _{3-δ}	5	Cr(acac) ₃	58	18
BaTi _{0.869} Cr _{0.131} O _{3-δ}	10	Cr(acac) ₃	131	45
BaTi _{0.802} Cr _{0.198} O _{3-δ}	15	Cr(acac) ₃	132	22

The diffractograms of Zr-based perovskite samples are shown in figure 3.5a and b. The very broad peaks can be assigned to BaZrO₃ (JCPDS No. 6-399). In this case, the crystallites are calculated to be smaller than 2 nm. Although the reaction

temperature was lower than the work published by Niederberger *et al.* (6 days at 200 °C instead of 3 days at 200 and another 3 at 220)³³ a small amount of BaCO₃ (vertical dashed line in Figure 3.5) is present in the pure sample and becomes more relevant upon doping. This is also suggested from the excess of barium compared to zirconium in the as-synthesized powder analyzed by mean of ICP (See Table 3.2).

2.2.4 TEM

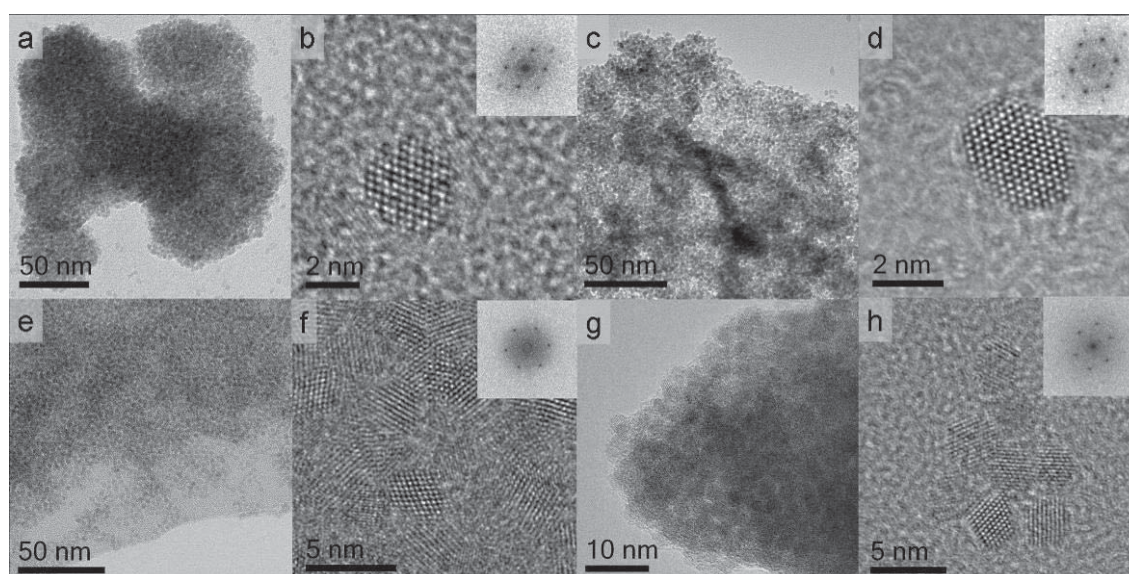


Figure 3.6: The TEM images show agglomerations of particles in low resolution and individual particles at high resolution. Top row: ZrO₂ (a, b) and HfO₂ (c, d). Bottom row: Mn-doped zirconia (e, f) and Mn-doped hafnia (g, h). Insets show the corresponding power spectra (b, h: cubic 110 orientation, d: monoclinic 110 orientation. f: cubic 111 orientation).

In order to evaluate the size, morphology and crystallinity as well as the doping homogeneity of the nanoparticles, the samples were examined by transmission electron microscopy (TEM), electron energy loss spectrometry (EELS) and energy dispersive X-ray spectroscopy (EDX). The observations revealed particles that are homogenous in size and shape. While the zirconia particles mostly appear to be spherical, the hafnia nanoparticles show a nearly ellipsoidal shape, being elongated along the [100] direction²⁹ (Figure 3.6). The sizes extracted from TEM are in good

agreement with the values derived from XRD measurements, pointing out that the nanocrystals are single crystalline in nature (see also refs.^{13,29}). Lattice fringes observed in high resolution (HRTEM) appear regularly and can readily be assigned to the corresponding structures of HfO₂ and ZrO₂, respectively. The zirconia samples and the hafnia doped with more than 4% of Mn precursor reveal a cubic structure, whereas the others (*i.e.* the pure, the low Mn doped and the Cr doped) hafnia nanoparticles are monoclinic. The phase transition observed in the case of the hafnia nanoparticles slightly modify the morphology of the nanoparticles from ellipsoidal to faceted pseudo spherical.

No indications for secondary phases such as Mn_xO_y were found. Clearly, lattice fringe imaging at high resolution provides only local information and is therefore not sufficient to exclude the presence of impurities in the sample. For that reason, EDX spectra have been recorded from particle aggregates of different sizes and also EELS spectra have been recorded in order to analyze the homogeneity of the dopant distribution. In both cases, the HRTEM findings regarding the purity and homogeneity of the samples have been confirmed.

For the synthetic conditions utilized for these samples (see Chapter 2) zirconia and hafnia nanocrystals tend to aggregate in micrometric unordered spheres. The same behavior was showed from doped BaTiO₃ NPs (Figure 3.7a and b). On the other hand, BaZrO₃ particles were organized in random agglomerates (Figure 3.7c and d). This can be explained by the presence of carbonate impurities as well as from the irregular morphology of the crystallites observed at higher resolution.

TEM observation of isolated barium titanate crystals shows well defined lattice fringes proving a certain degree of crystallinity of the particles. The shape is rather irregular although the nanoparticles are mainly pseudospherical.

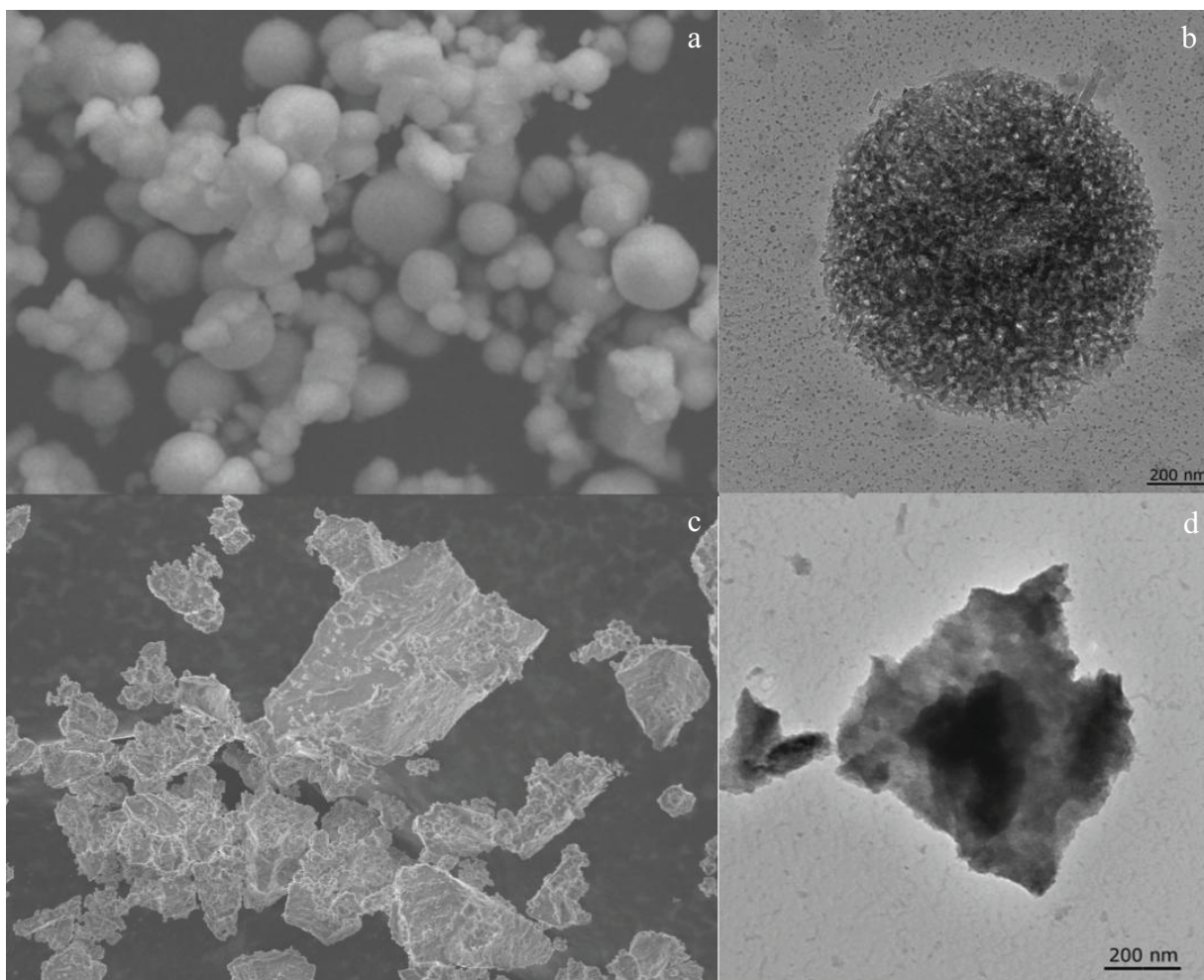


Figure 3.7: SEM and TEM images of Mn-doped BaTiO₃ (a and b, respectively) and BaZrO₃ (c and d, respectively) nanoparticles.

A more careful look of the samples suggests, even in BaTiO₃ case, the occurrence of a second phase, rather difficult to identify. The presence becomes obvious for highly doped samples, in which a larger percentage of the powder consists of the impurity. A thermal treatment at 500 °C on those samples showed, by means of XRD, the appearance of BaCO₃ (data not shown). However, by ICP analysis the amount of titanium was found to be far larger than the one of barium (*cf.* Table 3.2). This suggested the presence of amorphous titanium oxide. The presence of the impurities makes the study of the doping ion environment and its effect on the properties of the

material very difficult to study. Because of that, no further characterization on perovskite samples was carried out.

2.2.5 Diffuse reflectance

In order to investigate the valence state and the local environment of the dopant diffuse reflectance spectroscopy was used.

Both, pure zirconia and hafnia are white powders with optical band gaps around 5-6 eV^{34,35} and they do not present any absorption in the visible range. Therefore, the resulting brown and green colors of the samples are due to the doping with manganese and chromium, respectively.

After doping, an absorption becomes visible at around 400 nm in the spectra of Mn-doped samples, probably due to charge-transfer transitions.^{36,37} The spectra of Mn-doped samples (Figure 3.8a and b) show a broad peak centered around 580 nm for low Mn concentration. With increasing Mn concentration a feature starts to appear at around 470 nm. Above an added doping concentration of around 10%, the low energy features are completely covered by that new band.

The two bands observed in the visible region might be due to Mn in different environments or due to the two manganese oxidation states present in the samples. According to a previous article,¹³ the average oxidation state of Mn ions inside the zirconia is close to II for the less concentrated samples (~1%) and increases to almost III at a 5% manganese concentration. Furthermore, no Mn⁴⁺ ions were found by EPR studies. The peak at higher energy has been attributed to either Mn²⁺ (MnO, 480 nm)³⁸ or Mn³⁺ (Mn₂O₃, 480-485 nm)^{39,40} d-d transitions. However, as this peak arises with increasing Mn concentration, i.e. with a growing Mn³⁺ proportion, it can be tentatively assigned to a ${}^5B_{1g} \rightarrow {}^5B_{2g}$ transition at the Mn³⁺ ions in distorted octahedral symmetry. More difficult is the assignment of the peak at 580 nm, which is present for all the manganese concentrations. However, a similar band was already reported in the case of mixed Mn²⁺/Mn³⁺ doped zirconia³⁶ and sulfated zirconia.³⁷

Chapter 3 – Transitional Metal Doped Oxides

Spectra of Cr-doped zirconia and Cr-doped hafnia are shown in the Figures 3.8c and d, respectively. Both doped matrixes exhibit two broad peaks around 450 and 620 nm despite the different crystal structure of the hosts. These bands are characteristic of intra-3d transitions of Cr^{3+} ions (${}^4\text{F}$) in an octahedral symmetry. In this configuration the bands can be assigned to $A_{2g} \rightarrow T_{1g}$ and $A_{2g} \rightarrow T_{2g}$ transitions, respectively.^{41,42} Nevertheless, the presence of Cr^{4+} should not be excluded as these ${}^3\text{F}$ ions show similar bands in the same region (420-450 and 550-600 nm) but generally with a lower intensity.^{43,44}

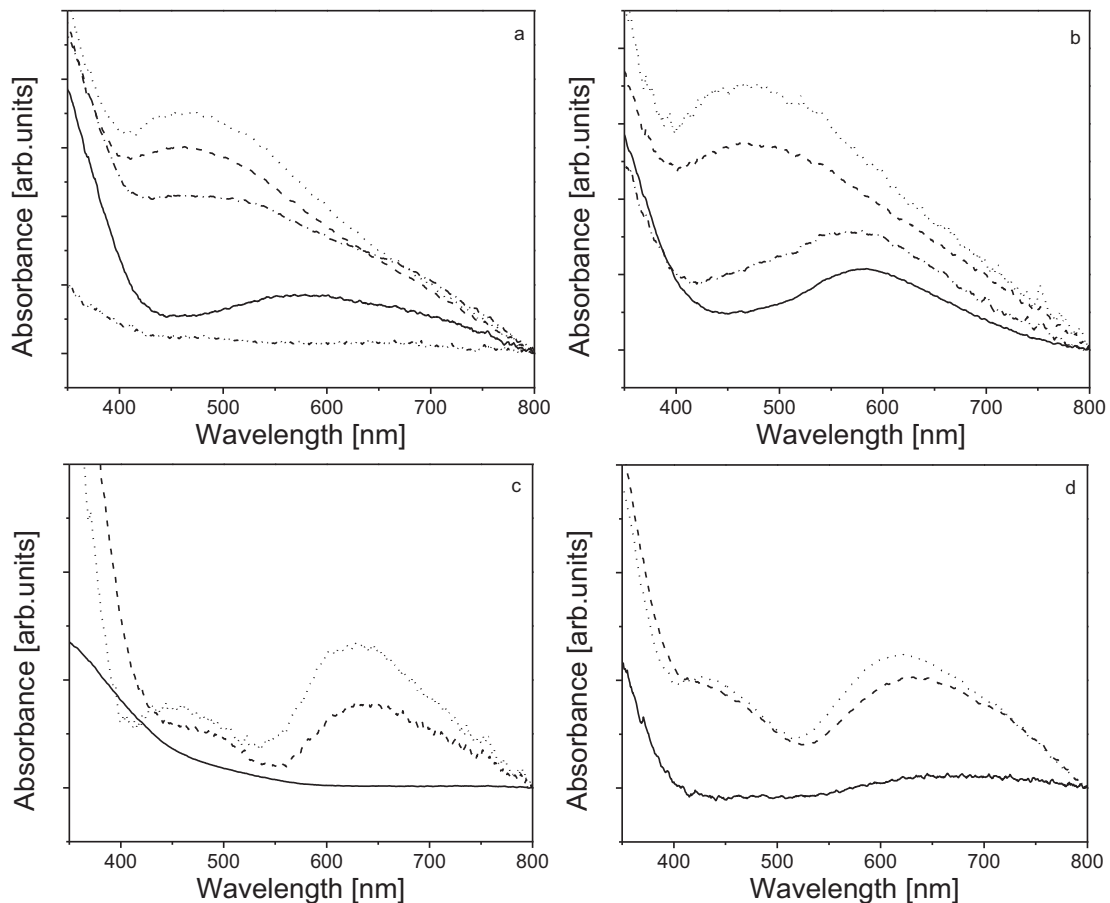


Figure 3.8: UV-Vis spectra of ZrO_2 (a) and HfO_2 (b) doped with 0 (dashed-dotted-dotted line), 1 (solid line), 5 (dashed-dotted line), 10 (dashed line) and 15 (dotted line) % of Mn precursor; UV-Vis spectra of ZrO_2 (c) and HfO_2 (d) doped with 1 (solid line), 10 (dotted line) and 15 (dashed line) % of Cr precursor.

2.2.6 XAS

X-ray absorption spectroscopy was carried out at the beamline BM29 of the European Synchrotron Radiation Facility (ESRF) of Grenoble, France. Synchrotron light provides a powerful source for the investigation of the nature and the local coordination of ions even in complex matrixes, such as doped oxides. The concentration of dopant for some samples was below the resolution limit of the transmission mode, thus only fluorescence regime was utilized. On the other hand, the intensity of this detection technique for its own nature is lower than the transmission mode, making the study of ion environment in doped nanoparticles rather difficult.

X-ray Absorption Near Edge Structure (XANES) spectra of Mn-doped zirconia are depicted in Figure 3.9a. The low concentration sample shows an adsorption edges situated between the MnO and the Mn₂O₃ patterns with energy of 9546.41 eV. For more doped samples the edge shift at higher energy. The almost linear correlation between oxidation state and position of the adsorption edge permits a quantitative determination of the average valence number.⁴⁵ Spectra from MnO, Mn₂O₃ and MnO₂ were also recorded to provide a series of chemically similar compounds to be used as reference. Using this method, the Zr_{0.992}Mn_{0.008}O_{2-δ} sample presents an average oxidation state of 2.6. As observed by Uv-vis analysis, the manganese concentration influences the oxidation state of the dopants. As the concentration increases, the average degree of oxidation increases. XAS experiments show the same behavior indeed, for Zr_{0.955}Mn_{0.045}O_{2-δ} the average oxidation state was 2.7. A similar behavior is envisaged for hafnia, which for highly doped samples reach values of valence above 2.8, as expected from the better doping efficiency of this system compared to the doped zirconia.

Cr-doped zirconia and hafnia samples (Figure 3.9b) are very similar, suggesting that Cr has the same oxidation state and local environment. In both cases the shift of the absorption edge matches perfectly the one of Cr₂O₃ used as reference, confirming an oxidation state of III as suggested from Uv-vis studies.

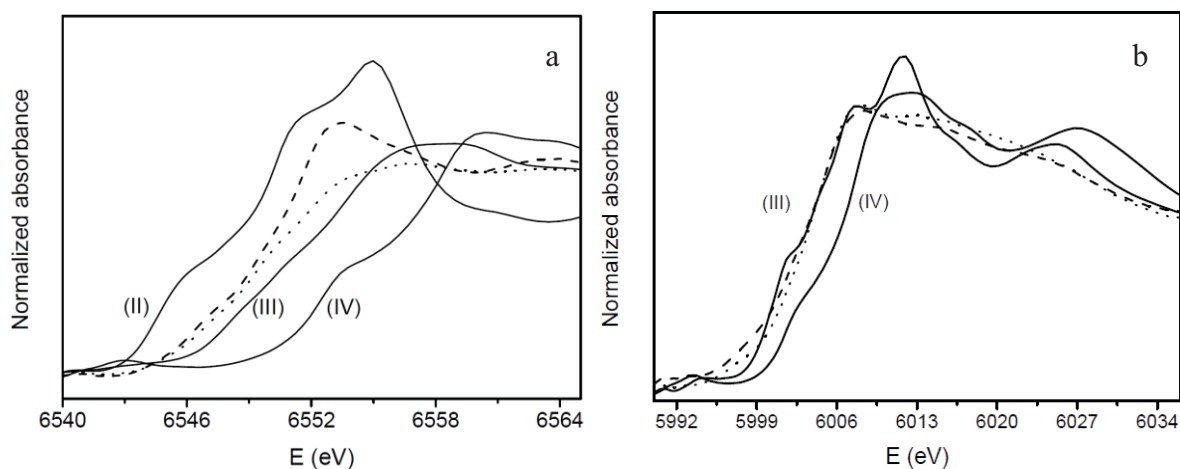


Figure 3.9: XANES spectra of a) 1 (dashed line) and 10% (dotted line) Mn-doped ZrO_2 and b) Cr-doped ZrO_2 (dashed line) and HfO_2 (dotted line) measured at the respective k-edge. The solid lines depict the reference materials.

2.3 Annealing

It was predicted that the oxidation state of the dopant and the concentration of oxygen vacancies would greatly influence the magnetic properties.¹⁶ In our previous work on Mn-doped ZrO_2 , quantitative EPR analyses has revealed that Mn presents two oxidation states, namely II and III, although a IV oxidation state would minimize the concentration of oxygen vacancies. In order to control the dopant oxidation state (or the amount of oxygen vacancies), post-synthesis annealing treatments were carried out under controlled atmosphere (*i.e.* Air and O_2). The thermal stability of the nanoparticles, with respect to the grain size and crystallographic phase, was investigated on Mn doped ZrO_2 samples. XRD patterns were recorded as a function of temperature from RT until 1100 °C under air (Figure 3.10). A narrowing of the peaks due to the increasing crystal size was observed above 600 °C. Above 700 °C, a phase transformation takes place leading to the tetragonal structure. Above 800 °C, a second phase transformation leads to the monoclinic structure and to an increase of the average crystallite size.

Table 3.3. Crystal structure and size dependence on the annealing treatment on Mn-doped zirconia samples.

Sample	Temperature [°C]	Atmosphere	Phase	Size [nm]
Zr _{0.970} Mn _{0.030} O _{2-δ}	RT	Air	cubic	3.4
Zr _{0.970} Mn _{0.030} O _{2-δ}	100	Air	cubic	3.5
Zr _{0.970} Mn _{0.030} O _{2-δ}	200	Air	cubic	3.5
Zr _{0.970} Mn _{0.030} O _{2-δ}	300	Air	cubic	4
Zr _{0.970} Mn _{0.030} O _{2-δ}	400	Air	cubic	3.6
Zr _{0.970} Mn _{0.030} O _{2-δ}	500	Air	cubic	4.2
Zr _{0.970} Mn _{0.030} O _{2-δ}	600	Air	cubic	4.2
Zr _{0.970} Mn _{0.030} O _{2-δ}	700	Air	Tetragonal	6.8
Zr _{0.970} Mn _{0.030} O _{2-δ}	800	Air	tetragonal/monoc	12.7
Zr _{0.970} Mn _{0.030} O _{2-δ}	900	Air	tetragonal/monoc	17.8
Zr _{0.970} Mn _{0.030} O _{2-δ}	1000	Air	tetragonal/monoc	19.9 (35.2 mono)
Zr _{0.970} Mn _{0.030} O _{2-δ}	1100	Air	Monoclinic	(35.2 mono)
Zr _{0.920} Mn _{0.080} O _{2-δ}	RT	Air	Cubic	3.4
Zr _{0.920} Mn _{0.080} O _{2-δ}	600	O ₂	Cubic	6.8
Zr _{0.920} Mn _{0.080} O _{2-δ}	700	O ₂	Tetragonal	12.5
Zr _{0.920} Mn _{0.080} O _{2-δ}	800	O ₂	tetragonal/monoc	17.2

Based on these observations, another annealing was performed under pure oxygen in order to promote higher oxidation states of the dopant and only up to 800 °C in order to avoid phase transformations. Selected samples were annealed in pure oxygen for 30 seconds at 600, 650, 700 and 800 °C in a Rapid Thermal Annealing oven (Figure 3.11). However, under these experimental conditions, the stability of the cubic phase of zirconia decreases. The structure and size variation (estimated using the Scherrer formula) as a function of the annealing temperature are reported in Table 3.3. For annealing temperatures up to 700 °C, no additional peaks due to segregation of the dopant are visible. The pattern of the sample calcined at 800 °C (Figure 3.11d) shows the coexistence of the cubic and monoclinic phases. It is therefore more delicate, from this pattern, to exclude the presence of some additional diffraction peaks due to manganese oxide impurities as they can be hidden by the patterns of the matrixes. Annealing experiments performed on doped hafnia showed similar trends (not shown).

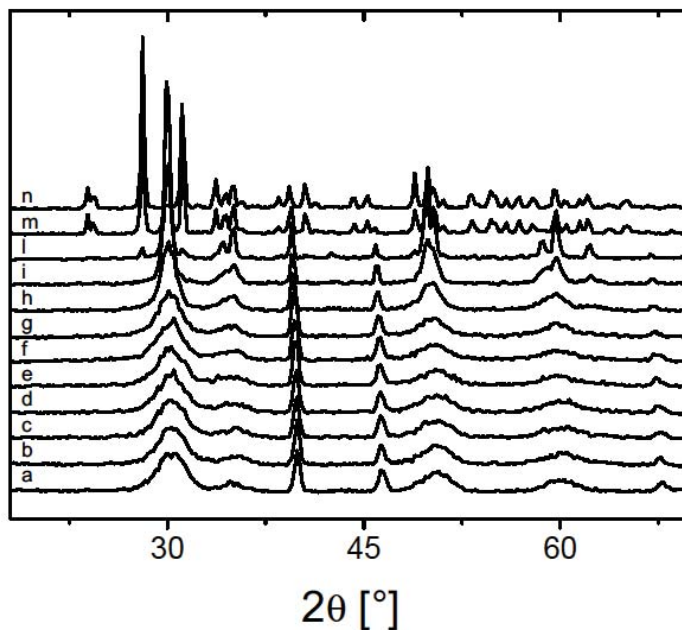


Figure 3.10: XRD patterns of $Zr_{0.970}Mn_{0.030}O_{2.5}$ as synthesized (a) and after annealing under air at the temperature of 100 (b), 200 (c), 300 (d), 400 (e), 500 (f), 600 (g), 700 (h), 800 (i), 900 (l), 1000 (m), 1100 °C (n).

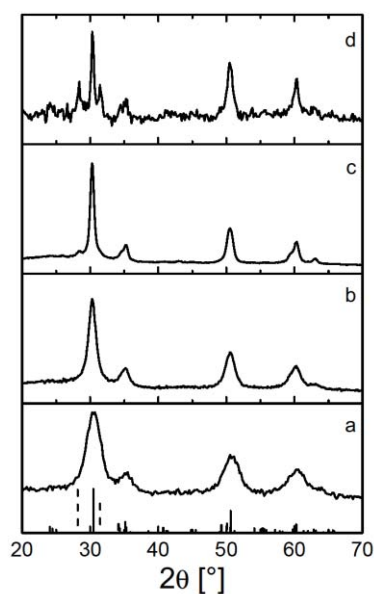


Figure 3.11: XRD patterns of $Zr_{0.920}Mn_{0.080}O_{2.5}$ as synthesized (a) and after annealed under oxygen at the temperature of 600 (b), 700 (c) and 800 (d) °C; expected reflection of cubic (solid line) and monoclinic phase (dashed line).

2.4 Magnetic properties

2.4.1 EPR

Electron paramagnetic resonance is a suitable technique to study the doping of paramagnetic transition metal ions in an oxide matrix. The measurements were performed at 300 K and 100 K. Except for an increase of the signal amplitude at low temperature, no change was observed in the spectra. The spectrum of dilute Mn-ZrO₂ samples depicted in Figure 3.12a resulted very similar to those already shown in a previous article.¹³ The signal centered at $g = 2.020$ was assigned to magnetic interactions of the Mn ions, resulting on a broad band, superimposed to a sextuplet due to isolated spins. Considering the g value and the peak to peak distance of the hyperfine splitting, the signals were attributed to Mn²⁺ ions only.¹³

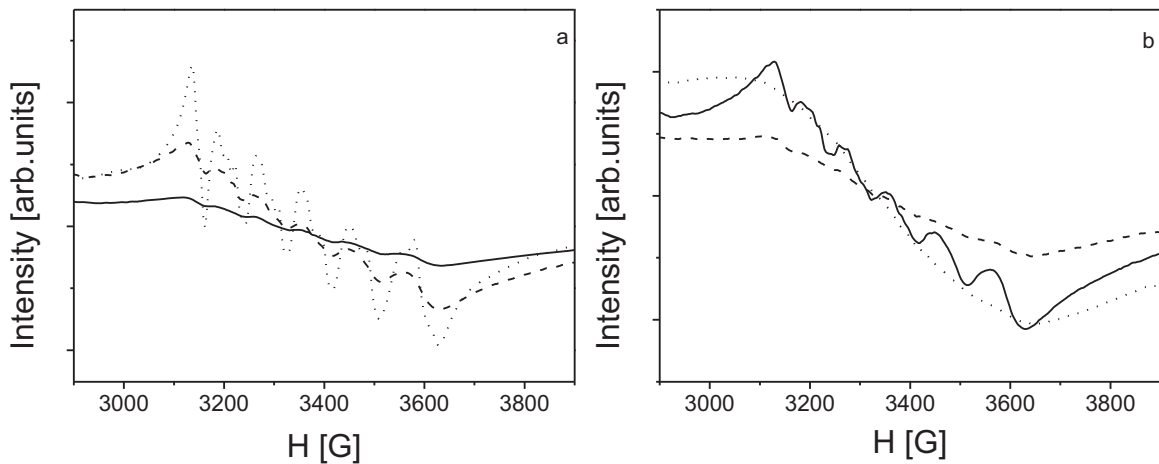


Figure 3.12: a) EPR spectra of Zr_{0.992}Mn_{0.008}O_{2.5} (dotted line), Zr_{0.955}Mn_{0.045}O_{2.5} (dashed line), Zr_{0.920}Mn_{0.080}O_{2.5} (solid line) samples synthesized using Mn(ac)₂ as precursor; b) EPR spectra of Mn-doped zirconia synthesized adding 10% of different precursors: Mn(ac)₂ (solid line), Mn(acac)₃ (dotted line) and Mn(acac)₂ (dashed line).

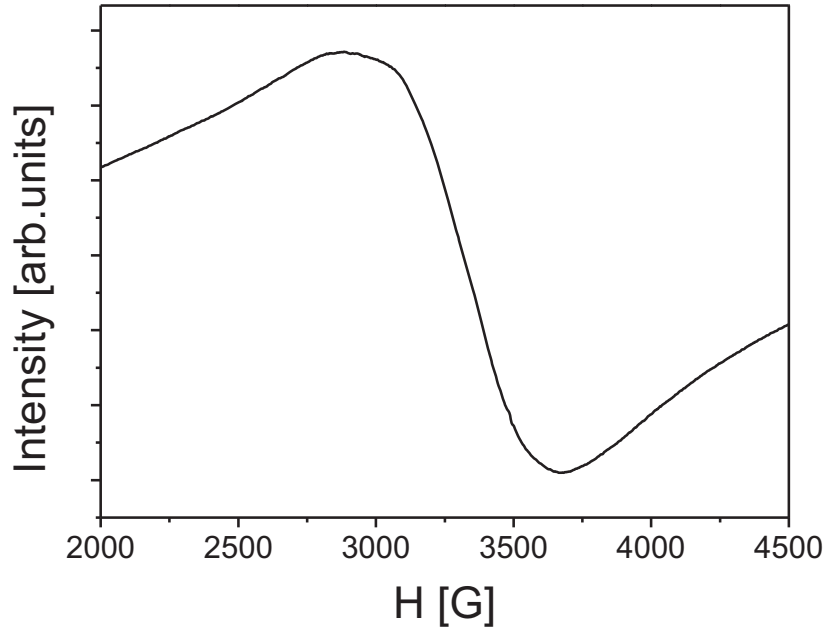


Figure 3.13: EPR spectra of $\text{Hf}_{0.85}\text{Mn}_{0.15}\text{O}_{2-\delta}$ sample synthesized using $\text{Mn}(\text{ac})_2$ as precursor.

In more concentrated samples, the hyperfine splitting (HS) becomes less discernible as dipolar coupling between the Mn spins broaden the sextuplet (Figure 3.12a). Even though the manganese concentration increases from 1 to 8 %, the intensity of the measured signals are comparable and no additional peaks coming from higher oxidation states were detected. As already demonstrated, upon increasing Mn concentration, the $[\text{Mn}^{3+}]/[\text{Mn}^{2+}]$ ratio increases.¹³ However, Mn^{3+} cannot be detected as it is silent in the EPR X-band commonly used.

As already noticed in Table 3.1a, the Mn precursor nature influences the doping efficiency. Using $\text{Mn}(\text{ac})_2$, the doping efficiency is very low and, consequently, the sextuplet is still observed even for high loading of Mn precursor (Figure 3.12b, solid line).

The EPR spectra of Mn-doped HfO_2 present a broad peak centered at $g = 2.05$ and no hyperfine splitting is discernible even at very low Mn concentration (Figure 3.13). Similarly to the case of zirconia, the signal is assumed to originate from the presence

of the Mn^{2+} ions. Further, the lack of hyperfine splitting and the absence of additional manganese oxide phases (*cf.* XRD and TEM studies) confirm the strong dipolar interaction between the spins and thus the doping inside the nanocrystals core. The higher doping efficiency for hafnia as compared to the case of zirconia explains the sole presence of a broad signal.

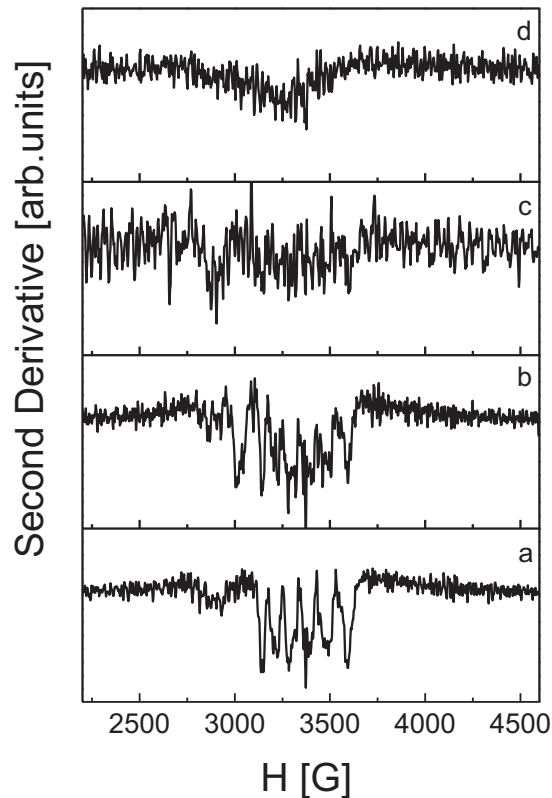


Figure 3.14: Second derivative of EPR spectra of $\text{Zr}_{0.920}\text{Mn}_{0.080}\text{O}_{2.5}$ as synthesized (a) and after annealing at the temperature of 600 (b), 700 (c), 800 (d) °C.

The samples obtained after rapid thermal annealing were also investigated with EPR. The signal was not affected by annealing up to 600 °C. The signal amplitude remains the same and the hyperfine splitting is still detectable (Figure 3.14). In the spectrum of the sample annealed at 700 °C the HS is faintly discernible and the intensity is reduced, probably due to the appearance of manganese ions in a tetragonal environment.⁴⁶ Further increasing of the furnace temperature (800 °C) leads to an

Chapter 3 – Transitional Metal Doped Oxides

additional decrease of the intensity, the complete vanishing of the HS and a shift to lower field value ($g = 2.07$). This shift can be attributed to the distortions caused by the structural phase change observed at this temperature (from cubic to tetragonal and then monoclinic).⁴

Due to the fact that the line width of the EPR signal, when plotted as a function of the temperature, depends on the magnetic interactions taking place in the sample, it can be used for the detection of magnetic impurities. EPR spectra of the $\text{Zr}_{0.920}\text{Mn}_{0.080}\text{O}_{2-\delta}$ sample annealed at 800 °C were therefore recorded between 15 and 120 K.

For an ideal diluted magnetic semiconductor, a hyperbolic decrease of the resonance intensity is expected. In the present case, an inverse correlation between the resonance intensity centered at $g = 2$ and the temperature was observed below 45 K and above 80 K (Figure 3.15). A maximum occurs around 65 K, almost matching the Curie temperature of the ferromagnet Mn_3O_4 , confirming the occurrence of manganese segregation.⁴

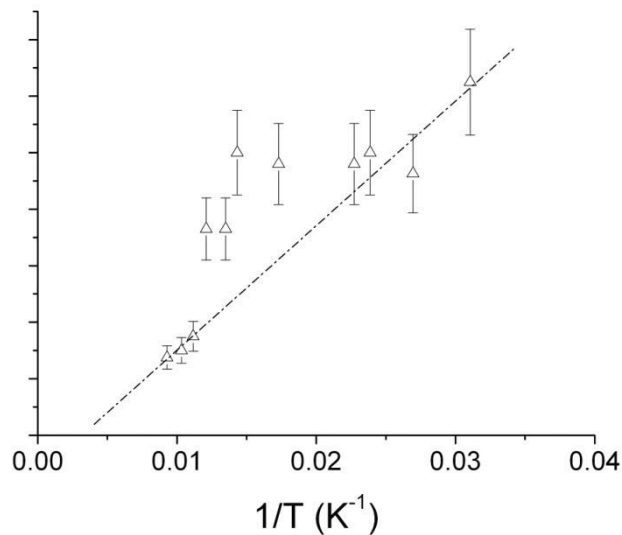


Figure 3.15: Temperature dependence of the resonance intensity of the EPR spectra in $\text{Zr}_{0.920}\text{Mn}_{0.080}\text{O}_{2-\delta}$ annealed under oxygen at 800 °C.

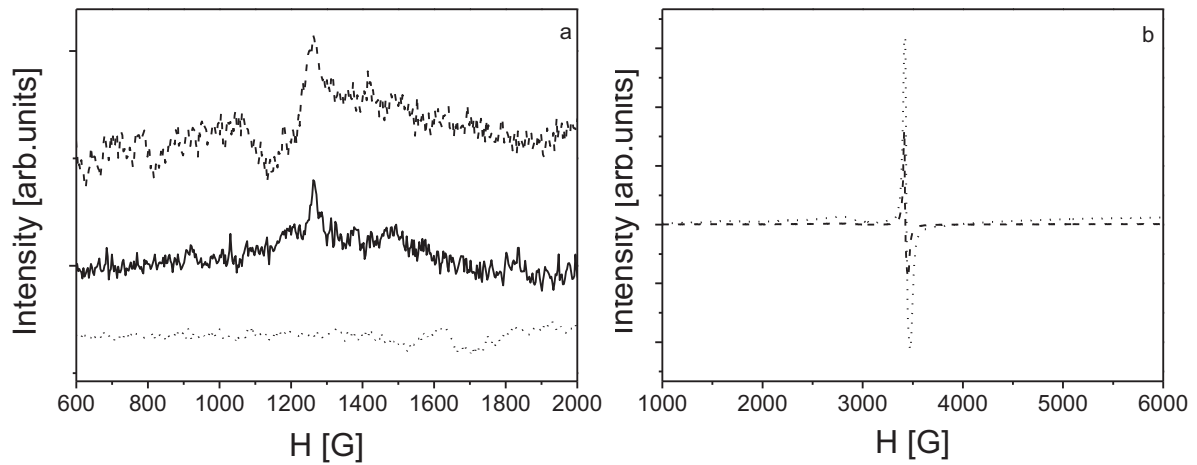


Figure 3.16: a) EPR spectra of $Zr_{0.998}Cr_{0.002}O_{2-\delta}$ (solid line), $Zr_{0.980}Cr_{0.020}O_{2-\delta}$ (dashed line) and $Hf_{0.996}Cr_{0.004}O_{2-\delta}$ (dotted line); b) EPR spectra of Cr-doped zirconia (dashed line) and Cr-doped hafnia (dotted line) samples after under air annealing at 500 °C.

In the case of chromium ions, three signals, referred to as δ , β and γ , are expected depending on the chromium oxidation state and its environment.⁴⁷ For Cr-doped zirconia only a weak band at $g = 5.33$ is visible (Figure 3.16a). This band is a δ type and can be attributed to Cr^{3+} homogeneously dispersed in the zirconia matrix. On the other hand, the EPR spectra of Cr-doped hafnia present no band in this region. Since all chemical characterizations clearly prove an effective doping and the average oxidation state was proved to be III by means of XAS, the ambiguity could be explained by the coexistence of Cr^{4+} in an octahedral environment and Cr^{2+} in tetragonal symmetry. Indeed, the resonance of Cr^{4+} could hardly be observed in the literature as its intensity is very low⁴⁸ and bivalent chromium signal in tetragonal was claimed to be hampered in X-band spectrometers.^{49,50} The lack of the β signal confirms once again the absence of Cr_2O_3 clusters.⁵¹

After calcinations, both samples show a sharp and intense peak at $g = 1.97$ (Figure 3.16b) which is attributed to a γ peak and hence, to Cr^{5+} ions at the surface of the particles or, less likely, to surface mixed valence trimers of the type “ $Cr^{6+}-O-Cr^{3+}-O-Cr^{6+}$ ”, containing both chromium(III) and chromium(VI) in which the average oxidation state of the chromium is V.^{47,51,52} Both are indications for an oxidation in the surface

region of the particles. In the case of zirconia, the δ signal is still detectable, suggesting that the oxidation is not complete.

2.4.2 Susceptibility Studies

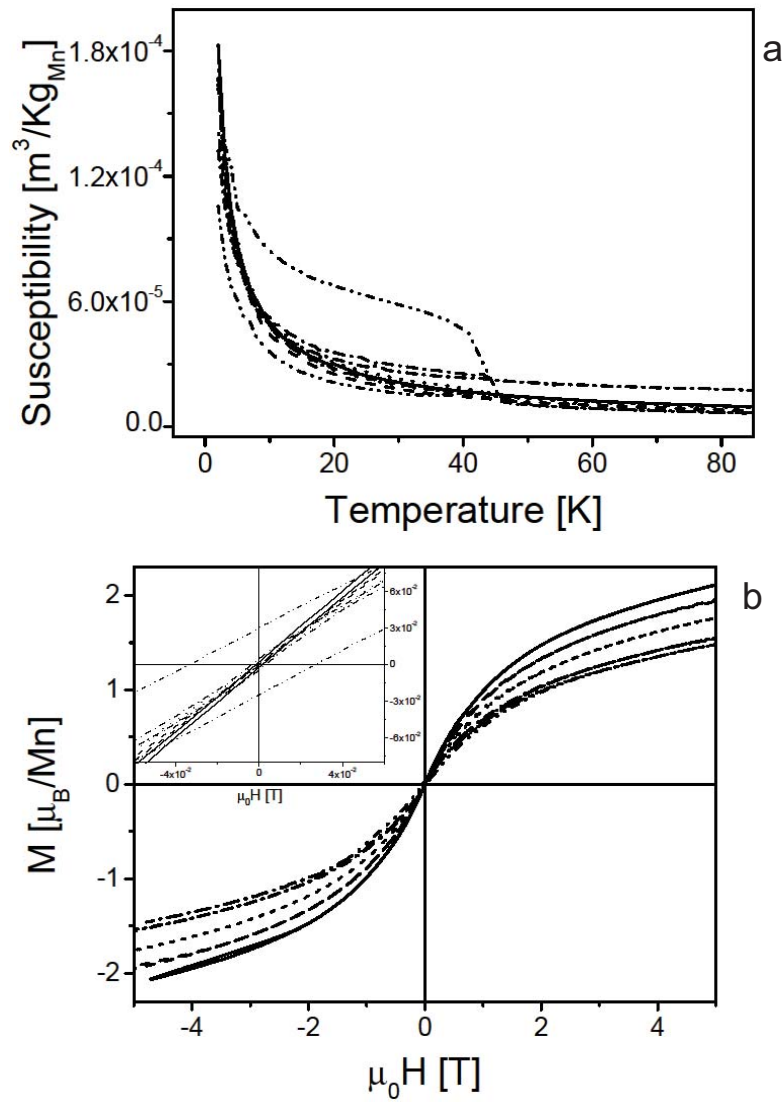


Figure 3.17: ZFC/FC curves measured under a field of $\mu_0 H = 500$ Oe (a) and hysteresis loop at $T = 2$ K (b) for $Zr_{0.920}Mn_{0.080}O_{2-\delta}$ as synthesized (solid line) and after annealing under oxygen at the temperature of 600 (dashed line), 650 (dotted line), 700 (dashed-dotted-dotted line) and 800 (dashed-dotted line) °C.

The magnetic measurements were carried out on all hafnia and zirconia samples. The susceptibility curve of diluted Mn doped ZrO_2 synthesized via the benzyl alcohol route displays a hyperbolic trend typical of a paramagnetic behavior.¹³ Here, we shall focus on the highest dopant concentration achieved on this system, namely $\text{Zr}_{0.920}\text{Mn}_{0.080}\text{O}_{2-\delta}$. Zero Field Cooled/Field Cooled (ZFC/FC) measurements were carried out on pristine samples and samples annealed between 600 and 800 °C in the RTA furnace. Unlike the as-synthesized $\text{Zr}_{0.920}\text{Mn}_{0.080}\text{O}_{2-\delta}$, annealed samples show a deviation from the Curie law at around 42 K (Figure 3.17a). The discrepancy between ZFC and FC curves becomes larger with increasing the annealing temperature. This ferromagnetic contribution is attributed to manganese oxide clusters, with a composition close to Mn_3O_4 . The Curie temperature shows a slight discrepancy from the bulk value of Mn_3O_4 but matches perfectly the Curie temperature found in diluted systems like Mn doped ZnO ¹⁵ or the blocking temperature in Mn_3O_4 nanoparticles.⁵³ This fact can also explain the huge increase of the loop width in ZFC/FC experiments (Figure 3.17a) from samples treated at 700 and 800 °C, indeed the phase modification of zirconia facilitates the segregation.

The decrease of the magnetic moment with annealing temperature is consistent with the oxidation of some Mn^{2+} ions as deduced from the EPR analysis. Even after annealing, the magnetization does not reach the saturation under a field of $\mu_0H = 5$ T. The Langevin fit of the M-H curve at $T = 2$ K gives estimated values of 2.70, 2.47, 2.20, 1.95 and 1.83 μ_B/Mn for $\text{Zr}_{0.920}\text{Mn}_{0.080}\text{O}_{2-\delta}$ samples before and after annealing at 600, 650, 700 and 800 °C, respectively. In the inset of the Figure 3.17b a magnification of the loops is shown. The ferromagnetic interactions are clearly visible for the highest temperature treated sample, where they give rise to a coercive field of 29.9 mT.

The study of the magnetic properties of Mn doped ZrO_2 shows therefore that the solubility limit of manganese in ZrO_2 has been reached and that, even after a chemical treatment aimed to fill the oxygen vacancies, no intrinsic ferromagnetism could be found for these samples. This result confirms another experimental study recently published on Mn and Fe doped ZrO_2 .¹⁸

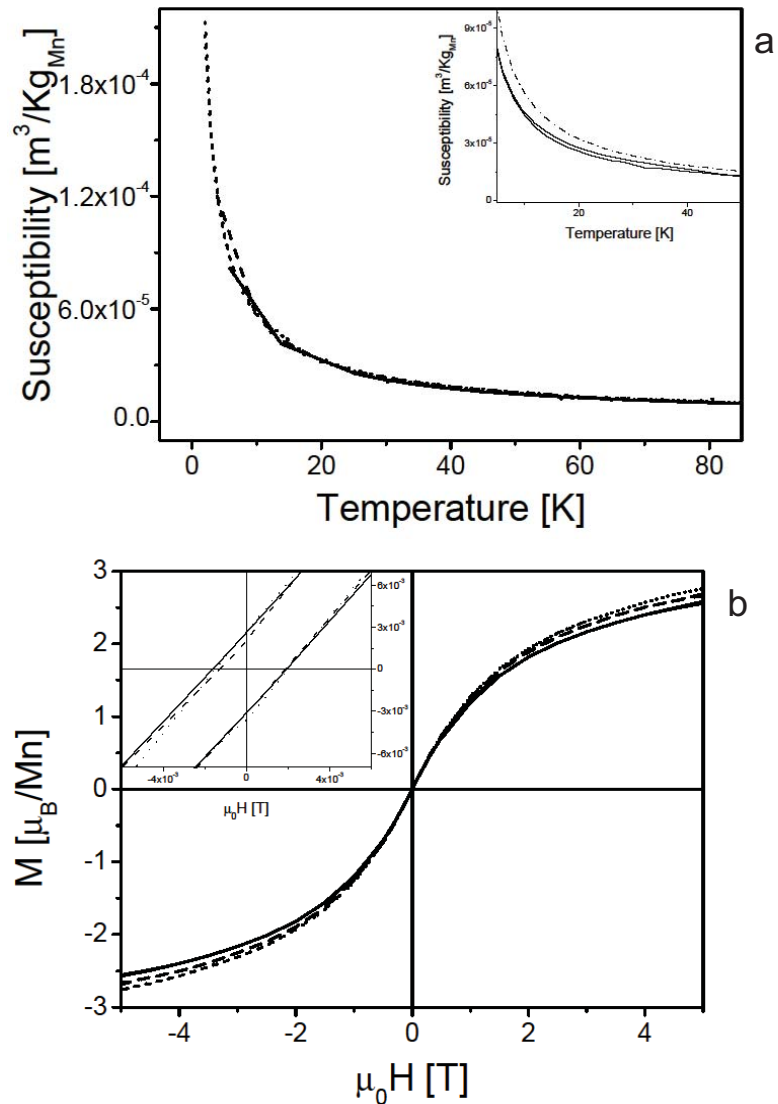


Figure 3.18: ZFC/FC curves measured in a field of 500 Oe (a) and hysteresis loop at $T = 2$ K (b) for Mn-doped hafnia synthesized with 15% of $\text{Mn}(\text{ac})_2$ (solid line), $\text{Mn}(\text{acac})_2$ (dashed line) and $\text{Mn}(\text{acac})_3$ (dotted line). Inset in Fig. a: ZFC/FC curves of pristine sample (dotted-dashed line) and annealed at 650 °C (solid line).

The susceptibility of manganese doped HfO_2 samples follow a Curie law and the magnetic moment per Mn atom reaches a value comparable to the doped zirconia samples. The clustering of Mn oxide takes place only after calcinations at 650 °C for

highly doped samples (about 15%); a small transition to ferromagnetism at $T = 42$ K is present (Figure 3.18a inset) as already observed on Mn doped ZrO_2 . The doping of the hafnia samples from different manganese precursors almost does not influence the magnetization (Figure 3.18b).

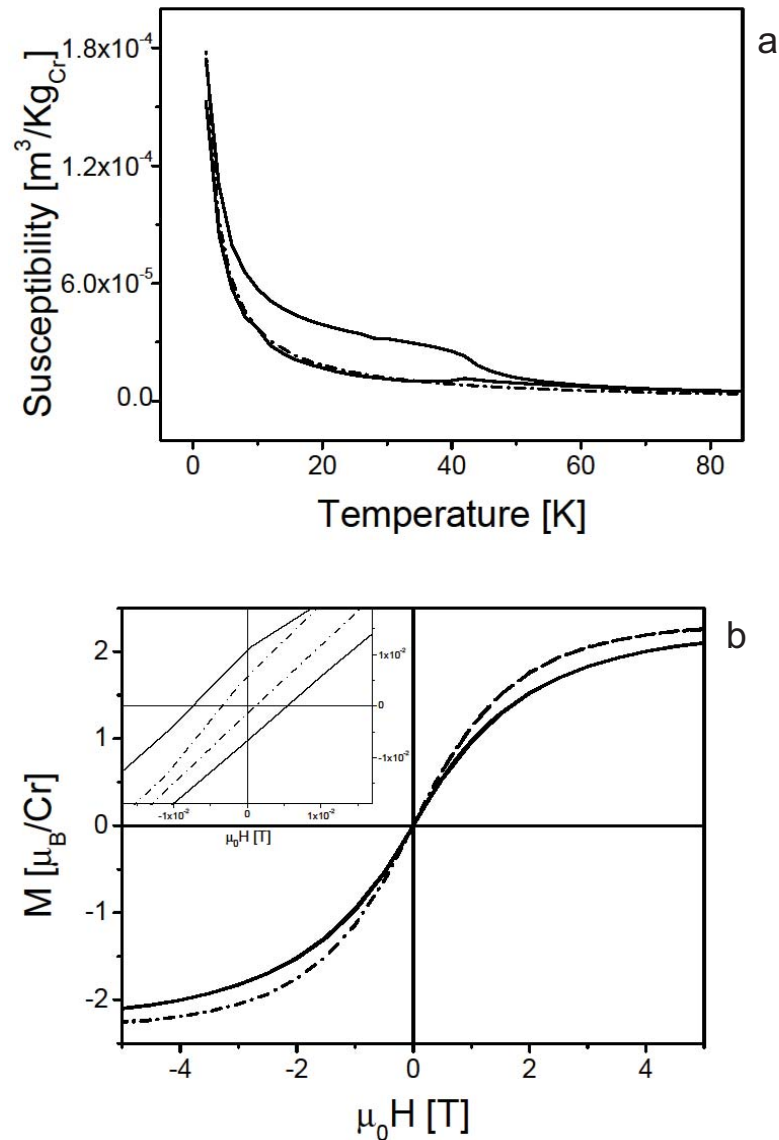


Figure 3.19: Magnetic measurements $Zr_{0.980}Cr_{0.020}O_{2-\delta}$, pristine sample (dotted-dashed line) and sample annealed at 650°C (solid line): ZFC/FC curves measured in a field of 500 Oe (a) and hysteresis loop at $T = 2$ K (b).

Chapter 3 – Transitional Metal Doped Oxides

The chromium-doped samples present a classical Curie law behavior before calcination (Figure 3.19). The substitution of Zr by Cr without formation of an oxygen vacancy would result in a Cr^{4+} state ($2 \mu_{\text{B}}/\text{Cr}$). The hysteresis loops reveal a large magnetic moment of $2.32 \mu_{\text{B}}/\text{Cr}$ consistent with a lower oxidation state of Cr. A magnetization value of $2.6 \mu_{\text{B}}/\text{Cr}$ was found in Cr^{3+} -doped anatase TiO_2 .⁵⁴ Therefore, the average oxidation state of chromium in our samples is confirmed to be around III. Interestingly, this oxidation state, at higher doping concentration (*i.e.* 25%), is predicted to be a ferromagnetic phase according to the calculations made by Ostanin *et al.*¹⁶

The only noticeable feature has been recorded on $\text{Zr}_{0.980}\text{Cr}_{0.020}\text{O}_{2-\delta}$ (Figure 3.19). Upon annealing at 650°C under pure oxygen, the ZFC curve displays a maximum at 43 K and the FC curve features a transition to ferromagnetism below the very same temperature. Contrary to Mn doped samples, the transition could hardly be ascribed to a known impurity since Cr_2O_3 is an antiferromagnet with a $T_{\text{Néel}} = 307 \text{ K}$ ⁵⁵ and chromium dioxide (CrO_2) is the only ferromagnetic (FM) compound with a Curie temperature of $\sim 390 \text{ K}$, which in addition, shows ‘half-metallic’ behavior with a magnetic moment of $2 \mu_{\text{B}}$ per Cr atom.⁵⁶ Therefore, the magnetic behavior observed for this compound could indeed be due to an intrinsic ferromagnetic behavior of the doped oxide.

This hypothesis could be confirmed by the study of Cr doped HfO_2 . Although the doping efficiency is much higher in that case (up to 7%), all samples have displayed paramagnetic behavior (not shown) with a magnetic moment of the annealed sample of $1.8 \mu_{\text{B}}$ per Cr atom. Along with EPR measurements, this value confirms the higher oxidation state of Cr (between IV and V). If one recalls the calculations by Ostanin *et al.*, the paramagnetic state could certainly be explained by the instability of the FM phase for the Cr^{4+} to Cr^{5+} oxidation state.¹⁶

Table 3.4. Magnetic behavior of pristine and annealed samples. Ms: magnetization at saturation, T_c: Curie temperature and T_θ Curie-Weiss temperature.

Samples	Annealing	Precursor	Magnetic Coupling	M _s (μ _B /MT)	T _c (K)	T _θ (K)
Zr _{0.920} Mn _{0.080} O _{2-δ}	Pristine	Mn(ac) ₂	Antiferromagnetic	2.70		-76.5
Zr _{0.920} Mn _{0.080} O _{2-δ}	600 °C	Mn(ac) ₂	Ferromagnetic	2.47	42	
Zr _{0.920} Mn _{0.080} O _{2-δ}	650 °C	Mn(ac) ₂	Ferromagnetic	2.20	42	
Zr _{0.920} Mn _{0.080} O _{2-δ}	700 °C	Mn(ac) ₂	Ferromagnetic	1.95	42	
Zr _{0.920} Mn _{0.080} O _{2-δ}	800 °C	Mn(ac) ₂	Ferromagnetic	1.83	42	
Hf _{0.830} Mn _{0.170} O _{2-δ}	Pristine	Mn(acac) ₃	Antiferromagnetic	3.51		-11.5
Hf _{0.840} Mn _{0.160} O _{2-δ}	Pristine	Mn(acac) ₂	Antiferromagnetic	3.42		-11.2
Hf _{0.850} Mn _{0.150} O _{2-δ}	Pristine	Mn(ac) ₂	Antiferromagnetic	3.28		-11.9
Hf _{0.840} Mn _{0.160} O _{2-δ}	650 °C	Mn(acac) ₂	Ferromagnetic	2.30	42	
Zr _{0.980} Cr _{0.020} O _{2-δ}	Pristine	Cr(acac) ₃	Ferromagnetic	2.32		10.8
Zr _{0.980} Cr _{0.020} O _{2-δ}	650 °C	Cr(acac) ₃	Ferromagnetic	2.08	43	
Hf _{0.930} Cr _{0.070} O _{2-δ}	Pristine	Cr(acac) ₃	Antiferromagnetic	2.66		-8.03
Hf _{0.930} Cr _{0.070} O _{2-δ}	650 °C	Cr(acac) ₃	Antiferromagnetic	1.80		-0.23

3 Conclusions

The chapter reported high doping efficiency in the synthesis of transition metal doped zirconium and hafnium binary oxides and BaTiO₃ and BaZrO₃ perovskites by tuning the reactivity of the molecular precursors under non-aqueous sol-gel conditions in benzyl alcohol. The largest effective doping concentration was obtained for HfO₂ from Mn(acac)₃ (17% Mn). Unfortunately, the perovskites showed the occurrence of inorganic impurities which made the as-synthesized material not suitable to investigate the magnetic properties related with the doping of transitional metal. A combination of several characterization techniques was used in order to correlate the synthesis conditions to the doping efficiency and behavior, and to the magnetic properties of the as synthesized nanocrystals. Post-synthetic annealing treatments under controlled atmospheres were performed in order to control the oxidation state of the transition metal ions and the amount of oxygen vacancies. It turned out that this is a rather delicate step as it can induce segregation and clustering at relatively low temperature (*i.e.* above 600-700 °C), as well as phase transformations. We conclude

Chapter 3 – Transitional Metal Doped Oxides

from our study that the annealing has to be performed below 650°C to preserve the nanocrystals size and the crystallographic structure.

Magnetic measurements reveal three different behaviors (*cf.* Table 3.4): i) a paramagnetic state for ZrO₂ and HfO₂ doped samples for all studied transition metal contents; ii) clustering of ferromagnetic Mn₃O₄ in the case of Mn-doped samples after calcination; iii) a FM phase below 43 K for Cr-doped ZrO₂, which has been attributed to the intrinsic DMS behavior.

4 Bibliography

- (1) Park, J.; Joo, J.; Kwon, Soon G.; Jang, Y.; Hyeon, T. *Angewandte Chemie International Edition* **2007**, *46*, 4630.
- (2) Pinna, N.; Niederberger, M. *Angewandte Chemie International Edition* **2008**, *47*, 5292.
- (3) Liu, Z.; Deng, H.; Yang, P.; Chu, J. *Materials Letters* **2009**, *63*, 2622.
- (4) Djerdj, I.; Arcon, D.; Jaglicic, Z.; Niederberger, M. *J. Phys. Chem. C* **2007**, *111*, 3614.
- (5) Cushing, B. L.; Kolesnichenko, V. L.; O'Connor, C. J. *Chemical Reviews* **2004**, *104*, 3893.
- (6) Livage, J.; Henry, M.; Sanchez, C. *Progress in Solid State Chemistry* **1988**, *18*, 259.
- (7) Sanchez, C.; Livage, J.; Henry, M.; Babonneau, F. *Journal of Non-Crystalline Solids* **1988**, *100*, 65.
- (8) Vioux, A. *Chemistry of Materials* **1997**, *9*, 2292.
- (9) Niederberger, M.; Garnweitner, G. *Chemistry - A European Journal* **2006**, *12*, 7282.
- (10) Seshadri, R. *Current Opinion in Solid State and Materials Science* **2005**, *9*, 1.
- (11) Clavel, G.; Pinna, N.; Zitoun, D. *physica status solidi (a)* **2007**, *204*, 118.
- (12) Clavel, G.; Willinger, M. G.; Zitoun, D.; Pinna, N. *Advanced Functional Materials* **2007**, *17*, 3159.
- (13) Clavel, G.; Willinger, M.-G.; Zitoun, D.; Pinna, N. *European Journal of Inorganic Chemistry* **2008**, *2008*, 863.
- (14) Yuhas, B. D.; Zitoun, D. O.; Pauzauskie, P. J.; He, R.; Yang, P. *Angewandte Chemie International Edition* **2006**, *45*, 420.
- (15) Djerdj, I.; Garnweitner, G.; Arcon, D.; Pregelj, M.; Jaglicic, Z.; Niederberger, M. *Journal of Materials Chemistry* **2008**, *18*, 5208.
- (16) Ostanin, S.; Ernst, A.; Sandratskii, L. M.; Bruno, P.; Dane, M.; Hughes, I. D.; Staunton, J. B.; Hergert, W.; Mertig, I.; Kudrnovsky, J. *Physical Review Letters* **2007**, *98*, 016101.
- (17) Maznichenko, I. V.; Ostanin, S.; Ernst, A.; Mertig, I. *Journal of Magnetism and Magnetic Materials* **2009**, *321*, 913.
- (18) Yu, J.; Duan, L. B.; Wang, Y. C.; Rao, G. H. *Physica B: Condensed Matter* **2008**, *403*, 4264.
- (19) Valigi, M.; Gazzoli, D.; Dragone, R.; Marucci, A.; Mattei, G. *Journal of Materials Chemistry* **1996**, *6*, 403.
- (20) Rao, M. S. R.; Kundaliya, D. C.; Ogale, S. B.; Fu, L. F.; Welz, S. J.; Browning, N. D.; Zaitsev, V.; Varughese, B.; Cardoso, C. A.; Curtin, A.; Dhar, S.; Shinde, S. R.; Venkatesan, T.; Lofland, S. E.; Schwarz, S. A. *Applied Physics Letters* **2006**, *88*, 142505.
- (21) Hong, N. H.; Poirot, N.; Sakai, J. *Applied Physics Letters* **2006**, *89*, 042503.

Chapter 3 – Transitional Metal Doped Oxides

- (22) Chang, Y. H.; Soo, Y. L.; Lee, W. C.; Huang, M. L.; Lee, Y. J.; Weng, S. C.; Sun, W. H.; Hong, M.; Kwo, J.; Lee, S. F.; Ablett, J. M.; Kao, C. C. *Applied Physics Letters* **2007**, *91*, 082504.
- (23) Kleemann, W.; Bedanta, S.; Borisov, P.; Shvartsman, V. V.; Miga, S.; Dec, J.; Tkach, A.; Vilarinho, P. M. *The European Physical Journal B - Condensed Matter and Complex Systems* **2009**, *71*, 407.
- (24) Shvartsman, V. V.; Bedanta, S.; Borisov, P.; Kleemann, W.; Tkach, A.; Vilarinho, P. M. *Physical Review Letters* **2008**, *101*, 165704.
- (25) Wei, X. K.; Zhang, Q. H.; Li, F. Y.; Jin, C. Q.; Yu, R. C. *Journal of Alloys and Compounds* **2010**, *508*, 486.
- (26) Lin, F.; Shi, W. *Journal of Alloys and Compounds* **2009**, *475*, 64.
- (27) Lin, F.; Jiang, D.; Ma, X.; Shi, W. *Journal of Magnetism and Magnetic Materials* **2008**, *320*, 691.
- (28) Garnweitner, G.; Goldenberg, L. M.; Sakhno, O. V.; Antonietti, M.; Niederberger, M.; Stumpe, J. *Small* **2007**, *3*, 1626.
- (29) Pinna, N.; Garnweitner, G.; Antonietti, M.; Niederberger, M. *Advanced Materials* **2004**, *16*, 2196.
- (30) Niederberger, M.; Garnweitner, G.; Pinna, N.; Antonietti, M. *J. Am. Chem. Soc.* **2004**, *126*, 9120.
- (31) Garnweitner, G.; Niederberger, M. *Journal of the American Ceramic Society* **2006**, *89*, 1801.
- (32) Karmaoui, M.; Willinger, M. G.; Mafra, L.; Hertrich, T.; Pinna, N. *Nanoscale* **2009**, *1*, 360.
- (33) Niederberger, M.; Pinna, N.; Polleux, J.; Antonietti, M. *Angewandte Chemie International Edition* **2004**, *43*, 2270.
- (34) French, R. H.; Glass, S. J.; Ohuchi, F. S.; Xu, Y. N.; Ching, W. Y. *Journal Name: Physical Review, B: Condensed Matter; (United States); Journal Volume: 49:8* **1994**, Medium: X; Size: Pages: 5133.
- (35) Bendoraitis, J. G.; Salomon, R. E. *The Journal of Physical Chemistry* **1965**, *69*, 3666.
- (36) Sasaki, K.; Maier, J. *Solid State Ionics* **2000**, *134*, 303.
- (37) Klose, B. S.; Jentoft, F. C.; Joshi, P.; Trunschke, A.; Schlögl, R.; Subbotina, I. R.; Kazansky, V. B. *Catalysis Today* **2006**, *116*, 121.
- (38) Pratt, G. W.; Coelho, R. *Physical Review* **1959**, *116*, 281.
- (39) Lopez, E. F.; Escribano, V. S.; Panizza, M.; Carnasciali, M. M.; Busca, G. *Journal of Materials Chemistry* **2001**, *11*, 1891.
- (40) Milella, F.; Gallardo-Amores, J. M.; Baldi, M.; Busca, G. *Journal of Materials Chemistry* **1998**, *8*, 2525.
- (41) Köhler, K.; Engweiler, J.; Baiker, A. *Journal of Molecular Catalysis A: Chemical* **2000**, *162*, 423.
- (42) Pavlov, R. S.; Marza, V. B.; Carda, J. B. *Journal of Materials Chemistry* **2002**, *12*, 2825.
- (43) Rana, S.; Ram, S.; Roy, S. K. *Materials and Manufacturing Processes* **2002**, *17*, 529
- (44) Ram, S. *Journal of Materials Science* **2003**, *38*, 643.

- (45) Wong, J.; Lytle, F. W.; Messmer, R. P.; Maylotte, D. H. *Physical Review B* **1984**, *30*, 5596.
- (46) Occhiuzzi, M.; Cordischi, D.; Dragone, R. *Physical Chemistry Chemical Physics* **2003**, *5*, 4938.
- (47) Harrison, P. G.; Lloyd, N. C.; Daniell, W. J. *Phys. Chem. B* **1998**, *102*, 10672.
- (48) Abragam, A.; Bleaney, B. *Electron Paramagnetic Resonance of Transition Ions*; Clarendon Press: Oxford, England, 1970.
- (49) Langhammer, H. T.; Muller, T.; R., B.; H.-P., A. *Journal of Physics: Condensed Matter* **2008**, *20*, 085206.
- (50) Avanesov, A.; Badikov, V.; Shakurov, G. *Physics of the Solid State* **2003**, *45*, 1451.
- (51) Cimino, A.; Cordischi, D.; De Rossi, S.; Ferraris, G.; Gazzoli, D.; Indovina, V.; Occhiuzzi, M.; Valighi, M. *Journal Name: Journal of Catalysis; (USA); Journal Volume: 127:2* **1991**, Medium: X; Size: Pages: 761.
- (52) Liotta, L. F.; Venezia, A. M.; Pantaleo, G.; Deganello, G.; Gruttadauria, M.; Noto, R. *Catalysis Today* **2004**, *91-92*, 231.
- (53) Seo, W. S.; Jo, H. H.; Lee, K.; Kim, B.; Oh, S. J.; Park, J. T. *Angewandte Chemie International Edition* **2004**, *43*, 1115.
- (54) Hong, N. H.; Ruyter, A.; Prellier, W.; Sakai, J. *Applied Physics Letters* **2004**, *85*, 6212.
- (55) Corliss, L. M.; Hastings, J. M.; Nathans, R.; Shirane, G. *Journal of Applied Physics* **1965**, *36*, 1099.
- (56) Korotin, M. A.; Anisimov, V. I.; Khomskii, D. I.; Sawatzky, G. A. *Physical Review Letters* **1998**, *80*, 4305.

CHAPTER 4*
Rare Earth Doped Zirconia

*This chapter has never been either submitted nor published at the time of the defense.

Table of contents

1	Introduction	71
2	Result and Discussion	72
2.1	Structural and Morphological Characterization	72
2.2	Electrochemical properties of 14.8% Y-doped ZrO ₂	78
2.2.1	Sintering of the ceramics	78
2.2.2	Electrical conductivity	80
3	Conclusion	86
4	Bibliography	87

1 Introduction

Y-doped zirconia is a very well known material exploited for ceramic and electroceramic applications.¹ The solubility of yttrium ions in zirconia matrix has been extensively investigated. Nowadays, ceramic engineers mainly focus on a Y_2O_3/ZrO_2 ratio of 3 or 8% due to their superior properties.² The ionic crystal radius of Y(III) (104 pm) is close to those of lanthanides (Tb(III) and Eu(III) have an ionic radius of 106.3 and 108.7 pm, respectively) and, more in general, their chemical behavior is comparable. Thus, similar solubility features are expected from rare earth (RE) doped zirconia. As a matter of fact, Eu-doped zirconia (up to 13%) was already synthesized by Ninjbadgar *et al.*³ Nevertheless, those systems have not been yet deeply studied. The presence of partially filled f orbitals in lanthanides gives to the material peculiar photoluminescent and paramagnetic properties that can be exploited in optical, magnetic and biological applications making these compounds particularly appealing. The first part of this chapter will focus on the study of the doping behavior of our zirconia nanoparticles with yttrium, europium and terbium ions. This part will also be important for the Chapter 6 in which the assembly behavior of these NPs in large supercrystals will be described as function of the doping and reaction conditions. The second part of the chapter will present the study of 8% Y_2O_3/ZrO_2 nanoparticles, their sintering behavior and their conduction properties. It will be shown that the nanometric size achievable exploiting the “benzyl alcohol route” can be particularly effective for improving the sintering condition and to enhance the conductivity of the final ceramic material. Although grain boundaries are known to be detrimental for the ionic conductivity, complex activating transport may rise in nanoceramic.⁴⁻⁵ The control of the ceramic microstructure restricting grain growth can be reached either by tailoring the sintering stages or by non conventional high pressure sintering methods.⁶⁻⁷ However, the engineering of the starting material is also a crucial point as it allows to control some important characteristics that influence the sintering behavior and the final properties of the ceramic material, that is the primary particle size and particle agglomeration.⁸

2 Results and Discussion

2.1 Structural and Morphological Characterization

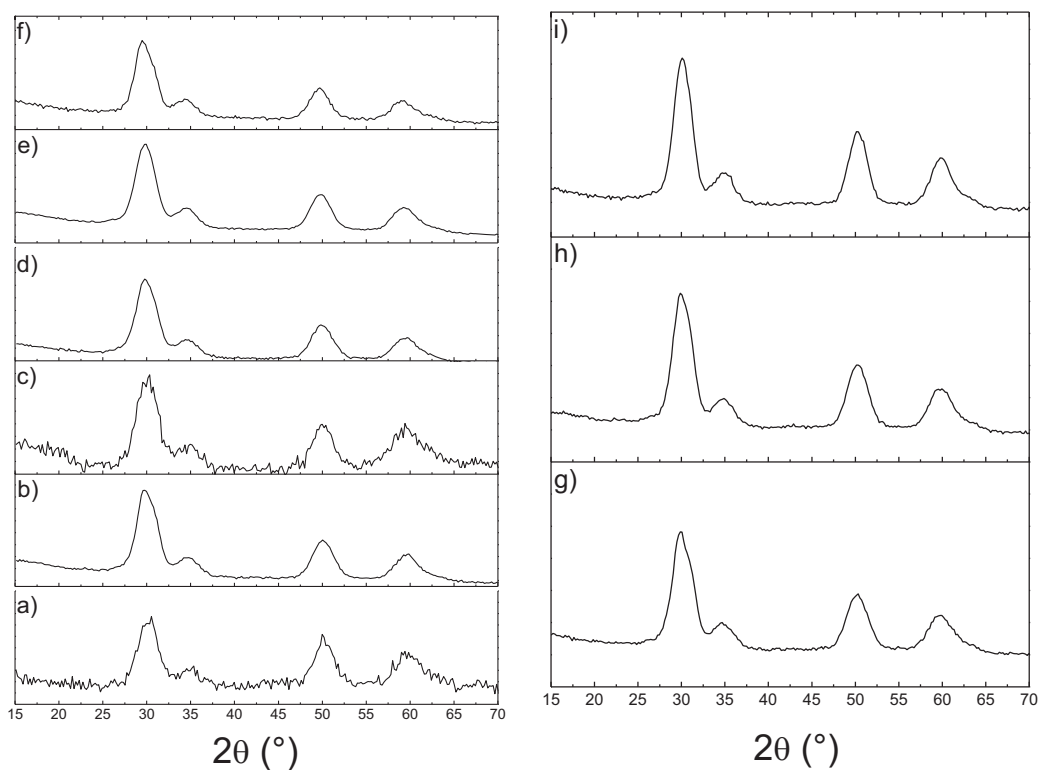


Figure 4.1: XRD of zirconia doped with europium (left) or terbium (right) at different percentage: 11(a), 13(b), 15(c), 17(d), 20(e), 23(f) and 3(g), 5(h) and 10%(i). The samples depicted here were synthesized at 230 °C in the case of Eu doping and 275 °C in the case of Tb.

According to the synthesis procedure presented in Chapter 2, the synthesis of RE-doped zirconia was carried out using different metal oxide precursors. For europium and terbium doping acetate hydrate complexes were used, whereas, for yttrium doping, isopropoxide and chloride homoleptic complexes were used. The yield of the reaction was greatly reduced upon terbium doping at the standard reaction temperature (230 °C), decreasing from around 90% for the pure zirconia to below 20%. Interestingly, europium doped zirconia did not show such a steep drop in yield.

However, due to this observation the synthesis temperature for all the materials discussed hereafter in this chapter was increased to 275 °C and above.

In the cases of the Y-doped samples, considering the different nature of the precursors (chloride and alkoxide), alternative reaction mechanisms may occur. Generally, when chlorides precursors are employed an alkylhalide elimination condensation step is expected, whereas an ether elimination or C-C coupling of benzylic alcohols and alkoxide molecules condensation steps can take place in the case of the pure metal alkoxide.⁹⁻¹⁰ The reaction yield was in this cases normalized to the amount of organics (calculated by TGA). The synthesis at 300 °C produced in both cases Y-doped zirconia with the yield being higher when yttrium chloride was used (94.3% compared to 82.2%). This result is expected considering the higher reactivity of chlorinated precursor in NHSG.¹⁰ As above mentioned, the research on YSZ was mainly focused on 3 or 8% Y₂O₃/ZrO₂ mixture. This amounts to a molar percentage in Y³⁺ dopant of 5.8 and 14.8, respectively. Those ratios were also considered in the present study (*cf.* Chapter 2, section 1.1).

Figure 4.1a and b show the XRD patterns of Eu-doped ZrO₂ synthesized at 230 °C and Tb-doped ZrO₂ synthesized at 275 °C, respectively, for different doping concentrations. As already discussed in the previous chapter (Chapter 3, section 2.2) the zirconium oxide synthesized via the benzyl alcohol route can be stabilized in either cubic or tetragonal modification. No appearance of second phases was discernable by means of XRD, even for the highly doped samples. Raman spectroscopy are ongoing in order to finally identify the structure although difficulties on the analysis, because of sample stability, were encountered. Preliminary results suggested that doping can actually force the crystal to form a tetragonal environment rather than the cubic one found for pure zirconia.¹¹ The same consideration can be done investigating the effect of the synthesis temperature on the final product. The diffractograms shown in Figure 4.2 (5.8 Y-doped ZrO₂ synthesized at 250, 300 and 350 °C) and Figure 4.3 (depicting zirconia doped with 14.8% of yttrium) are very much alike. In all the studied cases, the size of the nanocrystals only suffer minor changes (varying in the range between 2.9 and 4.4 nm, as estimated by Scherrer

formula, *cf.* Table 2.1 in Chapter 2) when modifying the nature and the amount of the dopant, as well as the reaction temperature. The only parameter that leads to a slightly different outcome is by choosing a different yttrium precursor. The XRD of the sample synthesized with YCl_3 (Figure 4.3, dotted line) shows sharper peaks, clearly indicating larger particles, which were estimated to be around 6 nm by the Scherrer formula.

As suggested from the Vegard's law, the introduction of a different ion into a certain matrix, for a solid solution, slightly modifies the relative distances between atoms leading to a shift of the diffraction peaks. The entity of the shift is rather small but became more evident at high diffraction angles. For example, substituting Zr^{4+} ions with the larger Y^{3+} ions into the cubic phase of zirconia (JCPDS [27–997]) till obtaining $\text{Y}_{0.15}\text{Zr}_{0.85}\text{O}_{1.93}$ (JCPDS [30–1468]) increases the 220 interplane distance from 1.80 to 1.82 Å, shifting the relative reflection from 50.64 to 50.14 2θ degrees. This small difference is clearly observable in bulk materials where the peaks are sharp and intense, but it becomes difficult to observe when moving to 3 nm particles. In the diffractograms of the various zirconia doped samples a shift becomes obvious, despite the broad peaks, only for highly doped samples (see for example Figure 4.1 left). This observation suggests that an effective substitution of the RE ions in the matrix takes place in our samples. Moreover, the absence of the XRD signature of the RE oxides and other RE-based hybrid materials, that can be synthesized following the “benzyl alcohol route”, suggests the absence of phase segregation.¹²⁻¹³

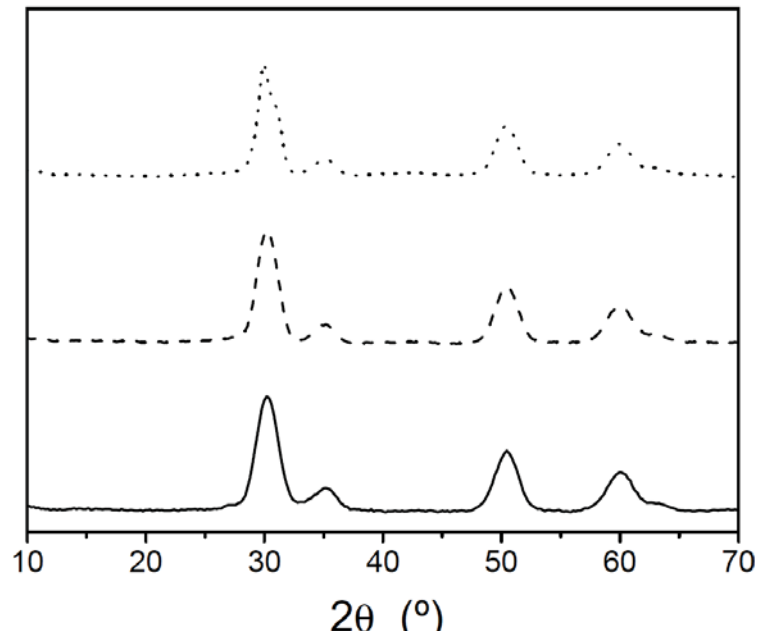


Figure 4.2: XRD of 5.8% Y-doped ZrO₂ synthesized at different temperature: 250 (full line), 300 (dashed line) and 350 °C (dotted line).

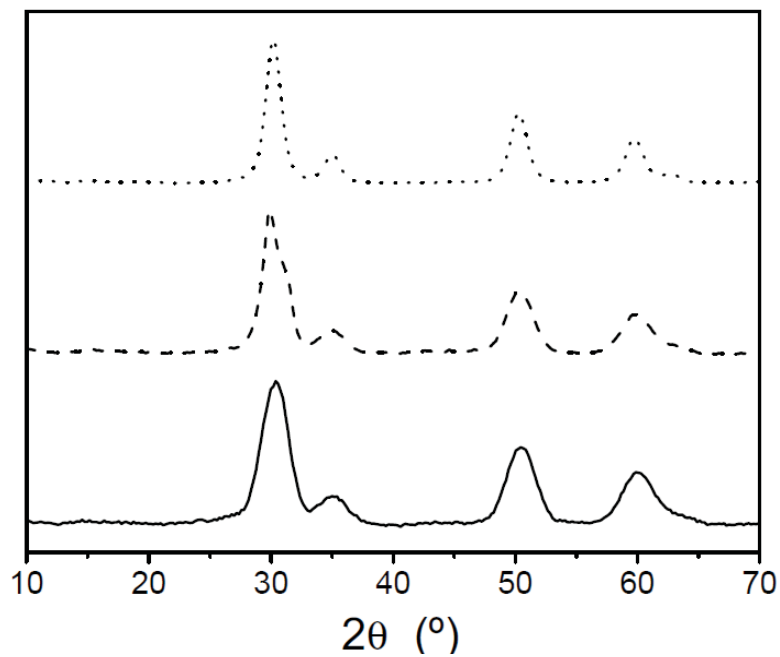


Figure 4.3: XRD of 14.8% Y-doped ZrO₂ synthesized at 250 °C (full line) and at 300 °C (dashed line) with yttrium alkoxide and the one synthesized at 300 °C using YCl₃ (dotted line).

Chapter 4 – Rare Earth Doped Zirconia

Transmission electron microscopy observations of the nanoparticles synthesized at 230-250 °C (Figure 4.4) confirmed what already found for TM-doped ZrO₂ (Chapter 3, section 2.2). The nanoparticles are highly crystalline and preserve a spherical shape irrespective of the nature and the percentage of the dopant (Figure 4.4). The particle size remains almost constants and ranges from 3 to 4.4 nm depending on the reaction temperature and the doping, confirming the findings obtained by means of XRD. Only in the case of the YSZ nanoparticles synthesized from YCl₃ the particles become substantially larger reaching 6 nm in diameter (Figure 4.4c and d).

With the increasing of the reaction temperature and the doping concentration a difference is observable in the way nanoparticles interact among each other. The small and disordered aggregates of nanoparticles as the ones presented in Figure 4.4 leave the place to supercrystals made by an ordered arrangement of highly monodisperse nanoparticles (*cf.* Figures 6.2 and 6.3). As already mentioned, this particular result will be deeply investigated in Chapter 6. On the other hand, the sample synthesized with YCl₃ precursor showed a lower degree of agglomeration. Large agglomerates of particles, although made of very small crystallites, are not suitable for sintering as they do not assure the homogeneity necessary to form densely packed pellets. Because of this, the investigation on the sintering behavior and ion conductivity discussed in the following section were carried out only on this latter sample.

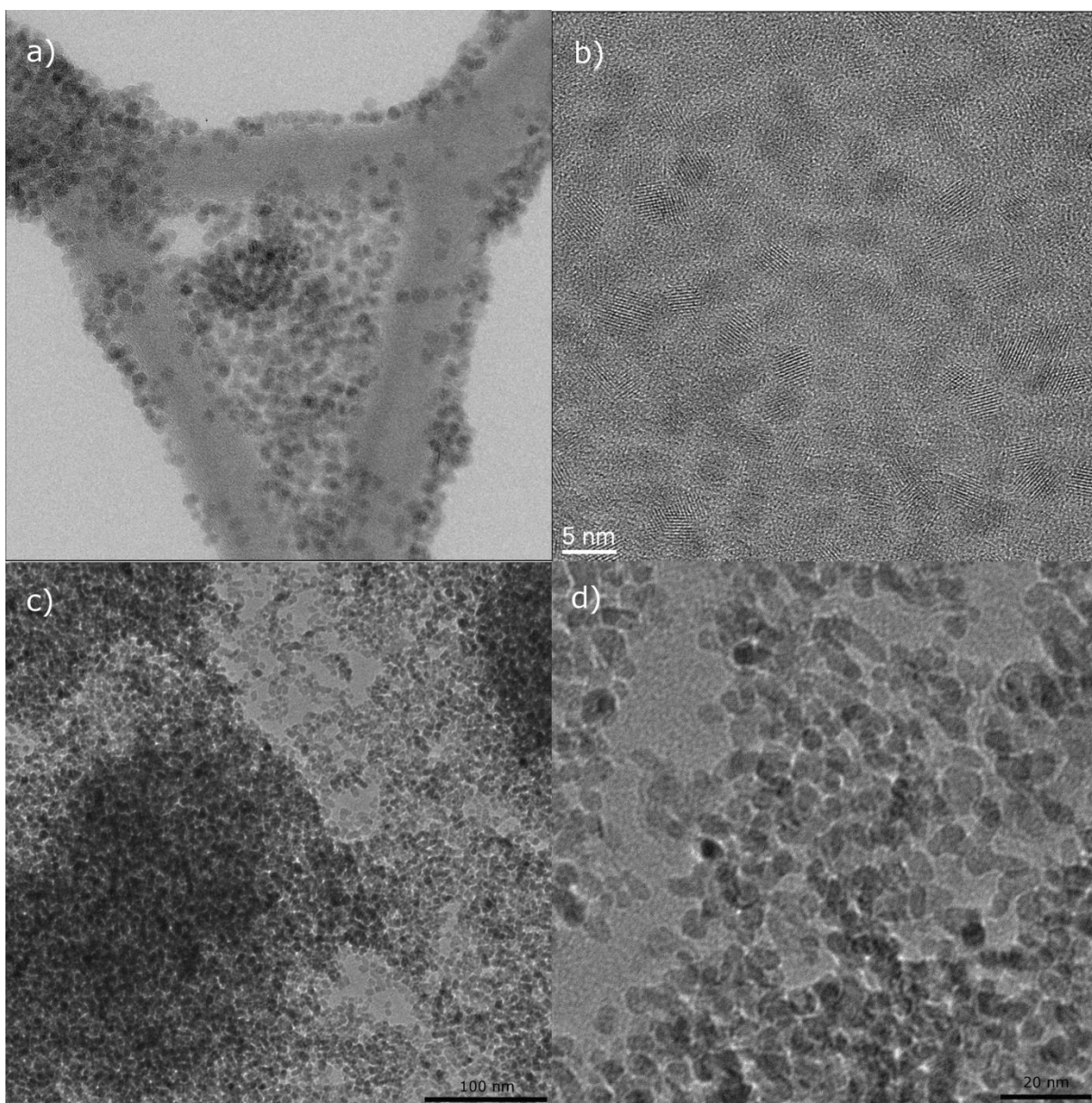


Figure 4.4: TEM and HRTEM images of functionalized Eu-doped ZrO_2 (a and b) and of Y-doped ZrO_2 prepared with YCl_3 precursor (c and d).

2.2 Electrochemical properties of 14.8% Y-doped ZrO₂

2.2.1 Sintering of the ceramics

The fine and reactive nanopowders can in principle be sintered at lower temperatures than conventional powders. The use of the 6 nm YSZ nanoparticles might improve the processes for the production of dense ceramic materials. Around 450 mg of the YSZ nanoparticles obtained by reacting Zr isopropoxide complex and YCl₃ in benzyl alcohol at 300 °C were pelletized using a uniaxial press and further densified with an isostatic press for 30 minutes at 300 MPa. The fractional density of these powder compacts was close to 80%, assuming a theoretical density of 6.10 g/cm³. The shrinkage behavior was studied by dilatometry. The pristine sample shows a smooth and continuous decrease of volume starting at 200 °C and up to 1050 °C, after which a marked increase of the densification rate is apparent until a steady state plateau is obtained for temperatures above 1300 °C (Figure 4.5). The loss of volume at temperatures lower than approximately 600 °C can be attributed to the removal of water and organics. This was partly confirmed by the elemental CHN analysis, which measured a carbon amount as high as 8%, and by thermal gravimetry, which showed a marked weight loss around 500 °C accountable to 6% of the sample total weight. On the other hand, in agreement with observation, the initial shrinkage stage of a sample obtained from powder pre-calcined at 500 °C for 3 hours (thus free from the organics) starts only at 600 °C, and it displays the same fast second stage shrinkage above 1050 °C. The first shrinkage, stage between ~600 °C and 1050 °C, is usually not reported for zirconia powders and may thus be ascribed to a first rearrangement of the nanoparticles.

It should be noticed that the final linear shrinkage was about 19% for the as prepared sample (solid line in Figure 4.5), whereas a much higher value (~23%) was attained for the pre-calcined samples (dashed line). These data clearly demonstrate the negative impact of the organics resulting from the synthesis steps on the densification kinetics of these nanopowders.

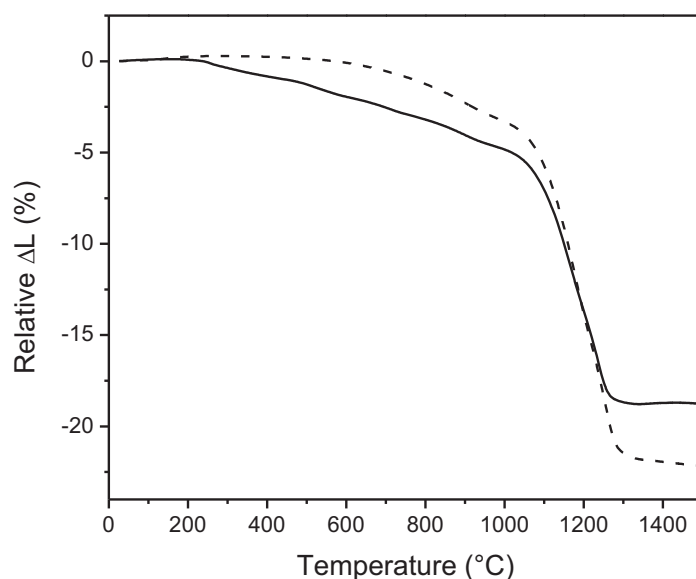


Figure 4.5: Dilatometry plot of the pristine Y-doped ZrO₂ nanopowder (solid line) and of the same sample obtained from powder pre-calcined for 3h at 500 °C (dashed line).

The subsequent investigation of the sintering behavior of these powders in isothermal conditions and of the resulting ceramics was thus conducted with the pre-calcined samples. Three sintering temperatures (1300, 1400 and 1500 °C) were selected based on the shrinkage curves so that ceramics free from percolating porosity could be obtained. Fractional densities of 91, 93 and 96% were achieved for samples sintered at 1300, 1400 and 1500 °C in air during 4h (heating rate of 5 K/min), respectively. The microstructure of the sintered samples was analyzed by SEM, as shown in Figure 4.6. Fractured cross section of the pellets were polished and chemically etched during 5 min in hydrofluoric acid in order to reveal the grain boundaries. The chemical treatment was preferred over the thermal etching because of experimental constraints related to the availability of furnaces. The SEM micrographs indeed reveal a strong dissolution of the grain boundaries, which tends to decrease with increasing sintering temperature. Such a strong effect of the acid on the samples sintered at the lower temperatures is somewhat unexpected and may indicate local composition inhomogeneities at the grain boundary regions, as already

observed in the case of annealed Mn-doped zirconia (*cf.* Chapter 3). The porosity fraction apparent in these images is clearly above that expected from the measured fractional densities. Nevertheless, it is possible to clearly identify differences in the average grain size of the prepared ceramics. The sample treated at 1300 °C shows grain size lower than 1 μm (Figure 4.6a). Increasing the sintering temperature to 1400 °C (Figure 4.6b) leads to a further densification while the grain size remains of the order of 1 μm . Finally, the sintering treatment at 1500 °C led to an average grain size around 3 to 4 μm (Figure 4.6c) which is typical for cubic yttria-stabilized zirconia.

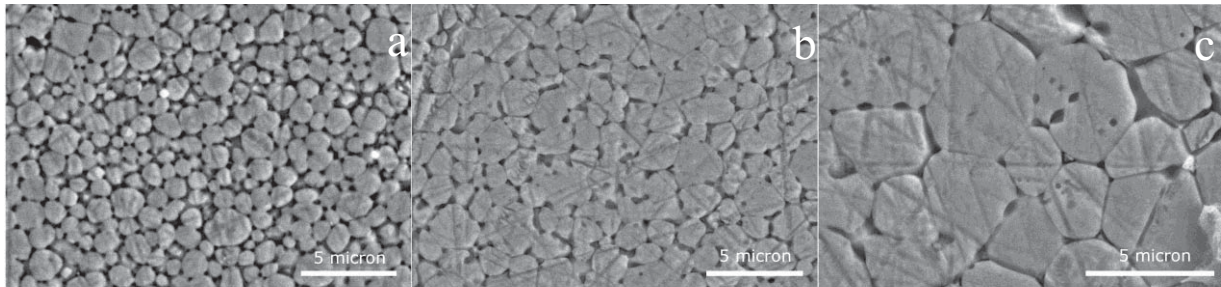


Figure 4.6: SEM micrographs of YSZ sintered at (a) 1300, (b) 1400 and (c) 1500 °C.

2.2.2 Electrical conductivity

The ionic conductivity of the sintered pellets was measured in air at different temperatures. Figure 4.7 depicts the impedance spectra measured at 350 °C for the samples annealed at the three sintering temperatures. All the samples show two contributions, one at high frequency due to the grain interior (bulk), and another at low frequency, which can be ascribed to the grain boundary. The sintering temperature has opposite effects on both contributions, being of much greater amplitude for the grain boundary impedance. On the one hand, the bulk impedance tends to slightly increase with increasing sintering temperature. On the other hand, the grain boundary semicircle is strongly reduced with increasing sintering temperature. While the bulk effect may be due to dopant segregation, the grain boundary differences are the direct consequence of the different grain size. Indeed, with the increase of the grain

dimensions (resulting from higher sintering temperature) the density of grain boundaries decreases, thus decreasing their relative resistive contribution. A possible role of porosity cannot at this point be excluded since, particularly for the sample sintered at 1300 °C, the fractional density is at the border line of the existence of percolating pores (<93%). The contribution of such purely dimensional effects (grain size and porosity) may be separated from possible compositional effects (related to the dopant segregation) by a detailed analysis of the grain boundary conductivity in light of a simple model description referred to as the “brick layer model” (BLM).¹⁴⁻¹⁵ This analysis is attempted in the following lines.

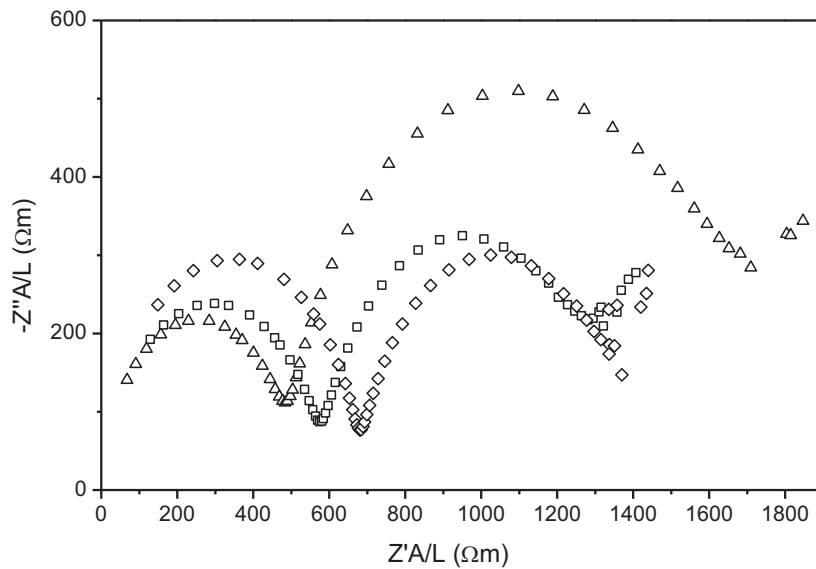


Figure 4.7: Representative impedance spectra obtained at 350 °C for the YSZ sintered at 1300 °C (triangle), 1400 °C (square) and 1500 °C (rhomb).

The BLM is a simplified depiction of the ceramic material that allows to interpret the electrical behavior dependence on the frequency considering each grain as two parallel resistor-capacitor network one representing the grain interior and the other one to represent the boundaries. A schematic of the equivalent circuit used is depicted in Figure 4.8. The circuit parameters were estimated by a nonlinear fitting

program using ZView software. The response of the electrode was systematically subtracted.

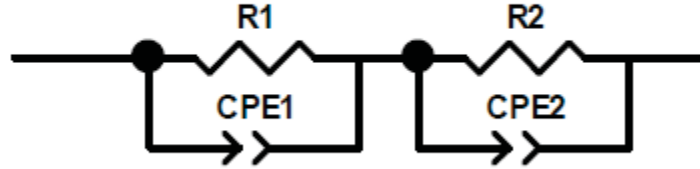


Figure 4.8: Equivalent electrical circuit chosen at low temperatures. R1 represents the resistance of the bulk, R2 the resistivity of the grain boundary while the CPEs are constant phase elements representing dielectric effects in the two regions.

The conductivity data calculated for the different samples are superimposed suggesting that the bulk conductivity is only marginally affected by the sintering temperature. However, a clear effect can be observed on the grain boundary conductivity plot (Figure 4.9a). This region of the ceramic material is known to be detrimental to the ion conductivity. As previously seen, smaller grain size present more relevant grain boundary phenomena resulting on a lower conductivity (see triangles in Figure 4.9a) The specific grain boundary conductivity was calculated as described in ref. ¹⁶, with the following formula:

$$\sigma_{gb,sp} = \frac{L\delta_{gb}}{AR_{gb}G} = \frac{LC_b}{AR_{gb}C_{gb}} \quad (\text{Eq. 4.1})$$

where L and A are geometrical parameters (respectively thickness of the sample and surface area of the electrodes). R_{gb} is the grain boundary resistance. δ_{gb} is the grain boundary thickness, C_b and C_{gb} are the bulk and boundary capacitance, respectively. Since the δ_{gb} is unknown and the C_b values are usually affected by uncertainties related to stray capacitances, it is preferable to estimate the specific grain boundary conductivity by

$$\sigma_{gb,sp} = \frac{\epsilon_0 \epsilon_r}{R_{gb} C_{gb}} \quad (\text{Eq. 4.2})$$

where ϵ_0 is the permittivity of vacuum and ϵ_r is the relative permittivity, considered in our case to be 55, which is a standard value for YSZ single crystal for temperature higher than 250 °C.¹⁷ Figure 4.9b shows that δ_{gb} is independent of the microstructure, thus confirming that the differences in the apparent grain boundary conductivity can be simply explained by a grain size effect, and that possible contributions from percolating porosity or compositional differences are thus negligible.

Nevertheless, even for the best sample here presented, the grain boundary impedance is comparable to the bulk impedance. This is in contrast with what is reported for YSZ ceramics with comparable grain size, usually displaying much lower grain boundary resistances.¹⁸

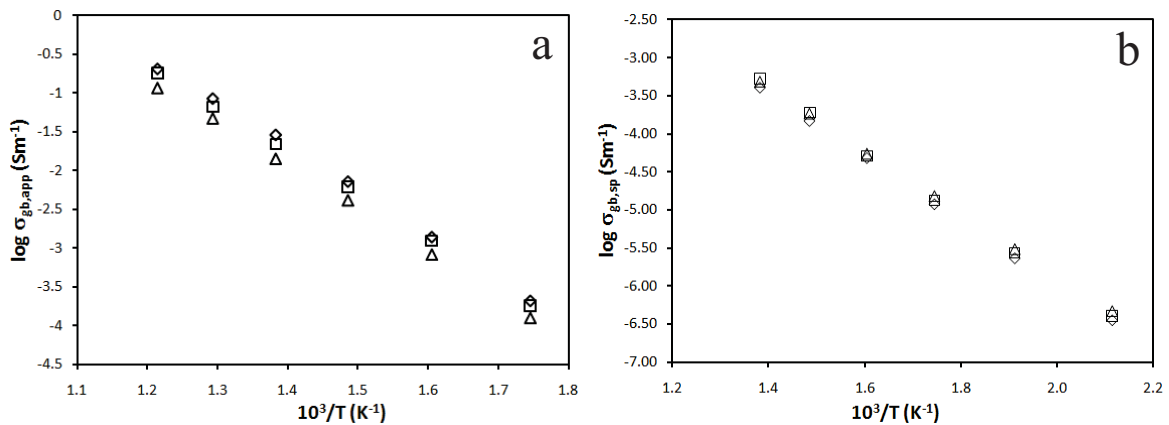


Figure 4.9: Temperature dependence of the apparent grain boundary (a) and specific grain boundary (b) conductivity obtained for the YSZ sintered at 1300 (triangle), 1400 (square) and 1500 °C (rhomb).

The grain boundary region is known to have different thermodynamic properties compared to the bulk. In general the outer region present a higher concentration of

defect originating in a difference of charge compared to the center of the grain. This result in a driving force that might enhance or refrain ionic or electronic conduction.

The difference between the potential at the grain boundary core and the bulk of the grain ($\Delta\Phi$) can be estimated from the ratio between the bulk and the specific grain boundary conductivity according to ref. ¹⁹.

$$\frac{\sigma_b}{\sigma_{gb,sp}} = \frac{e \left(\frac{2e\Delta\Phi}{kT} \right)}{\frac{4e\Delta\Phi}{kT}} \quad (\text{Eq.4.3})$$

These values are shown in Figure 4.10 for the three ceramics prepared in this work. It can be seen that $\Delta\Phi$ is nearly independent of the sintering conditions, with just a slight deviation being observed for the high temperatures (accountable, perhaps, by the assumption of a temperature independent ϵ_r). Moreover, the space charge potential of these samples fit well within literature data^{18,20} for the same composition. Therefore, one may speculate that the relatively poor grain boundary conductance of the samples obtained in this work is due to the presence the impurities existing in the initial precursors, being silica and some transitional elements the most likely. This will obviously imply a systematic analysis of these samples by TEM and complementary analytical techniques, notably EELS.

The value for bulk, grain boundaries and total activation energies are listed in Table 4.1 together with the conductivity measured at different temperatures. As the activation energy for the grain boundaries is higher than for the bulk, their contribution to the total resistance of the sample tends to decrease with increasing temperature. The values for the high temperature sintered samples are higher than those obtained with a similar sintering process on commercially available zirconia, such as Tosoh powder, even if in that case the density reached 99%.^{18,21}

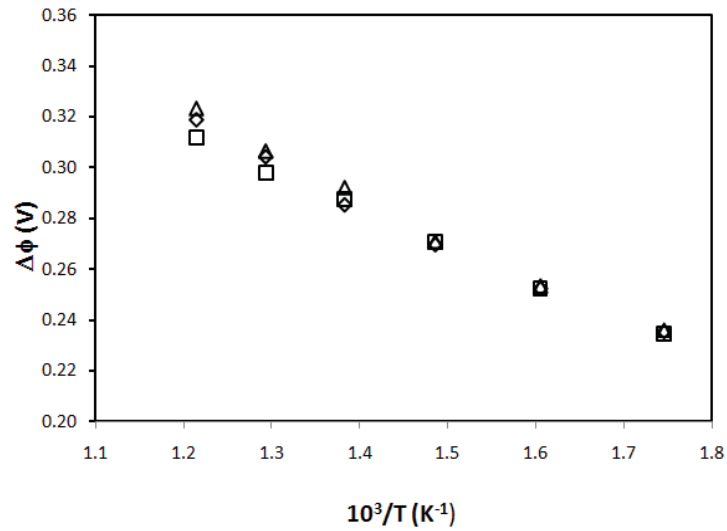


Figure 4.10: Temperature dependence of the space charge potential obtained for the YSZ sintered at 1300 (triangle), 1400 (square) and 1500 °C (rhomb).

Table 4.1: Activation energy and conductivities in the range 350-1000 °C for the sample calcined at 1300, 1400 and 1500 °C.

Reaction temperature (°C)	E_b (eV)	Conductivity at 350 °C (S/m)	E_{gb} (eV)	Conductivity at 500 °C (S/m)	Conductivity at 800 °C (S/m)	E_t (eV)	Conductivity at 1000 °C (S/m)
1300	1.13	5.86×10^{-04}	1.17	3.18×10^{-02}	$2.14 \times 10^{+00}$	1.05	$1.30 \times 10^{+01}$
1400	1.12	7.28×10^{-04}	1.18	3.65×10^{-02}	$1.83 \times 10^{+00}$	1.03	$1.36 \times 10^{+01}$
1500	1.13	7.17×10^{-04}	1.14	3.95×10^{-02}	$2.25 \times 10^{+00}$	1.07	$8.58 \times 10^{+00}$

3 Conclusions

In the present chapter the doping of zirconia nanoparticles synthesized following the “benzyl alcohol route” with diverse rare earth ions was presented. The doping of zirconia with carboxylate or alkoxyde RE precursors, similarly to what reported in Chapter 3 for Cr and Mn doping, does not modify the particle size compared to pure samples. Indeed, in each case gram scale quantity of 3-4 nm nanocrystals could be obtained at high yields. Different is the case of chlorinated precursors. These compounds proved to be more reactive than their metalorganic counterpart, leading with high yield to less defined and larger (6 nm) nanocrystals.

After the assessment of the nanostructure–reaction parameters relationship, 6 nm YSZ nanoparticles synthesized from YCl_3 were chosen for a case study. These nanoparticles demonstrated a high sinterability obtaining a degree of densification above 90% even at relatively low temperature treatments and following simple sintering procedure. The ionic conductivity demonstrated to be comparable to those of the best commercial YSZ powders. Interestingly, at high processing temperature the total conductivity is higher than the one obtained with the iso-doped Tosoh powder reported in literature. The study reported in this chapter could be further extended to a different load of doping cation (*i.e.* the 3% Y_2O_3/ZrO_2 mixture). Moreover, even more interesting results could be obtained by optimizing the sintering procedure for example by implementing a two-step process.

4 Bibliography

- (1) Singhal, S. C. *Solid State Ionics* **2002**, *152*, 405.
- (2) Ciacchi, F. T.; Crane, K. M.; Badwal, S. P. S. *Solid State Ionics* **1994**, *73*, 49.
- (3) Ninjbadgar, T.; Garnweitner, G.; Börger, A.; Goldenberg, L. M.; Sakhno, O.; Stumpe, J. *Advanced Functional Materials* **2009**, *19*, 1819.
- (4) Maier, J. Z. *Phys. Chem.* **2003**, *217*, 415.
- (5) Fleig, J. *Solid State Ionics* **2000**, *163*, 131.
- (6) Maca, K.; Pouchly, V.; Zalud, P. *Journal of the European Ceramic Society* **2010**, *30*, 583.
- (7) Lourenço, M. A.; Cunto, G. G.; Figueiredo, F. M.; Frade, J. R. *Materials Chemistry and Physics* **2011**, *126*, 262.
- (8) Lu, K. *Int. Mater. Rev.* **2008**, *53*, 21.
- (9) Niederberger, M.; Garnweitner, G. *Chemistry - A European Journal* **2006**, *12*, 7282.
- (10) Niederberger, M.; Pinna, N. *Metal Oxide Nanoparticles in Organic Solvents*; Springer London, 2009.
- (11) Garnweitner, G.; Goldenberg, L. M.; Sakhno, O. V.; Antonietti, M.; Niederberger, M.; Stumpe, J. *Small* **2007**, *3*, 1626.
- (12) Karmaoui, M.; Sa Ferreira, R. A.; Mane, A. T.; Carlos, L. D.; Pinna, N. *Chemistry of Materials* **2006**, *18*, 4493.
- (13) Karmaoui, M.; Sá Ferreira, R. A.; Carlos, L. D.; Pinna, N. *Materials Science and Engineering: C* **2007**, *27*, 1368.
- (14) Bauerle, J. E. *J. Phys. Chem. Solid* **1969**, *30*, 2657.
- (15) Verkerk, M. J.; Middelhuis, B. J.; Burggraaf, A. J. *Solid State Ionics* **1982**, *6*, 159.
- (16) Abrantes, J. C. C.; Labrincha, J. A.; Frade, J. R. *J. Am. Ceram. Soc.* **2000**, *20*, 1063.
- (17) Perry, N. H.; Kim, S.; Mason, T. O. *J. Mater. Sci.* **2008**, *43*, 4684.
- (18) Fernandes, C. M.; Castela, A.; Figueiredo, F. M.; Frade, J. R. *Solid State Ionics* **2011**, *193*, 52.
- (19) Guo, X.; Maier, J. *J. Electrochem. Soc.* **2001**, *148*, E121.
- (20) Boulfrad, S.; Djurado, E.; Dessemond, L. *Fuel cells* **2008**, *5*, 313.
- (21) Gathe, M.; Shariat, M. H.; Irvine, J. T. S. *Solid State Ionics* **2009**, *180*, 57.

CHAPTER 5*

Lithium Titanium Oxide

*This chapter is based on: S.-H. Yu, A. Pucci, T. Hertrich, M.-G. Willinger, S.-H. Baek, Y.-E. Sung, N. Pinna *J. Mater. Chem.* **2011**, 21, 806

Table of contents

1 Introduction 91

2 Results and Discussion..... 93

 2.1 Structural and Morphological Characterization93

 2.2 Electrochemical properties97

3 Conclusions 101

4 Bibliography 103

1 Introduction

There is a clear need for novel nanomaterials for rechargeable lithium batteries in order to “achieve the increase in energy and power density essential to meet the future challenges of energy storage”.¹

Clearly, the development of such advanced materials demands for a rational synthesis through controlled and well understood protocols, which allow controlling the size, homogeneity and assembly behaviors. Only well defined materials and homogeneous nanostructures will permit the establishment of a clear structure-functionality relationship and permit to go beyond the present state of the art.

As already discussed in the introduction of this manuscript, NHSG and, in particular, the “benzyl alcohol route” provides a powerful but simple reaction pathway through a reduced reactivity of the precursor allowing an easier access to the engineering and the fabrication of complex multi-metal oxides. In this chapter, that particular feature is further highlighted in the synthesis of lithium titanium oxide (LTO).

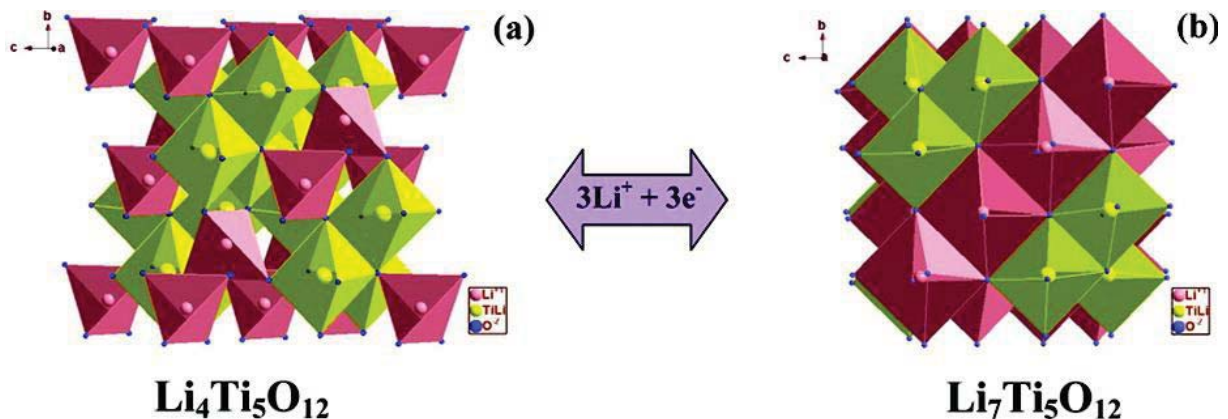


Figure 5.1: The Li^+ intercalation/deintercalation equilibrium between the two LTO phases.

Among the LTO phases, the spinel $\text{Li}_4\text{Ti}_5\text{O}_{12}$ is a promising anode material for high-rate lithium-ion batteries showing intrinsic safety, good load capability, and excellent low temperature performance. This, together with the long cycle life, due to the zero-strain insertion during the passage from the reduced ($\text{Li}_7\text{Ti}_5\text{O}_{12}$) to the oxidized

($\text{Li}_4\text{Ti}_5\text{O}_{12}$) phase (*i.e.* no volume change during the intercalation/deintercalation process, as depicted in Figure 5.1), make this material highly appealing for portable devices and electric vehicles. Although the investigation of the electrochemical properties of LTO is relatively recent,¹⁰ in the last two decades a prompt application in the everyday life of the lithium ion battery technology acted as a boost for the research on such a material.

$\text{Li}_4\text{Ti}_5\text{O}_{12}$ is generally prepared by solid state reaction from TiO_2 and Li_2CO_3 or LiOH .¹⁰⁻¹⁷ Soft chemistry processes were also investigated such as sol-gel¹⁸⁻²⁶ and hydrothermal.²⁷⁻³⁰ For example, Kavan et al. synthesized it from the hydrolysis and condensation of lithium and titanium alkoxides followed by a high temperature annealing.¹⁹ Mesoporous $\text{Li}_4\text{Ti}_5\text{O}_{12}$ was produced by a hydrothermal method followed by calcination at 500 °C.²⁷ Very recently, a solution combustion route at 800 °C led to nanocrystalline $\text{Li}_4\text{Ti}_5\text{O}_{12}$ in less than a minute.³¹ However, to the best of our knowledge no crystalline $\text{Li}_4\text{Ti}_5\text{O}_{12}$ was so far obtained by soft chemistry routes. In each case, a post synthesis calcination step was required, which generally does not permit to preserve or control the nanostructure.

In this chapter a one-pot template-free solvothermal synthesis of crystalline $\text{Li}_4\text{Ti}_5\text{O}_{12}$ hierarchical nanostructures based on the “benzyl alcohol route” is introduced. The as-synthesized crystalline nanostructures show good lithium intercalation/deintercalation performance at high rate (up to 30 C) and a good cycling stability. Annealing of the nanostructures at 750 °C improves the performance to a regime close to the theoretical capacity of $\text{Li}_4\text{Ti}_5\text{O}_{12}$. Furthermore, no noticeably capacity loss (less than 5%) is detected after 200 cycles.

2 Results and Discussion

2.1 Structural and Morphological Characterization

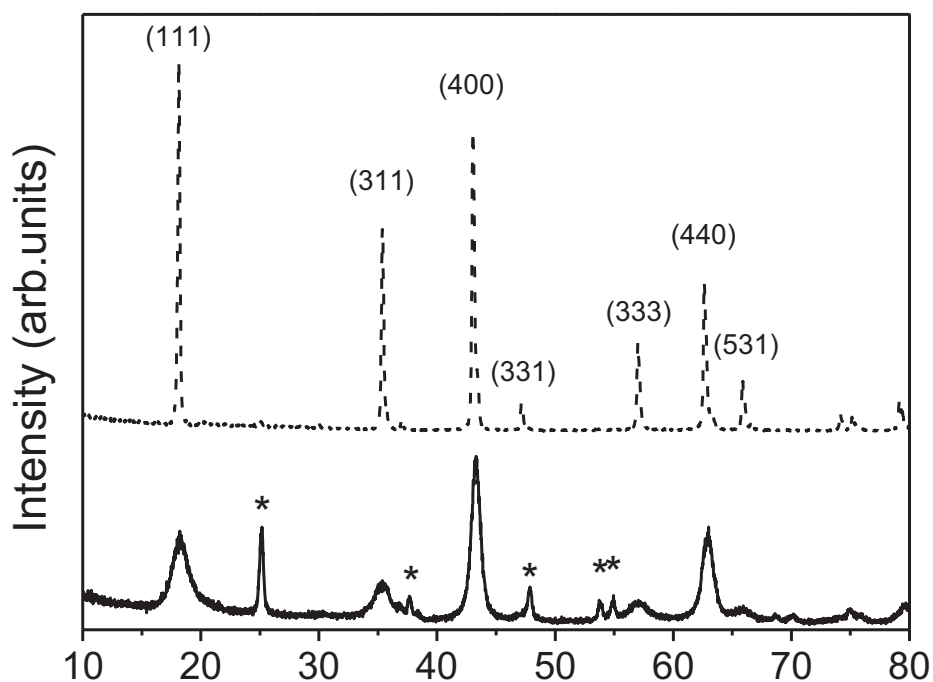


Figure 5.2: XRD pattern of the as prepared LTO nanostructures (full line) and after calcination at 400 °C for 1 h and at 750 °C for 1 h (dashed line) (Li:Ti concentration ratio of 7.2:7.6 mmol). The peaks denoted with an * are due to TiO_2 anatase phase impurity which is not any more detected after annealing at 750 °C.

The reaction between lithium alkoxide, formed from the *in situ* oxidation of Li metal, and titanium isopropoxide in benzyl alcohol led to the production with high yield of a white powder (*cf.* section 1.4 in Chapter 2).

The as-synthesized powder was characterized by X-ray diffraction (XRD), as shown in Figure 5.2. The most intense diffraction peaks of the pristine sample at 18.5°, 43.5° and 63.3° correspond to the (111), (400) and (440) reflections of the spinel $\text{Li}_4\text{Ti}_5\text{O}_{12}$ structure, respectively (Figure 5.2, solid line). Additional low intensity peaks such as

the (311) and (333) at around 35° and 57° are clearly visible. In general, the intensity of the diffraction peaks observed does not correspond to the standard data of $\text{Li}_4\text{Ti}_5\text{O}_{12}$ phases (e.g. ICDD 00-049-0207). Indeed, the (111) reflection is expected to be the most intense. Moreover, the width of the peaks is non-uniform and the crystallite sizes evaluated from the Scherrer equation are 10 nm for the (400) and (440) reflections and around 5 nm for the (111) reflection. This apparent discrepancy can be explained by the fact that the nanocrystals are not spherical, but instead, show a platelet-like morphology. In addition, some peaks that are attributed to anatase TiO_2 , as an impurity phase are clearly visible. Due to the much larger TiO_2 particle size (the average particle size extracted from Scherrer equation is 30 nm) the anatase impurity can be estimated to account for only a few mass percent. The anatase impurity can be inhibited by increasing the lithium amount during the synthesis. This is demonstrated by the XRD pattern shown in Figure 5.3a, where, based on an initial Li:Ti concentration ratio of 8.5:8 mmol, only the peaks due to the $\text{Li}_4\text{Ti}_5\text{O}_{12}$ phase are present. The annealing of the samples at 750 °C produces an increase of the particle size, hence facilitating the phase analysis of the XRD pattern (Figure 5.3b). In the case of the increased lithium amount, the obtained pattern shows peaks that are characteristic for two LTO phases: the spinel $\text{Li}_4\text{Ti}_5\text{O}_{12}$ (ICDD 00-049-0207) and the monoclinic Li_2TiO_3 (ICDD 04-009-1068). On the other hand, the annealing at 750 °C of the sample synthesized at lower lithium content (Li:Ti concentration ratio of 7.2:7.6 mmol) leads to pure phase $\text{Li}_4\text{Ti}_5\text{O}_{12}$ (ICDD 00-049-0207). Hence, the anatase impurity of the pristine sample can not be detected anymore after the heat treatment (Figure 5.2, dashed line). Unfortunately, a phase pure pristine $\text{Li}_4\text{Ti}_5\text{O}_{12}$ could not be obtained by empirically changing the Li:Ti concentration ratio.

Under consideration of the fact that i) $\text{Li}_4\text{Ti}_5\text{O}_{12}$ is the most suited LTO phase for lithium-ion batteries application and ii) that the monoclinic Li_2TiO_3 has poor electrochemical properties and finally iii) that the TiO_2 impurities are less detrimental to the charge/discharge properties and furthermore can be easily converted to

$\text{Li}_4\text{Ti}_5\text{O}_{12}$ upon annealing,³² the following part of the manuscript will focus on the sample synthesized under the Li:Ti concentration ratio of 7.2:7.6 mmol.

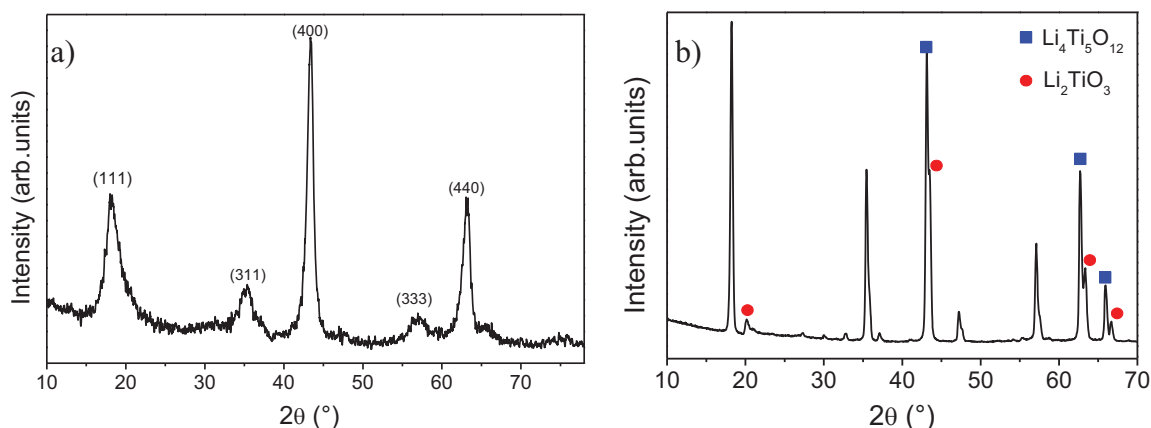


Figure 5.3: XRD pattern of the as-prepared (a) and calcined (b) LTO nanostructures with a Li:Ti concentration ratio of 8.5:8 mmol. The excess of lithium permits to eliminate the TiO_2 anatase phase impurity, however it promotes the formation of Li_2TiO_3 .

The result of the CHN analysis proves that the as-synthesized material is rather pure as only 2.5% of carbon is found. Indeed, this is very low compared to metal oxide nanoparticles synthesized by template- or surfactant-assisted syntheses.²

Scanning electron microscopy (SEM) images of the as-synthesized LTO reveal the presence of 1-2 μm sized spherical particles (Figure 5.4a). They are characterized by a nanostructured surface (Figure 5.4a inset). The selected area electron diffraction (SAED) recorded from such a nanostructure presents Debye-Scherrer rings that can be ascribed to nanocrystallites of the spinel $\text{Li}_4\text{Ti}_5\text{O}_{12}$ structure (Figure 5.4b). The transmission electron microscopy (TEM) image of one particle (Figure 5.4c) confirms that the surface is constituted of nanocrystallites in the size range of a few nm. The high resolution image of the peripheral region (Figure 5.4d) denotes the presence of platelet-like nanocrystallites of around 10 nm in diameter, confirming the above interpretation of the XRD results.

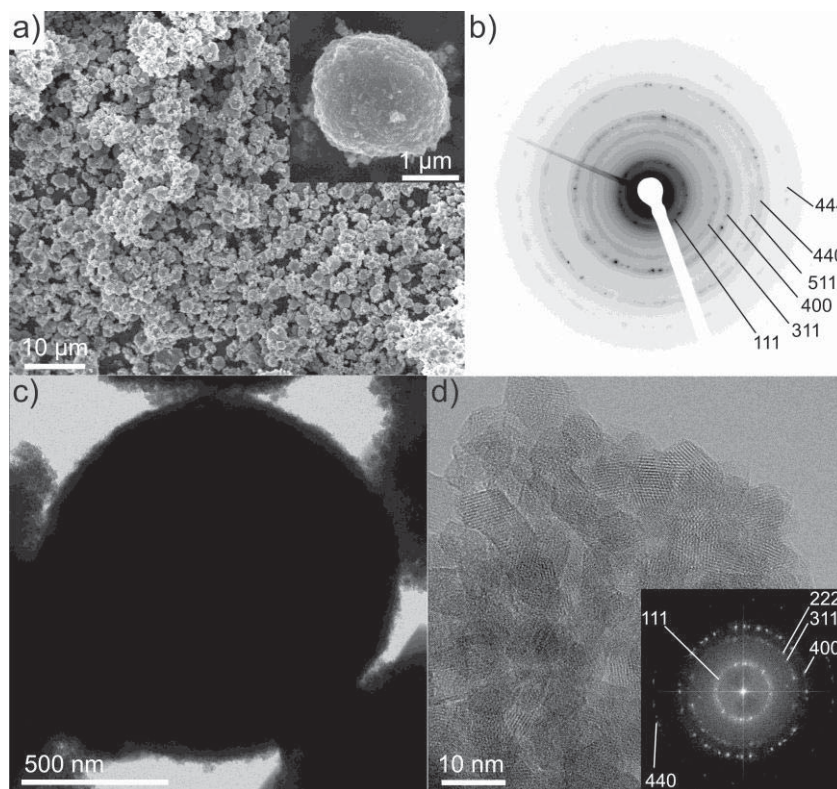


Figure 5.4: a) SEM overview image of the pristine LTO micrometer sized spherical particles. A single particle is shown in the inset. b) SAED of a part of one particle showing reflection rings corresponding to the spinel LTO structure, c) TEM overview image of one particle and d) HRTEM recorded from of an edge region of one particle showing the platelet-like shape of the individual nanocrystals. The inset of d) shows the corresponding power spectrum with the reflections corresponding to the spinel LTO structure.

The lattice fringes of the particles are clearly visible and prove that the nanocrystals are crystallographically randomly oriented with respect to each other. The lattice distances extracted from the power spectrum (Figure 5.4d inset) are in agreement with the ones of the $\text{Li}_4\text{Ti}_5\text{O}_{12}$ phase. The annealing treatment lead to an increase of the size of the nanocrystals, however without modifying the size and the spherical morphology of the superstructures as it can be clearly observed from the SEM images (Figure 5.5). However, the annealing process not only strongly affects the crystallite sizes, but also the Brunauer–Emmett–Teller surface area which decreases from $73 \text{ m}^2/\text{g}$ to only $8 \text{ m}^2/\text{g}$.

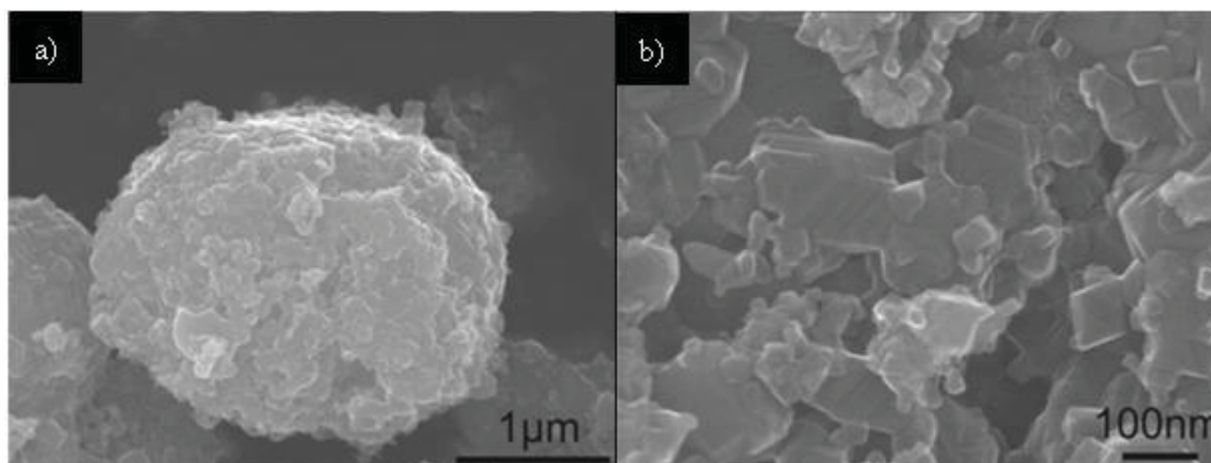


Figure 5.5: HRSEM images of the LTO micrometric sized particles annealed at 750 °C. a) Single particle and b) detail of the nanostructured surface.

When metal alkoxides are reacted in benzyl alcohol, the most likely condensation reactions leading to the formation of M-O-M bridges are the ether elimination³³ and the C-C coupling of benzylic alcohols and alkoxide precursors.³⁴ Although the formation of titania from the reaction of titanium isopropoxide in benzyl alcohol passes through the ether elimination reaction scheme,⁷ the addition of a barium metal or alkaline species (e.g. Na(OEt) or K(O^tBu)) are a prerequisite for the occurrence of a C-C coupling mechanism in the system.³⁴ The analysis by means of GC-MS and NMR of the reaction mixture of the LTO system speaks for a predominant C-C coupling mechanism similar to the one found for BaTiO₃. As a matter of fact, a three time fold amount of 4-phenyl-2-butanol (*i.e.* the main reaction product of the C-C coupling mechanism) compared to benzyl ether (*i.e.* the main reaction product of the ether elimination mechanism) was detected.

2.2 Electrochemical properties

The voltage profiles of the as-prepared sample present a gentle slope on plateaus (Figure 5.6a), which is attributed to titanium oxide impurity.³⁵ Still, the presence of the plateau speaks for the crystallinity of pristine nanoparticles. On the other hand, the

charge/discharge curves of the calcined sample are typical profiles of pure $\text{Li}_4\text{Ti}_5\text{O}_{12}$ (Figure 5.6b). They exhibit flat plateaus around 1.5 - 1.6 V (vs Li/Li^+), which correspond to the reversible phase transition between $\text{Li}_4\text{Ti}_5\text{O}_{12}$ and $\text{Li}_7\text{Ti}_5\text{O}_{12}$.³¹ For both pristine and calcined samples the potential plateau becomes shorter and gradually bends with the increasing of the charging/discharging rate due to a growing polarization effect. Another consequence is a bigger potential margin between the charge and discharge plateau which is much more evident for the calcined sample. Indeed, the small size of the pristine particles assures a lower polarization and a better reaction kinetic because of large surface area.

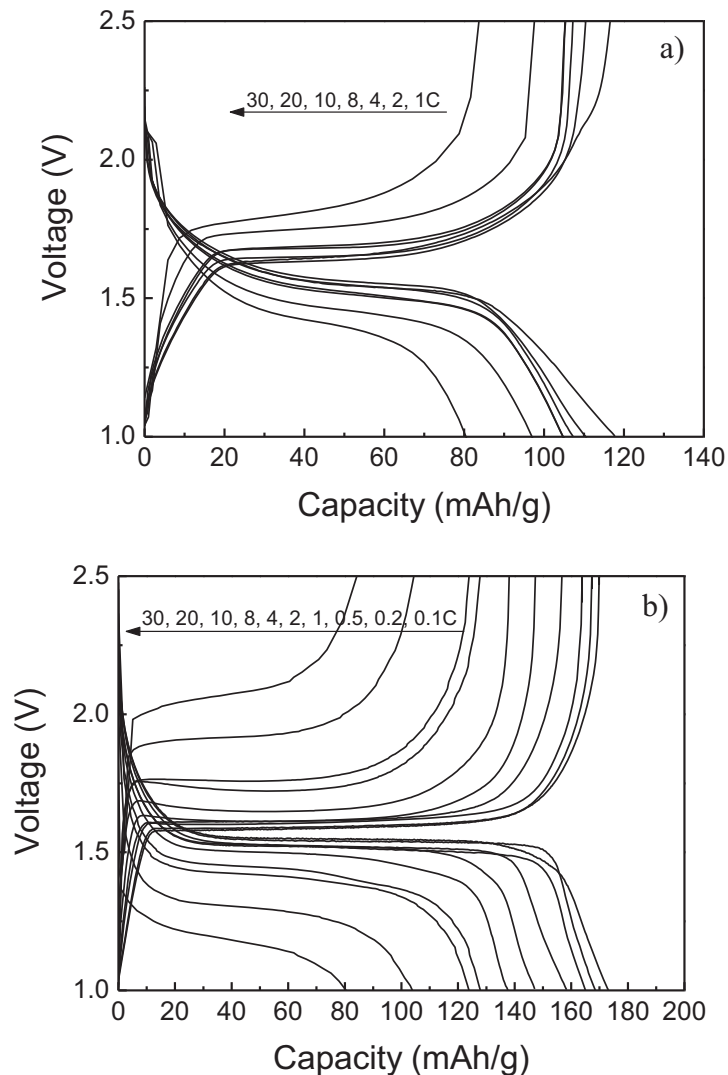


Figure 5.6: Capacity-voltage profiles for as-synthesized (a) and calcined (b) nanocrystalline $\text{Li}_4\text{Ti}_5\text{O}_{12}$.

The capacity versus cycle number plots for the pristine and calcined LTO samples are shown in Figure 5.7. The coulombic efficiency in the first cycle of the as-synthesized sample is low (~78.7%). The loss of the irreversible capacity in the first cycle is mainly attributed to titanium oxide impurities. As a matter of fact, a high irreversible capacity in the first cycle in various titanium oxides phases has already been reported.³⁵⁻³⁷ The irreversible capacity rapidly decreases with the increase of the cycle number, and the capacity stabilizes after ca. 10 cycles. On the other hand, the coulombic efficiency in the first cycle for the calcined sample is higher (~94.8%). Both samples exhibit good cycle stability at the current density of 1 C (175 mA/g). From cycle 10 to 200 the capacity decreases from 116 to 110 mAh/g and from 152 to 148 mAh/g for the pristine and calcined samples, respectively.

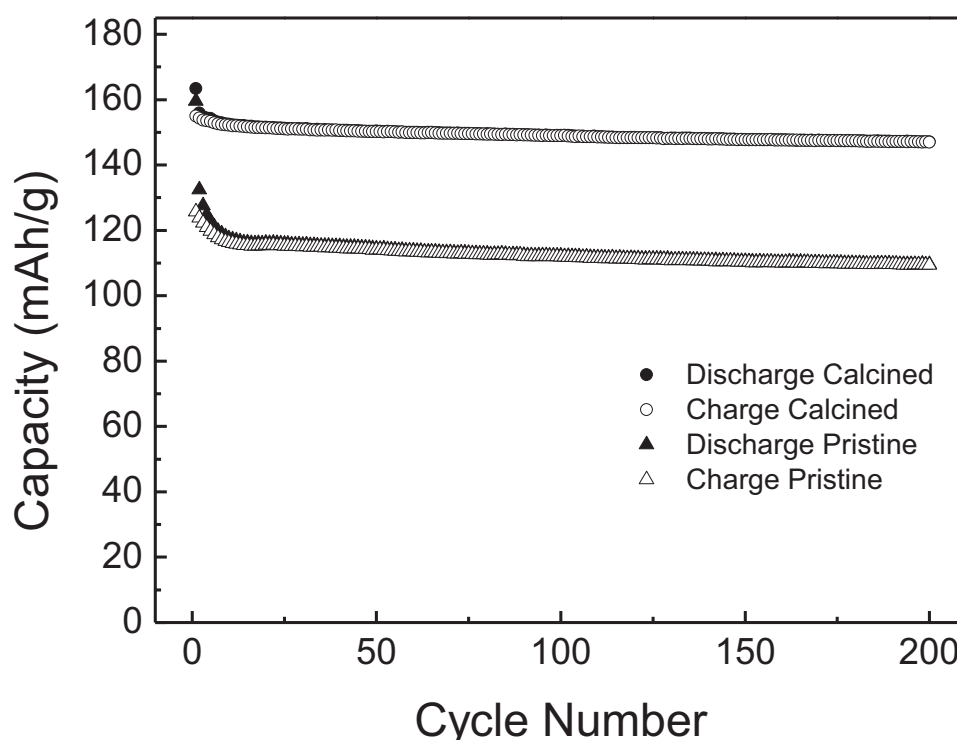


Figure 5.7: Capacity versus cycle number at the current density of 1 C (175 mA/g) for as-synthesized nanocrystalline $\text{Li}_4\text{Ti}_5\text{O}_{12}$ (triangles) and after calcination at 750 °C (circles) for both discharge and charge cycles (full and empty symbols, respectively).

They also show an excellent rate performance (Figure 5.8). The reversible capacity of the as-prepared sample at the very high rate of 20 C is still around 100 mAh/g, corresponding to 85% of the total capacity at 1 C. This can be understood in terms of the nanometric size of the crystallites that leads to an increase of the contact area between the active material and the electrolyte and to a short Li diffusion length.¹ The reversible capacity of the calcined sample decreases more rapidly reaching the same values as for the pristine sample at the high rates of 20 C (~105 mAh/g) and 30 C (~85 mAh/g). This can be attributed to the larger specific surface area of the pristine sample, which gives rise to a higher interface contact between the LTO and the electrolyte. Therefore, the lithium diffusion path is shorter in the pristine sample avoiding polarization effects (*cf.* also Figure 5.6a). Finally, both samples recover the initial reversible capacity at 1 C suggesting that the nanostructure is still preserved after high rate charge/discharge cycles. At the rate of 10 C, 20 C, and 30 C, as-prepared sample showed high-rate performance of 91%, 85%, and 72%, respectively, in comparison to 1 C. These performance rates are comparable to the high-rate performance results from other recent papers.^{27,31} In comparison to other methods, our synthesis method is simpler and creates the smallest primary particles ever reported for LTO.

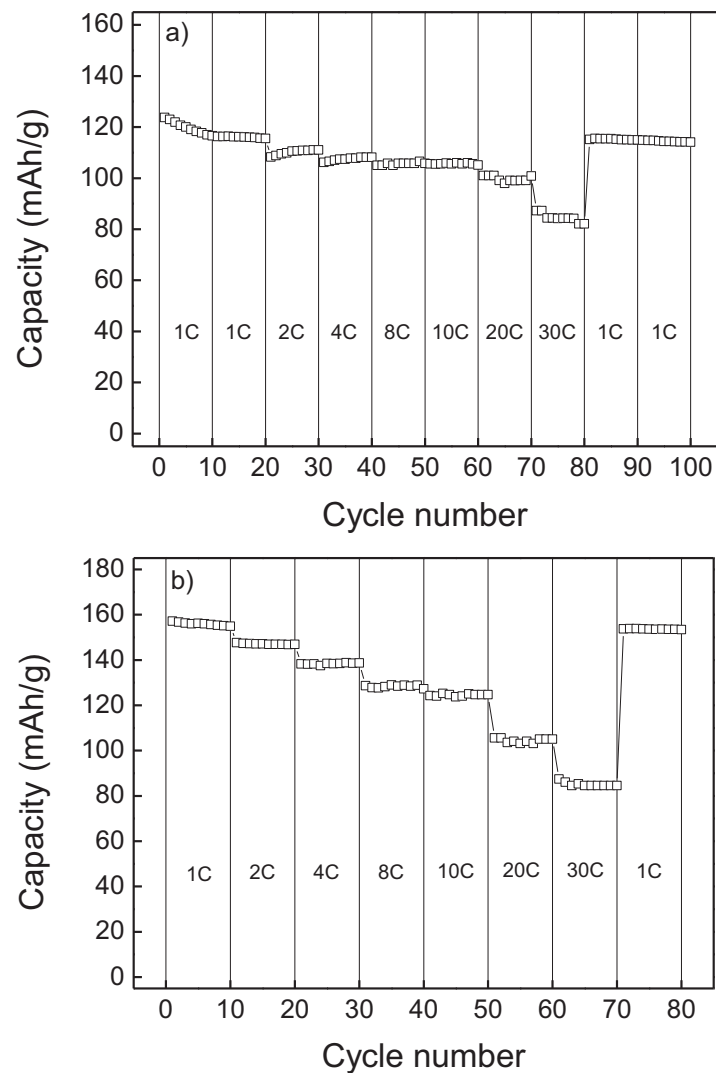


Figure 5.8: Reversible capacity versus cycle number at various current densities for as-synthesized nanocrystalline $\text{Li}_4\text{Ti}_5\text{O}_{12}$ (a) and after calcination at 750 °C (b).

3 Conclusions

In conclusion, nanostructured micrometer-sized hierarchical spinel $\text{Li}_4\text{Ti}_5\text{O}_{12}$ nanostructures were prepared by a simple, surfactant and template-free method based on the “benzyl alcohol route”. This method consists on the solvothermal

Chapter 5 – Lithium Titanium Oxide

treatment of lithium and titanium alkoxide in benzyl alcohol. The as-synthesized material consists of 1-2 μm sized spherical particles made of 10 nm crystalline nanoplatelets. The yield of the reaction is above 85% and allows the production of gram quantities of LTO nanostructures from a 20 ml synthesis. This is the first report of crystalline $\text{Li}_4\text{Ti}_5\text{O}_{12}$ synthesized by solution routes without the need of a post-synthesis calcination step. Furthermore, the as-prepared nanostructures exhibit good capacity and cycle performances even at high charge/discharge rates (30 C) when used as anode material in lithium ion batteries. A post-synthesis annealing process improves the charge/discharge capacity, which approaches the theoretical limit of the spinel $\text{Li}_4\text{Ti}_5\text{O}_{12}$ structure. The high performances in term of cyclability and capacity of this LTO material are comparable to the best one present in the actual state of the art.

4 Bibliography

- (1) Bruce, P.; Scrosati, B.; Tarascon, J.-M. *Angewandte Chemie International Edition* **2008**, *47*, 2930.
- (2) Pinna, N.; Niederberger, M. *Angewandte Chemie International Edition* **2008**, *47*, 5292.
- (3) Mutin, P. H.; Vioux, A. *Chemistry of Materials* **2009**, *21*, 582.
- (4) Niederberger, M. *Accounts of Chemical Research* **2007**, *40*, 793.
- (5) Pinna, N. *Journal of Materials Chemistry* **2007**, *17*, 2769.
- (6) Clavel, G.; Rauwel, E.; Willinger, M.-G.; Pinna, N. *Journal of Materials Chemistry* **2009**, *19*, 454.
- (7) Niederberger, M.; Pinna, N. *Metal Oxide Nanoparticles in Organic Solvents*; Springer London, 2009.
- (8) Pinna, N.; Karmaoui, M.; Willinger, M.-G. *Journal of Sol-Gel Science and Technology* **2011**, *57*, 323.
- (9) Karmaoui, M.; Willinger, M. G.; Mafra, L.; Hertrich, T.; Pinna, N. *Nanoscale* **2009**, *1*, 360.
- (10) Ferg, E.; Gummow, R. J.; de Kock, A.; Thackeray, M. M. *Journal of The Electrochemical Society* **1994**, *141*, L147.
- (11) Amatucci, G. G.; Badway, F.; Pasquier, A. D.; Zheng, T. *Journal of The Electrochemical Society* **2001**, *148*, A930.
- (12) Colbow, K. M.; Dahn, J. R.; Haering, R. R. *Journal of Power Sources* **1989**, *26*, 397.
- (13) Ohzuku, T.; Ueda, A.; Yamamoto, N. *Journal of The Electrochemical Society* **1995**, *142*, 1431.
- (14) Pyun, S.-I.; Kim, S.-W.; Shin, H.-C. *Journal of Power Sources* **1999**, *81-82*, 248.
- (15) Zaghbi, K.; Simoneau, M.; Armand, M.; Gauthier, M. *Journal of Power Sources* **1999**, *81-82*, 300.
- (16) Zaghbi, K.; Armand, M.; Gauthier, M. *Journal of The Electrochemical Society* **1998**, *145*, 3135.
- (17) Hsiao, K.-C.; Liao, S.-C.; Chen, J.-M. *Electrochimica Acta* **2008**, *53*, 7242.
- (18) Aldon, L.; Kubiak, P.; Womes, M.; Jumas, J. C.; Olivier-Fourcade, J.; Tirado, J. L.; Corredor, J. I.; Perez Vicente, C. *Chemistry of Materials* **2004**, *16*, 5721.
- (19) Kavan, L.; Gratzel, M. *Electrochemical and Solid-State Letters* **2002**, *5*, A39.
- (20) Jiang, C.; Ichihara, M.; Honma, I.; Zhou, H. *Electrochimica Acta* **2007**, *52*, 6470.
- (21) Sorensen, E. M.; Barry, S. J.; Jung, H.-K.; Rondinelli, J. M.; Vaughey, J. T.; Poepelmeier, K. R. *Chemistry of Materials* **2006**, *18*, 482.
- (22) Kalbac, M.; Zukalova, M.; Kavan, L. *Journal of Solid State Electrochemistry* **2003**, *8*, 2.

Chapter 5 – Lithium Titanium Oxide

- (23) Kim, D. H.; Ahn, Y. S.; Kim, J. *Electrochemistry Communications* **2005**, *7*, 1340.
- (24) Bach, S.; Pereira-ramos, J. P.; Baffier, N. *Journal of Materials Chemistry* **1998**, *8*, 251.
- (25) He, N.; Wang, B.; Huang, J. *Journal of Solid State Electrochemistry* **2010**, *14*, 1241.
- (26) Jiang, C.; Zhou, Y.; Honma, I.; Kudo, T.; Zhou, H. *Journal of Power Sources* **2007**, *166*, 514.
- (27) Tang, Y.; Yang, L.; Fang, S.; Qiu, Z. *Electrochimica Acta* **2009**, *54*, 6244.
- (28) Lee, S. C.; Lee, S. M.; Lee, J. W.; Lee, J. B.; Lee, S. M.; Han, S. S.; Lee, H. C.; Kim, H. J. *The Journal of Physical Chemistry C* **2009**, *113*, 18420.
- (29) Tang, Y. F.; Yang, L.; Qiu, Z.; Huang, J. S. *Electrochemistry Communications* **2008**, *10*, 1513.
- (30) Tang, Y.; Yang, L.; Qiu, Z.; Huang, J. *Journal of Materials Chemistry* **2009**, *19*, 5980.
- (31) Prakash, A. S.; Manikandan, P.; Ramesha, K.; Sathiya, M.; Tarascon, J. M.; Shukla, A. K. *Chemistry of Materials* **2010**, *22*, 2857.
- (32) Yoshikawa, D.; Kadoma, Y.; Kim, J.-M.; Ui, K.; Kumagai, N.; Kitamura, N.; Idemoto, Y. *Electrochimica Acta* **2010**, *55*, 1872.
- (33) Pinna, N.; Garnweitner, G.; Antonietti, M.; Niederberger, M. *Advanced Materials* **2004**, *16*, 2196.
- (34) Niederberger, M.; Garnweitner, G.; Pinna, N.; Antonietti, M. *J. Am. Chem. Soc.* **2004**, *126*, 9120.
- (35) Lan, Y.; Gao, X. P.; Zhu, H. Y.; Zheng, Z. F.; Yan, T. Y.; Wu, F.; Ringer, S. P.; Song, D. Y. *Advanced Functional Materials* **2005**, *15*, 1310.
- (36) Guo, Y. G.; Hu, Y. S.; Sigle, W.; Maier, J. *Advanced Materials* **2007**, *19*, 2087.
- (37) Ortiz, G. F.; Hanzu, I.; Djenizian, T.; Lavela, P.; Tirado, J. L.; Knauth, P. *Chemistry of Materials* **2008**, *21*, 63.
- (38) Kim, J. K.; Woo, C. H.; Choi, E. S.; Lim, J. S.; Kim, D. H.; Ahn, S. H. High-capacity anode material for lithium secondary batteries and process for synthesizing the same; Hyundai Motor Company Industry foundation of Chonnam National University, 2010; Vol. US 2011/0135564 A1.

CHAPTER 6*
Assembly

*This chapter has never been either submitted nor published at the time of the defense.

Table of contents

1 Introduction 107

2 Results and discussion 109

3 Conclusions..... 122

4 Bibliography 124

1 Introduction

For material scientists, biomineralization offers not only a playground to discover and wonder about beautifully assembled materials, but also to try to mimic them and learn the principles of their formation. During millions of years of evolutionary development and testing, biominerals have evolved in optimized forms under various constraints. A unifying building principle in biominerals is the hierarchical assembly of their building blocks, starting from the basic structural units.¹⁻³

Comparing our achievements in the synthesis of new materials to the products of nature demonstrates that we are just at the beginning of understanding how to design materials with complex and hierarchical structures.

Understanding the formation of materials from their building blocks is essential for the design of hierarchically structured materials. Much work has been devoted to fabrication of nanoparticles with desired properties; however, their assembly into larger structures is still not fully understood and controlled at the molecular level.

Superstructures showing ordered arrangement can be built either by self-assembly directly in solution, or on a substrate following solvent evaporation or sedimentation.⁴⁻

⁶ Colloidal self-assembly, in particular, has attracted special attention because it allows to easily obtain 3D ordered structures.⁷⁻⁸ Nano-building-blocks can spontaneously organize under the effect of externally applied magnetic, electric or flow fields, or by specific interaction such as short range forces.⁹ The large majority of reported approaches fall into the latter category, mainly using substrates, templates, and long aliphatic chain ligands as assembly directing agents.

Since it was first proposed in 1996,¹⁰⁻¹¹ DNA driven self-assembly of metal nanoparticles has been one of the most widely investigated methods allowing the engineering of a large number of crystal structures by controlling the length and interaction of the complementary DNA chains as well as the size and shape of the nanoparticles.¹²⁻¹⁴ Particularly interesting is also the case of liquid crystals which act as templates for a geometrical organization of the nanoparticles inducing anisotropic

interaction.¹⁵⁻¹⁶ All these approaches rely on large and complex ligand molecules. As a consequence, the fraction of organic species in the final material is significant, especially when dealing with small colloids.

Assemblies of nanocrystals stabilized by shorter molecules were also explored. For example, Kahn *et al.* proposed the formation of 2D and 3D arrays of ZnO nanoparticles stabilized by diverse alkyl chains through evaporation of colloidal THF solutions.¹⁷ Better control over dimensionality of the superstructure was achieved by selectively functionalizing either some or all of the faces of silver cubes with a hydrophobic thiolate.¹⁸ However, in many cases the production of superstructured materials is a mere laboratory exercise and robust approaches scalable up to industrial level aimed at commercial applications are still at a research stage.

In the introduction of the manuscript the surfactant-free non-aqueous sol–gel routes were presented as one of the most versatile and powerful methodologies for the synthesis of nanocrystalline metal oxides with high compositional homogeneity and purity.¹⁹ However, one of the drawbacks of these synthesis protocols is the lack of a precise control over the particle size and size distribution, which is attributable to the lack of stabilizing agents in the reaction medium. One notable exception is the solvothermal reaction of zirconium isopropoxide in benzyl alcohol leading to the formation of uniform zirconia nanocrystals.

The synthesis presented in Chapter 3 was modified by increasing the reaction temperature above 230 °C and by using Tb and Y as dopants (*cf.* Table 2.1 in Chapter 2). This simple synthetic protocol leads to the formation of benzoate capped monodisperse zirconia nanocrystals that self-assemble into large superlattices. In the present chapter it is shown that the main weakness of the surfactant-free non-aqueous routes can be overcome by the *in situ* formation of benzoate species acting as stabilizing and structure-directing agents. The morphology and structure of the superlattice is studied as a function of the amount of the benzoate species, formed from the oxidation of the solvent, and as a function of nanoparticle doping. To the best of our knowledge, there have been no previous reports of surfactant-free syntheses of nanocrystals coupled with *in situ* assembly into a 3D superlattice.

2 Results and discussion

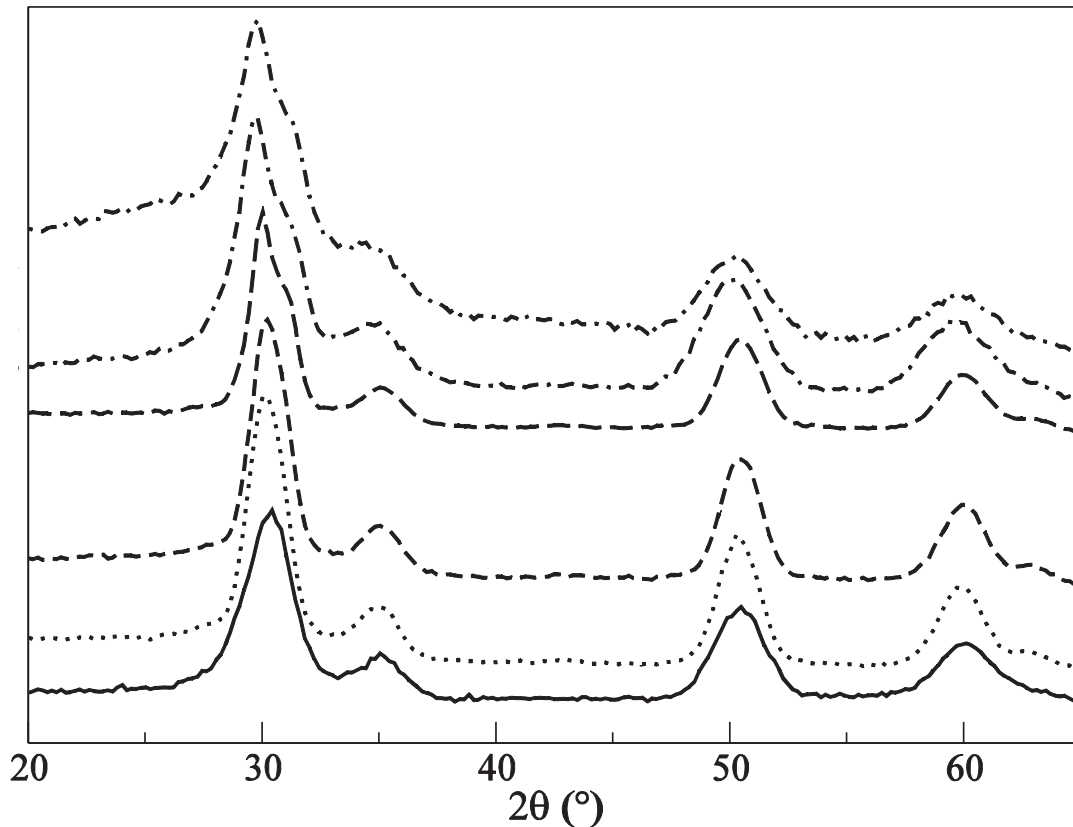


Figure 6.1: XRD patterns of the samples presented in this chapter. Pure ZrO_2 synthesized at 230 °C (full line), 325 °C (dotted line), 350 °C (dashed line), 6%Y-doped zirconia synthesized at 350 °C (long dashed line), 10%Tb-doped zirconia synthesized at 300 °C (dash-dash-dot), 325 °C (dash-dot).

X-ray diffraction patterns of the as-synthesized pure zirconia particles are displayed in Figure 6.1. They show broad diffraction peaks due to the nanometric size of the crystals. An average particle size around 4 nm, as deduced by the Scherrer formula, is obtained for the pure zirconia particles independently of the reaction temperature (*cf.* Table 6.1). As the diffraction peaks are broad, XRD experiments are not suitable to assign univocally the crystalline structure of the nanoparticles. Indeed, as above mentioned, lattice parameters of the cubic (JCPDS [27–997]) and tetragonal phase (JCPDS [17–923]) of zirconia are similar, and the splitting of X-ray reflections due to tetragonal symmetry breaking is beyond visual resolution. However, on the basis of Rietveld refinement, it was possible to conclude that the synthetic procedure for pure

zirconia leads to the cubic phase.²⁰ However, the addition of dopant may stabilize the tetragonal modification, as suggested from preliminary Raman results obtained for Y-doped ZrO_2 . The yttrium doped samples contain particles of similar size, whereas the terbium doped nanoparticles are slightly smaller (*cf.* Figure 6.1 and Table 6.1).

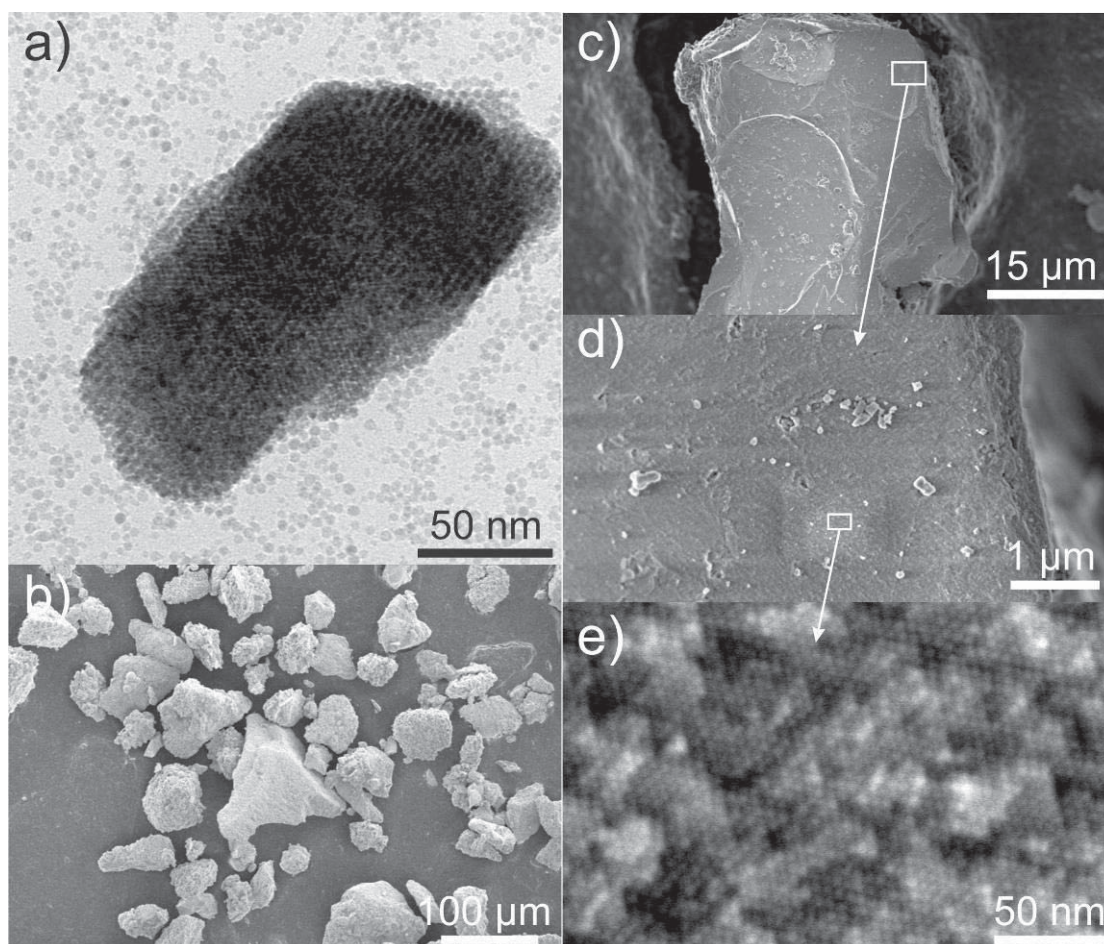


Figure 6.2: (a) TEM image of a small aggregate of ZrO_2 nanoparticles synthesized at 230 °C. (b-e) SEM images recorded at different magnifications on large aggregates of ZrO_2 nanoparticles synthesized at 325 °C.

Transmission electron microscopy (TEM) studies of the standard sample synthesized at 230 °C principally show isolated nanoparticles, but also some aggregates such as the one in Figure 6.2a. They are composed of monodisperse particles of about 4 nm periodically assembled, *i.e.* the same size as isolated nanoparticles. This first observation was a motivation to investigate the factors controlling the assembly

behavior of zirconia nanoparticles. The increase in reaction temperature did not dramatically affect either the zirconia particle size or their size distribution. On the other hand, large agglomerates of several tens of micrometers were now present as shown by the scanning electron microscopy (SEM) images (Figure 6.2b and c). Zooming in on one of these aggregates reveals that they are composed of 4 nm zirconia nanoparticles assembled in ordered structures (Figure 6.2d and e). Therefore, a simple increase in reaction temperature has the effect of promoting nanoparticle assembly into large superstructures without affecting the nanocrystals size.

In Chapter 4 the doping of zirconia was extended to yttrium and terbium ions investigating purity and doping efficiency. This chapter focuses on the role of the doping on the assembly of zirconia nanoparticles. The fabrication of terbium doped zirconia should take place at higher temperatures compared to pure zirconia. As a matter of fact, at temperatures lower than 300 °C the yield of the reaction was lower than 30%. At 300 °C monodisperse nanoparticles forming large ill-defined aggregates could be obtained (Figure 6.3a). It turned out that these aggregates are composed of monodisperse terbium doped zirconia nanoparticles assembled in well ordered superlattices. Figure 6.3b shows the edge of a supercrystal containing several layers of hexagonally assembled nanoparticles. The Fourier transform shows several sets of reflections (Figure 6.3b inset). The particles show a poorly marked preferential crystallographic orientation leading to relatively broad reflections. The two outer sets can be attributed to the cubic zirconia structure in [110] zone axis. The presence of six reflections due to the 220 lattice planes suggests that the nanocrystals can rotate 60° around the [110] axis. Close to the center, the two sets of spots are characteristic of the 2D hexagonal packing of the nanoparticles.

At higher temperatures (*i.e.* 325 and 350 °C) the synthesis produces aggregates with well faceted shapes such as flower-like, rhombic dodecahedron and bipyramids, depending on the temperature and dopant used. At 325 °C the terbium doped particles mainly show a flower-like morphology (Figure 6.3d). SEM images of isolated aggregates highlight the complex morphology and growth pattern (Figure 6.3e and f).

The overview TEM image (Figure 6.3g) shows the facets and the complexity of the leaves. The 3 pairs of reflections present in the selected area electron diffraction (Figure 6.3h) are characteristic of the cubic zirconia in [110] orientation. Here again the nanocrystals exhibit a preferential crystallographic orientation. The higher resolution image of the same edge of the aggregate, from which the SAED was recorded, shows the nano-building blocks forming an ordered superlattice (Figure 6.3i). Increasing the reaction temperature to 350 °C results in rhombic dodecahedron mesocrystals, in addition to flower-like morphologies, such as the ones depicted in Figure 6.3j. The yttrium doped sample synthesized under the same conditions shows bipyramid mesocrystals (Figure 6.3k). The HRSEM images of the surface of the well faceted aggregates always show a highly ordered assembly of the nano-building blocks (*cf.* Figure 3l).

It is important to point out that irrespective of the synthesis temperature and the doping the resulting nanoparticles have similar size (*cf.* Table 6.1) and very low size dispersion. Combined with the fact that the nano-building blocks are not completely fused and are therefore still discernible, these unique features allow us to study the formation mechanism of these mesocrystals.

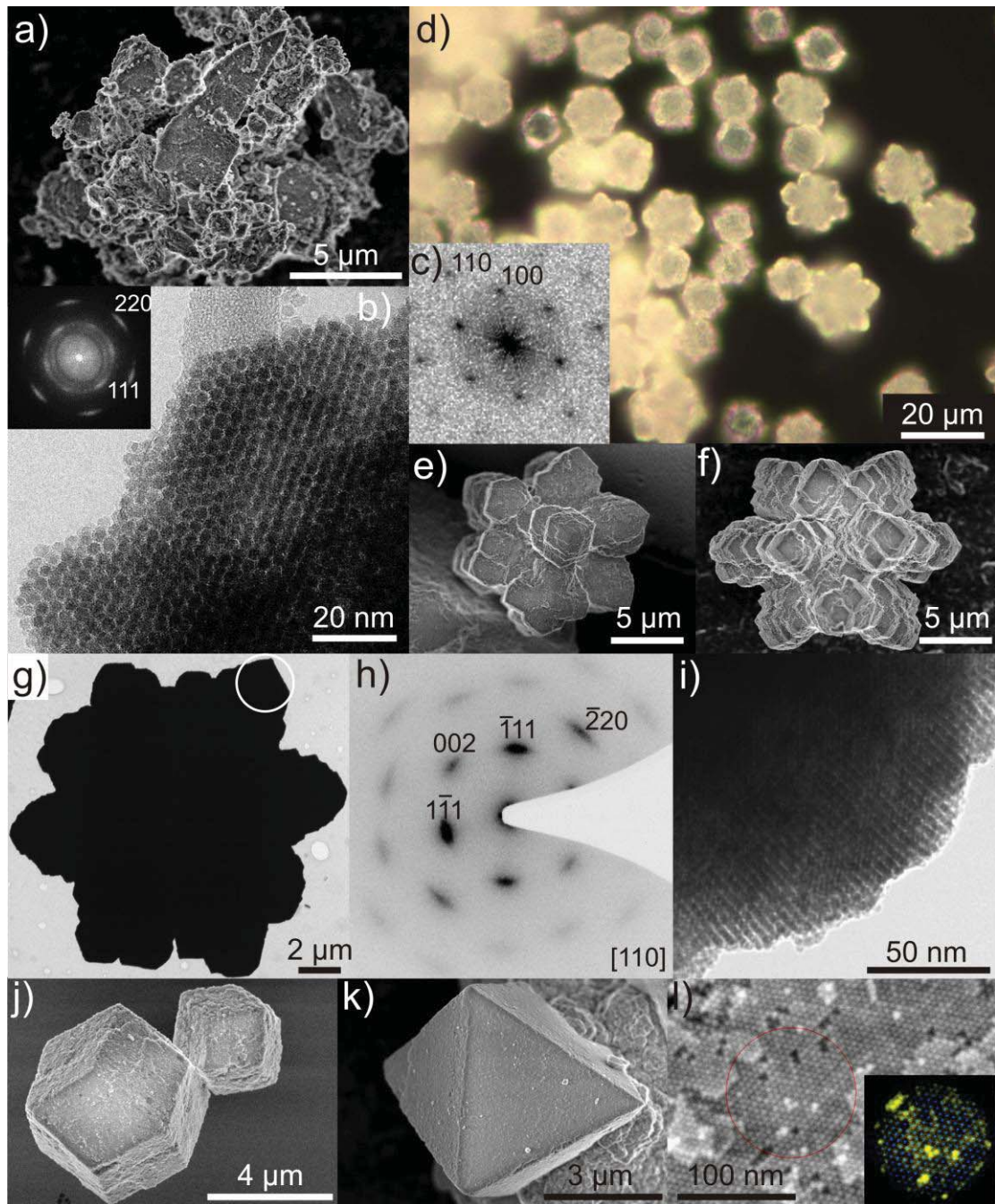


Figure 6.3: (a) SEM and (b) TEM images of supercrystals of 10% Tb-doped zirconia synthesized at 300 °C from which the SAED (c) was taken. (d) Optical microscopy, (e,f) SEM and (g,i) TEM images of supercrystals of 10% Tb-doped zirconia synthesized at 325 °C (h) selected area electron diffraction of the region indicated by a circle. (j) SEM of rhombic dodecahedra supercrystals of 10% Tb-doped zirconia synthesized at 350 °C. (k) SEM of bipyramidal supercrystal of 6% Y-doped zirconia synthesized at 350 °C. (l) HRSEM of the surface of an aggregate showing the assembly of the building blocks (inset color coded image showing a different nanoparticle layers).

Since transmission and scanning electron microscopy are not the best techniques for the assessment of the nanoparticles packing and because the synthesis approach readily produces gram quantity of material, the nanoparticle assembly was studied by small angle x-ray scattering (SAXS). The unusual packing of the nanoparticles is manifested in the relatively sharp x-ray diffraction peaks observed in the small angle region.

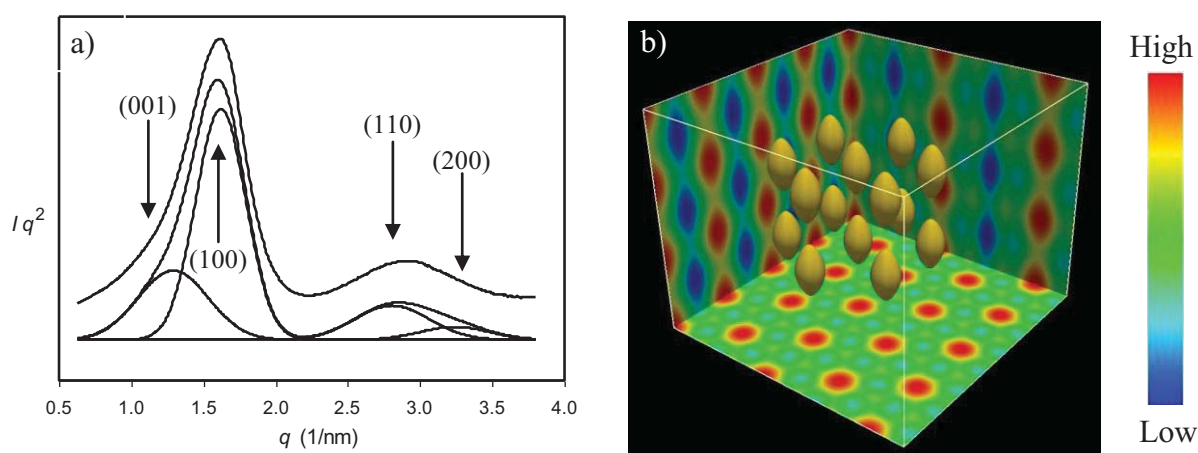


Figure 6.4: (a) SAXS diffractogram (best-fit curve and resolved diffraction peaks are plotted below) of pure Zirconia synthesized at 230 °C and (b) relative reconstructed electron density map. The three 2D maps lining the walls are [100], [110] and [001] cuts.

The packing of the zirconia nanoparticles strongly depends on temperature. In Figure 6.4a the Lorentz corrected diffraction intensity related to low temperature synthesis is depicted as a function of scattering vector q ($q = 4\pi\sin 2\theta/\lambda$, here 2θ is the scattering angle). Four diffraction peaks are observed and their index suggested a 3D simple hexagonal lattice with space group $P6/mmm$. The reconstructed electron density map (Figure 6.4b) shows that the nanoparticles are centered at the corners of the hexagonal unit cell. The cell parameters are $a = 4.48$ nm (the distance between nanoparticles within the 001 hexagonal plane) and $c = 4.87$ nm (distance between particles within a column, normal to the hexagonal plane). The iso-electron surface enclosing the high density region (*i.e.* the core of the nanoparticles) shows disproportionately large elongation along the c -axis, suggesting poor correlation along the column.

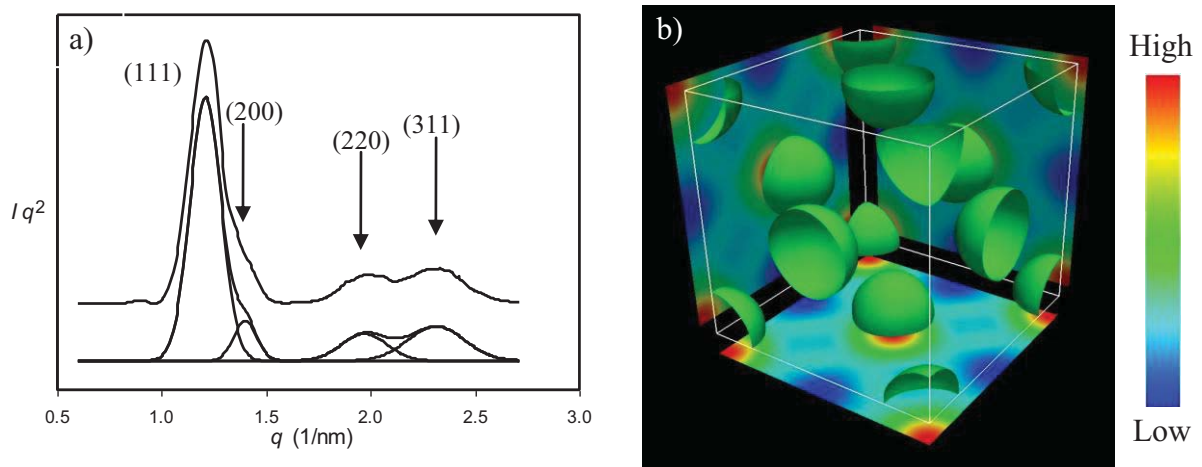


Figure 6.5: (a) SAXS diffractogram (best-fit curve and resolved diffraction peaks are plotted below) of pure Zirconia synthesized at 325 °C and (b) relative reconstructed electron density map. Green iso-electron surfaces showing nanoparticles pack on an FCC lattice. The three 2D maps are [100], [010] and [001] cuts at the unit cell surfaces, slightly shifted for better view.

By increasing the reaction temperature the packing changes. The pure samples synthesized at 325 °C presented a face centered cubic lattice (FCC) with space group symmetry $Fm\bar{3}m$ (Figure 6.5). The intensities of the first four diffraction peaks were used to reconstruct the electron density map of the phase. As shown in Figure 6.5b, the nanoparticles occupy the corners and face centers in the cubic lattice. There are four nanoparticles in the unit cell, and the nearest neighbor distance is 6.36 nm. A further increase in temperature led to a rhombohedral lattice with space group $R\bar{3}m$. Similar packing was observed for the high temperature synthesis of doped nanoparticles. Indeed, the SAXS diffraction pattern of Tb-doped ZrO_2 nanoparticles synthesized at 325 °C (Figure 6.6a) can also be indexed on a rhombohedral lattice with space group $R\bar{3}m$ and lattice parameters $a = 7.11$ nm, $c = 3.78$ nm (hexagonal coordinates). The reconstructed electron density map shows that ZrO_2 nanoparticles form linear chains. The distance between nanoparticles in each chain is $c = 3.78$ nm.

Chapter 6 – Assembly

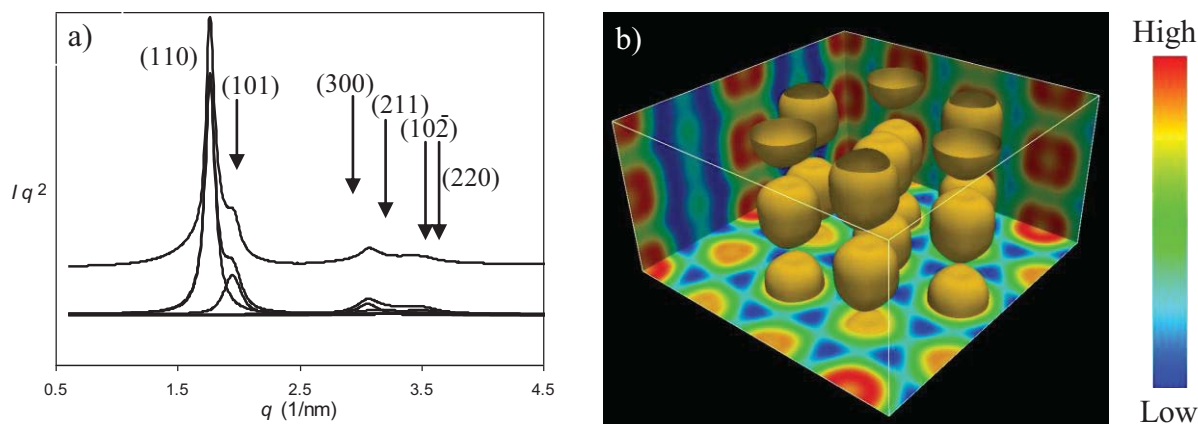


Figure 6.6: (a) SAXS diffractogram (best-fit curve and resolved diffraction peaks are plotted below) of 10% Tb-doped Zirconia synthesized at 325 °C and (b) relative reconstructed electron density map. Yellow iso-electron surface enclose the high density core of the nanoparticles. The three 2D maps lining the walls are [100], [110] and [001] cuts.

The nanoparticle columns pack on a hexagonal lattice, with the columns shifted longitudinally by $c/3 = 1.26$ nm relative to the neighboring columns. Consequently each unit cell contains 3 chains with relative heights 0, 1.26 and 2.52 nm, respectively. In contrast to the simple hexagonal packing of low temperature synthesized nanoparticles, here the distance between nanoparticles in neighboring chains is larger than within the same chain (4.29 nm instead of 3.78 nm; see Table 6.1). This rhombohedral structure can in fact be viewed as a FCC structure compressed along its [111] axis. The order of this phase is very good, judging by the FWHM of the (110) diffraction peak; the domain size is ~ 63 nm.

Table 6.1. Composition, reaction temperature, carbon content, nanoparticle sizes extracted from XRD (Scherrer formula applied to the 220 reflection) and ordered packing as determined by SAXS of the sample discussed in this study.

Sample Name	Composition	Reaction Temperature (°C)	Carbon Content (weight%) ^a	Particle size (nm) ^b	packing	Particle distance (nm)	
						between columns	within column
AP227E	ZrO ₂	230	4.4	3.7	<i>P6/mmm</i>	4.48	4.87
AP256	ZrO ₂	325	10.5	4.4	<i>Fm3m</i>	6.36	6.36
AP275	ZrO ₂	350	-	4.4	<i>R3m</i>	6.92	5.71
VR91	ZrO ₂ :Tb	300	14.8	3.0	<i>P6/mmm</i>	4.06	4.16
AP257	ZrO ₂ :Tb	325	15.0	3.1	<i>R3m</i>	4.29	3.78
AP272	ZrO ₂ :Y	350	11.1	4.3	<i>R3m</i>	5.91	4.89

^aDeduced from CHN analysis. ^bCrystallite size estimated from XRD patterns using the Scherrer equation and considering the diffraction peak at $2\theta = 50^\circ$ (*i.e.* 220). It is in good agreement with the particle size extracted from TEM measurements suggesting the single crystal nature of the nanoparticles (*cf.* also HRTEM measurements).

High resolution TEM of an edge of a supercrystal gives additional information on nanoparticle packing. In Figure 6.7a several layers of particles were imaged in high resolution. The slight difference in contrast makes it possible to distinguish the edges and the shape of the individual nano-building blocks. The particles are well-faceted showing semi-regular hexagonal projections. Each nanocrystal shows well-defined lattice fringes. The power spectrum of the whole image (Figure 6.7b) consists of diffuse spots, the distance and the angle between them being characteristic of the cubic ZrO₂ structure imaged along the [110] zone axis. This indicates that the facets defining the particle projection along [110] are two {100} and four {111}. Such a morphology under a TEM typifies cuboctahedron-shaped particles, having only {100} and {111} facets (Figure 6.7c).

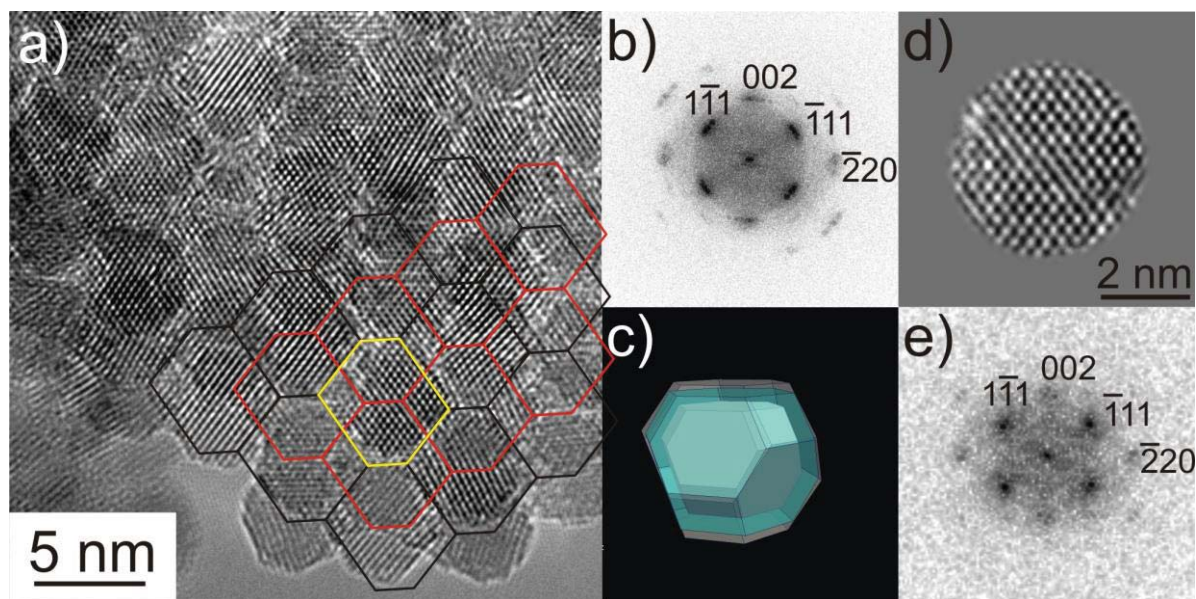


Figure 6.7: (a) HRTEM image and the (b) corresponding power spectrum of an edge of a superlattice made of 6% Y-doped zirconia synthesized at 350 °C. (c) Three Voronoi polyhedra. The outer one (gray) is the cubooctahedron of the BCC lattice. The middle (blue) is the one that tessellates the observed $R3m$ lattice before annealing. Obvious is the shrinkage of the $R3m$ along z-axis. Its (110) projection is used to form the outlines of the two layers (black and red lines) of polyhedra in (a). The inner Voronoi is for the lattice shrunk on annealing at maximum T before loss of order. (d) HRTEM selection used for the power spectrum shown in (e), the region correspond to the particles highlighted by the yellow contour in (a).

In order to better understand the factors controlling the nanoparticle assembly, additional characterization was carried out. First of all, it is known that superlattices are generally formed by interactions between the ligands adsorbed at the surface of the nanoparticles. Although no surfactants were used in the present synthesis, a careful investigation of the organic species left at the surface of the zirconia nanoparticles was carried out by ^{13}C solid state NMR and FT-IR spectroscopy. In all the cases, carbon contamination was observed. More surprisingly, it was found that the only organic species detected are benzoates. Indeed, the SS-NMR spectra of pure zirconia samples (Figure 6.8a) shows interesting feature only in the range of spectra between 100 and 200 ppm. More in details, it displays a broad band between 121 and 137 ppm, a small peak centered at 140 ppm and a peak at lower field centered at 173 ppm. In general, the spectrum recorded on the sample synthesized at higher temperature (full line), carrying a higher amount of organics, is better resolved.

Considering the kind of organics playing a role in the reaction (benzyl alcohol as solvent and isopropyl moieties of the zirconium precursor) the pattern can be easily traced back to benzoate groups matching well potassium benzoate salt reported in literature. *In situ* formed benzoate species coming from the oxidation of benzyl alcohol used as solvent for the metal oxide synthesis have been observed previously.²⁴ They are usually formed at relatively high temperatures and can be catalyzed by metal centers. A peculiar example is the formation of rare-earth oxide-based lamellar organic-inorganic nanostructures under similar reaction conditions.²⁵⁻²⁶ It was found that benzoate species were the only organic moieties present between the inorganic RE₂O₃ layers, separating them by 1.2 nm. They form a bridge-like interlayer bond, and are thus responsible for the formation of the periodic organic-inorganic structure. From chemical analysis the concentration of organic “contamination” increases with the reaction temperature and the doping. The carbon content estimated from elemental and thermogravimetric analysis was less than 5 weight% for the standard synthesis of ZrO₂ nanoparticles at 230 °C and it increased up to 15% for the nanoparticles synthesized above 300 °C (*cf.* Table 6.1).

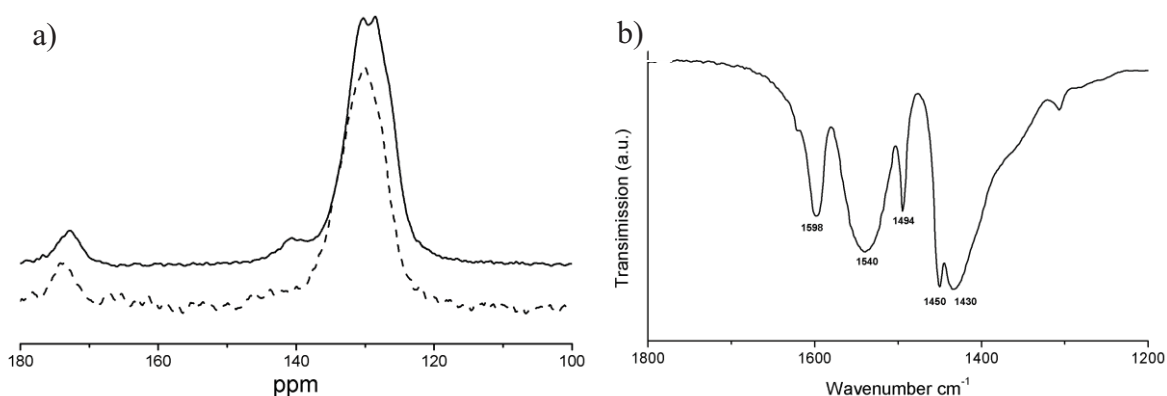


Figure 6.8: a) ¹³C Solid State NMR spectra of pure zirconia nanoparticles synthesized at 230 °C (dashed line) and 300 °C (full line); b) FT-IR spectrum of pure zirconia nanoparticles synthesized at 300 °C.

Figure 6.8b shows the normalized FTIR spectrum of the pure zirconia nanoparticles synthesized at 300 °C. The plot is in good agreement with the spectra showed in the

case of previously reported benzoate-metal oxide systems.^{24,27} In particular, Dobson and McQuillan proposed a very similar pattern for benzoic acid adsorbed on ZrO₂ film.²⁸ The peaks at 1598, 1494 and 1450 cm⁻¹ can be assigned to the stretching modes of phenyl rings. The doublet at 1540 and 1430 cm⁻¹ is assigned to the asymmetric and the symmetric stretching of the carboxylate group, respectively. It is well known that the relative position of the two broad bands can be related to the geometry of the carboxyl-metal centre coordination. A difference of 110 cm⁻¹ between the frequencies of the asymmetric and the symmetric stretching of the carboxylate group suggests the presence of chelating bidentate bonds between benzoate and zirconium ions. It should also be pointed out that the mother liquor after nanoparticle formation does not contain any benzoic acid (data not shown), proving that benzoate species are formed at the surface of the nanoparticles, staying adsorbed and immediately stopping their growth. The low polydispersity of the ZrO₂ nanoparticles, compared to similar surfactant-free non-aqueous sol-gel routes, supports this mechanism. These findings suggest that the formation of the zirconia superlattices can also be attributed to the surface benzoate species, where π - π stacking between phenyl groups keep together the structure and directs the assembly. Generally, the primary particle size extracted from XRD linewidths and TEM measurements are in good agreement, pointing to a single crystal characteristic of the particles as also previously demonstrated.²¹⁻²³ On the other hand, the particle-particle distance determined from SAXS experiments is always larger than the particle size (*cf.* Table 6.1). This implies that organic species acting as a glue are intercalated in the superlattice and participate in the assembly.

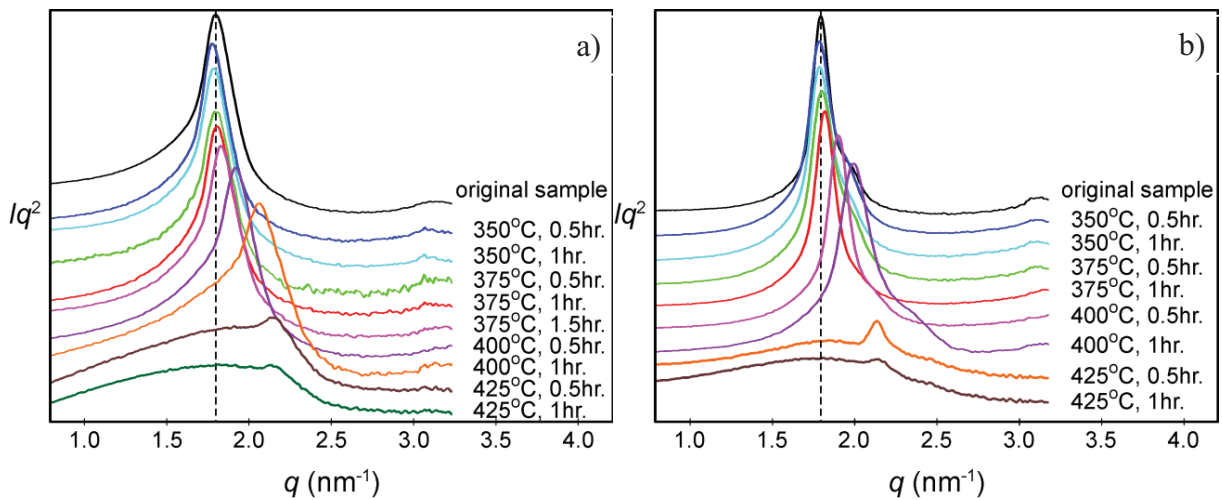


Figure 6.9: SAXS diffractograms of 10% Tb-doped Zirconia synthesized at 325 °C (a) and at 325 °C (b) as a function of the annealing temperature.

In order to confirm the above hypothesis mild annealing experiments were carried out in order to remove the organic species while preserving the order. At the same time, the assembly and lattice contraction was monitored by SAXS (Figure 6.9). Annealing at 400 °C for one hour led to a weight loss of 18% and a contraction of the lattice parameters larger than 20% for the 10% Tb-doped nanoparticles synthesized at 300 °C. The parameters of the hexagonal lattice contracted slightly anisotropically from $a = 4.01$ and $c = 4.09$ nm to $a = 3.49$, $c = 3.58$ nm, respectively, *i.e.* by 13.0% and 12.5% along a and c , respectively. It should also be pointed out that the structure of the superlattice was not affected by thermal treatment up to 400 °C. After annealing at 425 °C, only broad and very weak diffraction was observed, meaning that ordered structure has been destroyed. Similar results were obtained for the 10% Tb-doped nanoparticles synthesized at 325 °C. In the latter case, the $R3m$ structure and the order were retained for annealing up to 400 °C and the lattice parameters decreased from $a = 7.01$ nm and $c = 3.80$ nm to $a = 6.30$ nm and $c = 3.17$ nm, *i.e.* by 10.1% and 16.6% along a and c , respectively. Increasing the annealing temperature to 425 °C led to a further steep contraction of the lattice to $a = 5.85$ nm and $c = 2.97$ nm, as well as to a rapid reduction and finally loss of order. Therefore, these experiments proved that the supercrystals are formed due to organic ligands stabilizing the nanocrystals,

which are eliminated upon annealing accompanied by the contraction of the lattice and eventually the loss of long range order.

After the assessment of the mechanism leading to the regular assembly of the nanoparticles, the factors governing the assembly towards one structure or another have to be discussed. Both the reaction temperature and doping affect particle size, benzoate formation and packing. Generally, increasing the temperature leads to a slightly larger particle size (*cf.* Table 6.1). Moreover, the quantity of benzoate species increases with the reaction temperature and with the doping. The latter can be attributed to the catalytic effect of the lanthanide on the oxidation of benzyl alcohol to benzoate species as already demonstrated in previous reports.²⁴⁻²⁶

The main question now arising is how cuboctahedron-shaped particles can pack in such exotic structures and why the particle size and packing mode depend on temperature and doping in the observed way. Although this is difficult to prove with the techniques at our disposal, we suggest that the different amount of benzoate species induce different π - π stacking which influence the superlattice structure. As a matter of fact, a low amount (*e.g.* below 5 weight%) of benzoate does not allow the formation of large ordered aggregates, such as for particles synthesized at 230 °C. On the other hand, as the benzoate concentration increases the hexagonal first and then the rhombohedral structure are stabilized. Similar superlattices were also observed on doped HfO₂ nanoparticles and other system are now under investigation.

3 Conclusions

Compared to previous works reported on self-assembly of nanoparticles our system is unique in that the superlattice is formed directly in the reaction medium where the nanoparticles are formed. This is in contrast to the generally used strategy where superlattices are formed by slow evaporation of the solvent from a stable colloidal suspension of ligand-capped particles. The lack of colloidal stabilization of the benzoate capped nanoparticles in benzyl alcohol promotes the formation of stable

superlattices in solution by π - π interaction between the *in situ* formed benzoate ligands attached to neighboring particles. The as-fabricated supercrystals are larger than 10 μm and present well defined 3D morphologies such as flower like, rhombic dodecahedron and bipyramids tunable varying reaction temperature and doping concentration.

Using this strategy it was possible to easily produce gram quantity of highly hierarchically structured superlattices. The 3-4 nm building-blocks, showing similar size and monodispersity irrespective of the reaction parameters, could be assembled in lattices that are normally not achievable for nanoparticles derivatized with common surfactants. Moreover, being the nanocrystals not completely fused and still discernible, it is possible to study in details the formation mechanism of these mesocrystals. Therefore, this system can be understood as a model system for the non-classical crystallization mechanisms and biomaterials formation.

Finally, due to the versatility of the synthetic approach similar assembly might be obtained with other metal oxides.

4 Bibliography

- (1) Song, R.-Q.; Cölfen, H. *Adv. Mater.* **2009**, *22*, 1301.
- (2) Cölfen, H.; Antonietti, M. *Angew. Chem., Int. Ed.* **2005**, *44*, 5576.
- (3) Cölfen, H.; Mann, S. *Angew. Chem., Int. Ed.* **2003**, *42*, 2350.
- (4) Henzie, J.; Grunwald, M.; Widmer-Cooper, A.; Geissler, P. L.; Yang, P. *Nat Mater* **2011**, *advance online publication*.
- (5) Miszta, K.; de Graaf, J.; Bertoni, G.; Dorfs, D.; Brescia, R.; Marras, S.; Ceseracciu, L.; Cingolani, R.; van Roij, R.; Dijkstra, M.; Manna, L. *Nat Mater* **2011**, *10*, 872.
- (6) Tanaka, A.; Kamikubo, H.; Kataoka, M.; Hasegawa, Y.; Kawai, T. *Langmuir* **2011**, *27*, 104.
- (7) Baranov, D.; Manna, L.; Kanaras, A. G. *J. Mater. Chem.* **2011**, *21*, 16694.
- (8) Grzelczak, M.; Vermant, J.; Furst, E. M.; Liz-Marzan, L. M. *ACS Nano* **2010**, *4*, 3591.
- (9) Li, F.; Josephson, D. P.; Stein, A. *Angew. Chem., Int. Ed.* **2011**, *50*, 360.
- (10) Mirkin, C. A.; Letsinger, R. L.; Mucic, R. C.; Storhoff, J. J. *Nature* **1996**, *382*, 607.
- (11) Alivisatos, A. P.; Johnsson, K. P.; Peng, X.; Wilson, T. E.; Loweth, C. J.; Bruchez, M. P.; Schultz, P. G. *Nature* **1996**, *382*, 609.
- (12) Macfarlane, R. J.; Lee, B.; Jones, M. R.; Harris, N.; Schatz, G. C.; Mirkin, C. A. *Science* **2011**, *334*, 204.
- (13) Knorowski, C.; Travasset, A. *Curr. Opin. Solid State Mat. Sci.* **2011**, *15*, 262.
- (14) Cheng, W. L.; Tan, S. J.; Campolongo, M. J.; Hartman, M. R.; Kahn, J. S.; Luo, D. In *Comprehensive Nanoscience and Technology*; Andrews, Scholes, Wiederrecht, Eds.; Academic Press: Amsterdam, 2010, p 69.
- (15) Nelson, D. R. *Nano Letters* **2002**, *2*, 1125.
- (16) Zeng, X.; Liu, F.; Fowler, A. G.; Ungar, G.; Cseh, L.; Mehl, G. H.; Macdonald, J. E. *Adv. Mater.* **2009**, *21*, 1746.
- (17) Kahn, M. L.; Monge, M.; Snoeck, E.; Maisonnat, A.; Chaudret, B. *Small* **2005**, *1*, 221.
- (18) Rycenga, M.; McLellan, J. M.; Xia, Y. *Adv. Mater.* **2008**, *20*, 2416.
- (19) Pinna, N.; Niederberger, M. *Angew. Chem., Int. Ed.* **2008**, *47*, 5292.
- (20) Garnweitner, G.; Goldenberg, L. M.; Sakhno, O. V.; Antonietti, M.; Niederberger, M.; Stumpe, J. *Small* **2007**, *3*, 1626.
- (21) Clavel, G.; Willinger, M.-G.; Zitoun, D.; Pinna, N. *Eur. J. Inorg. Chem.* **2008**, 863.
- (22) Ninjbadgar, T.; Garnweitner, G.; Börger, A.; Goldenberg, L., M.; Sakhno, O.; Stumpe, J. *Adv. Funct. Mater.* **2009**, *19*, 1819.
- (23) Pucci, A.; Clavel, G.; Willinger, M.-G.; Zitoun, D.; Pinna, N. *J. Phys. Chem. C* **2009**, *113*, 12048.
- (24) Pinna, N.; Garnweitner, G.; Beato, P.; Niederberger, M.; Antonietti, M. *Small* **2005**, *1*, 112.

- (25) Karmaoui, M.; Sá Ferreira, R. A.; Carlos, L. D.; Pinna, N. *Mater. Sci. Eng. C* **2007**, *27*, 1368.
- (26) Karmaoui, M.; Sa Ferreira, R. A.; Mane, A. T.; Carlos, L. D.; Pinna, N. *Chem. Mater.* **2006**, *18*, 4493.
- (27) Tunesi, S.; Anderson, M. A. *Langmuir* **1992**, *8*, 487.
- (28) Dobson, K. D.; McQuillan, A. J. *Spectrochimica Acta Part A: Molecular and Biomolecular Spectroscopy* **2000**, *56*, 557.

CHAPTER 7
Conclusions

Conclusions

The development of advanced materials demands for a rational synthesis through well understood protocols, which allow controlling size, homogeneity and assembly behaviors of the desired product. In spite of the recent progress in nanomaterials chemistry research, it is not yet possible to prepare a certain compound on the nanoscale with a desired composition, structure, size and morphology, intentionally and in a predicted way. One of the reasons is the fact that it is not yet possible to predict the reactivity of metal complexes in a particular solvent.

This thesis is focused on the development of doped metal oxide nanostructures by nonaqueous sol-gel chemistry, under solvothermal conditions. Particular emphasis was put on highlighting one of the most promising advantages of these chemical routes. That is, the possibility to easier match the reactivity of the metal complexes compared to aqueous systems. This feature was exploited with a twofold aim: On the one hand, complex materials with high expectation in technological application were fabricated. On the other hand, important advances on the understanding of the process were achieved.

In the first part of the thesis high doping efficiency in the synthesis of transition metal doped ZrO_2 and HfO_2 by tuning the reactivity of the molecular precursors under non-aqueous sol-gel conditions in benzyl alcohol was reported. The largest effective doping concentration was obtained for HfO_2 from $Mn(acac)_3$ (17% Mn). The investigation was extended to Ba-based perovskites for which, however, a certain amount of impurities were found in any case. A combination of several characterization techniques was used in order to correlate the synthesis conditions to the doping efficiency and behavior, and to the magnetic properties of the as synthesized nanocrystals. Post-synthetic annealing treatments under controlled atmospheres were also performed in order to control the oxidation state of the transition metal ions and the amount of oxygen vacancies. It turned out that this is a rather delicate step as it can induce segregation and clustering at relatively low temperature (*i.e.* above 600-700 °C), as well as phase transformations. It can be

concluded that the annealing has to be performed below 650 °C to preserve the nanocrystals size and the crystallographic structure. Magnetic measurements revealed a paramagnetic state for ZrO₂ and HfO₂ doped samples for all studied transition metal contents. On the other hand, a ferromagnetic phase below 43 K for annealed Cr-doped ZrO₂, attributed to the intrinsic DMS behavior, was observed.

These studies paved the way to a further investigation on zirconia doped systems. Several RE-doped ZrO₂ were prepared with loading of doping precursor higher than 15%. In no cases second phases or segregation were encountered making this material appealing for several technological applications (*e.g.* optical, biological or electrochemical devices). As a case study, the investigation of 8% solid solution of Y₂O₃/ZrO₂ as electrolyte for fuel cell application is described. The material demonstrated enhanced sinterability leading to highly dense ceramics upon relatively low heat treatment.

All in all, the ternary systems preparation demonstrated to be very robust while the doping of perovskites turned out to be rather difficult with formation of second phases. Similar situation was found for Lithium-Titanium-Oxide compounds. The solvothermal treatment of lithium and titanium alkoxide in benzyl alcohol led to nanostructured micrometer-sized hierarchical Li₄Ti₅O₁₂ in which, unfortunately, a small amount of a secondary phase (either TiO₂ or Li₂TiO₃ depending on the initial precursor ratio) was always present. However, this compound, reported crystalline for the first time in a soft-chemistry synthesis, exhibited good capacity and cycle performances even at high charge/discharge rate (30 C) when used as anode material in lithium ion batteries. A post-synthesis annealing process improved the charge/discharge capacity approaching the theoretical limit of the spinel Li₄Ti₅O₁₂ structure.

In the final part of the manuscript the assembly of the nanoparticles in disordered or organized superstructures was discussed. At low reaction temperature nanoparticles tend to organize in densely packed aggregates. An increase in reaction temperature had the effect of promoting nanoparticles assembly into large ordered superstructures without affecting the nanocrystals size. Indeed, the modification of certain reaction parameters (*i.e.* temperature and doping concentration) permitted the preparation of

Conclusions

large supercrystals presenting hexagonal, cubic or rhombohedral lattices made of nanocrystals assembled by the *in situ* formed benzoate moieties acting as stabilizing ligands and structure-directing agents. The supercrystals were larger than 10 μm and presented well defined 3D morphologies such as flower like, rhombic dodecahedron and bipyramids. The self-assembly of the superstructures taking place directly in the reaction medium makes this system unique.

Finally, the work carried on during the Ph.D. allowed to make some steps forward on materials engineering by soft chemistry routes. The investigation of multi-metal systems permitted to assess the effect on the reactivity of different metal ions and ligands in the same reaction pot. This is a necessary step in order to move from simple binary compounds to more complex structures and thus, it paves the way to the investigation of a variety of many other interesting materials. This work can be considered as a starting point for different research directions that can be further investigated and, of course much more can be achieved.

The optimization of the final product can pass also through post-synthesis modifications. It is well known that the organic ligand on the surface of the particles can be exchange with other organic molecules allowing specific design of the surface properties. However, it is also possible to apply other post-synthesis treatments, such as annealing. The knowledge gained in this work on the behavior of the doped particles during sintering can be exploited in order to model the desired typology of composite materials. For example, it could be possible to control the segregation of the dopant upon annealing to produce surface decorated nanoparticles.

All in all, due to their versatility, the syntheses and the assembly procedures introduced in this work can be certainly extended to a large variety of complex metal oxide nanoparticles.